# ECOLE POLYTECHNIQUE DE BRUXELLES

**ULB**

UNIVERSITÉ LIBRE DE BRUXELLES

# Study of the effect of the anti-neutrino energy resolution using the JUNO detector on the measurement of the neutrino mass hierarchy, using Monte-Carlo simulations

Mémoire présenté en vue de l'obtention du diplôme
d'Ingénieur Civil Physicien à finalité Photonique et Applications Quantiques

**Pierre-Alexandre Petitjean**

Directeur
Professeur Nicolas Pauly

Co-Promoteur
Professeur Barbara Clerbaux

Service
Métrologie Nucléaire

Année académique
2017 - 2018

# *Abstract*

**Study of the effect of the anti-neutrino energy resolution using the JUNO detector on the measurement of the neutrino mass hierarchy, using Monte-Carlo simulations**

by Pierre-Alexandre PETITJEAN

The general context of this work is the study of the elementary components of the matter and their interactions in particular in the case of the neutrino sector. The Standard Model of particle physics describes already a large part of the particles and their interactions. In 2015 the Nobel Prize in Physics was awarded jointly to Takaaki Kajita and Arthur B. McDonald for " the discovery of neutrino oscillations, which shows that neutrinos have mass". The masses of neutrinos are very small and only upper limits are obtained from direct mass measurement experiments ($m_{\nu_e} < 2$ eV). The neutrinos are the less known particles in the SM, in particular only their mass differences are measured. In addition to the unknown absolute values of the neutrino masses, the neutrino hierarchy (normal or inverted) has to be determined. The Jiangmen Underground Neutrino Observatory (JUNO) experiment is a medium baseline neutrino oscillation experiment to measure the mass hierarchy of the neutrinos and several parameters of the neutrino oscillations with a better precision than presently known. The precise measurement of the energy spectrum of the anti-neutrinos will allow distinguishing between a normal or inverted hierarchy. The object of this work is to study the effect of the anti-neutrino energy resolution on the measurement, in particular, to estimate what is the energy resolution needed to conclude on the mass hierarchy in the JUNO experiment. The first step of this work is to evaluate the anti-neutrino energy spectrum. To achieve this, a parametrization of the anti-neutrino flux using data from KamLAND and a parametrization of the inverse $\beta$-cross section were performed. To differentiate between the two hierarchies we compute Fourier transforms of the anti-neutrino energy spectra and define two parameters: RL and PV. The way chosen to simulate experiments is to use Monte Carlo simulations and to generate different pseudo-experiments. The impact of 4 key parameters is computed: 1- the distance between the nuclear plant and the reactor, 2- the oscillation parameter $sin^2(\theta_{13})$, 3- the number of events, 4- the resolution of data acquisition along the whole process. For each set of parameters, an analysis is made on the discrimination probability between the normal and inverted hierarchy. For the value of these 4 factors taken as in the JUNO facility specifications, our calculation shows that the discrimination probability with a confidence level of 3 $\sigma$, is equal to 0.991.

**Keywords**: neutrino physics - neutrino oscillations - neutrino mass hierarchy - JUNO - Fourier transforms- Monte Carlo.

# *Resumé*

**Study of the effect of the anti-neutrino energy resolution using the JUNO detector on the measurement of the neutrino mass hierarchy, using Monte-Carlo simulations**

par Pierre-Alexandre PETITJEAN

Le contexte général de ce travail est l'étude des composants élémentaires de la matière et de leurs interactions dans le cas particulier des neutrinos. Le Modèle Standard de la physique des particules décrit déjà une grande partie des particules élémentaires et leurs interactions. En 2015, le prix Nobel de physique a été décerné conjointement à Takaaki Kajita et Arthur B. McDonald pour "la découverte des oscillations des neutrinos, démontrant ainsi que les neutrinos ont une masse". Les masses des neutrinos sont très petites et seules des limites supérieures sont obtenues à partir d'expériences de mesure directe de masse ($m_{\nu_e}$ <2 eV). Les neutrinos sont les particules les moins connues du Modèle Standard, en particulier seules leurs différences de masse sont mesurées. De plus la hiérarchie des neutrinos (normale ou inversée) doit être aussi déterminée. L'observatoire souterrain de neutrinos de Jiangmen (JUNO) est une expérience d'oscillation de neutrinos de moyenne distance. Elle a pour but de mesurer la hiérarchie de masse des neutrinos et le paramètre des oscillations de neutrinos avec une meilleure précision que celle actuelle. La mesure précise du spectre d'énergie des anti-neutrinos permettra de distinguer une hiérarchie normale ou inversée. L'objet de ce travail est d'étudier la résolution en énergie des anti-neutrinos, en particulier pour estimer son effet dans la détermination de la hiérarchie de masse dans l'expérience JUNO. La première étape de ce travail consiste à évaluer le spectre en énergie des anti-neutrinos. Pour y parvenir, une paramétrisation du flux d'anti-neutrinos est faite en utilisant les données de KamLAND ainsi qu'une paramétrisation de la section efficace de désintegration $\beta$ inverse provenant de J. Engels. Pour différencier les deux hiérarchies, nous calculons les transformées de Fourier des spectres en énergie des anti-neutrinos et définissons deux paramètres: RL et PV. La manière choisie pour simuler l'expérience est d'utiliser des simulations de Monte Carlo et de génèrer des pseudo-expériences. L'impact de 4 paramètres clés est calculé: 1- la distance entre la centrale nucléaire et le détecteur, 2- le paramètre d'oscillation $sin^2(\theta_{13})$, 3- le nombre d'événements, 4- la résolution de l'acquisition des données tout au long du processus de mesure. Pour chaque ensemble de paramètres, une analyse est effectuée sur la probabilité de discrimination entre la hiérarchie normale et inversée. Pour les valeurs de ces 4 facteurs, telles que reprises des spécifications de l'installation JUNO, notre calcul montre cette probabilité de discrimination avec un intervalle de confiance de 3 $\sigma$, est égal à 0.991.

**Mots-clés**: physique des neutrinos - oscillations des neutrinos - hiérarchie des masses des neutrinos - JUNO - transformées de Fourier - Monte Carlo.

# *Acknowledgements*

I would first like to thank my thesis advisor Prof. Clerbaux of the IIHE. The door to Prof. Clerbaux office was always open whenever I ran into a trouble spot or had a question about my research or writing. She consistently allowed this paper to be my own work, but steered me in the right direction whenever she thought I needed it.

I would also like to acknowledge Prof. Pauly of the Métrologie Nucléaire department for his overall guidance on this work, and I am gratefully indebted to him for his very valuable comments on this thesis.

Finally, I must express my very profound gratitude to my parents for providing me with unfailing support and continuous encouragement throughout my years of study and through the process of researching and writing this thesis. This accomplishment would not have been possible without them.

Pierre-Alexandre Petitjean

# Contents

# Introduction

The description of Nature mechanisms has always been one of the greatest challenges for the human kind and the methods to perform it have changed with centuries. Newton has posed the main basis of the modern science in 1687 with the publication of the "*Philosophiae naturalis principia mathematica*".

Physics aims to describe quantified observation of Nature with well defined theories with a mathematical language. A theory is commonly accepted by physicists when it accurately describes the results of experiments that have already been performed. The theory must also make solid predictions that can be tested in future experiments. The start of the neutrino physics follows the same idea. In 1930, physics was facing the possibility to defeat the conservation of energy, one of the best-tested precepts of modern science, by counterexample. In the observation of the energy spectra of radioactive $\beta$-decay, the energy seems not to be conserved. To save the conservation of the energy, physicists introduced a new invisible particle, the neutrino. It is in 1956 that we have the first neutrino detection with the Reines and Cowan experience [1].

Physics has constructed in the last century one of the most successful theories: the Standard Model of particle physics (SM), which describes the elementary particles and their interactions. The SM has made extremely accurate predictions for the properties of the elementary particles and the cross sections in particle interactions. However, even though the SM has had such a great success, we know that it is not a complete description of the inner workings of Nature. In 2015 the Nobel Prize in Physics was awarded jointly to Takaaki Kajita and Arthur B. McDonald for "the discovery of neutrino oscillations, which shows that neutrinos have mass" [2]. However in the minimal version of SM the neutrinos are massless. There is a need of new physics beyond the SM to allow the possibility of massive neutrinos.

The neutrinos are the less known particles in the SM, in particular only their mass differences are measured. The masses of the neutrinos are very small and only upper limits are obtained from direct mass measurement experiments ($m_{\nu_e} < 2$ eV/c$^2$ or $m_{\nu_e} < 3.5 \ 10^{-36}$ kg) [3]. In addition to the unknown absolute values of the neutrino masses, the neutrino hierarchy (normal or inverted) has to be determined.

The Jiangmen Underground Neutrino Observatory (JUNO) experiment is a medium baseline neutrino oscillation experiment, in construction in China. The JUNO detector will measure accurately the energy spectrum of the electronic anti-neutrinos produced in nuclear plants situated at a distance of 53 km. The JUNO experiment has as main objective to measure the mass hierarchy of the neutrinos and to measure some of the neutrino oscillation parameters with a better precision than presently known.

The accurate measurement of the energy spectrum of the anti-neutrinos will allow to

distinguish between a normal or inverted hierarchy. The goal of this work is to study the effect of the anti-neutrino energy resolution on the measurement, in particular to estimate what is the energy resolution needed to conclude on the mass hierarchy in the JUNO experiment.

The way chosen to investigate this question is to use Monte Carlo simulations and generate different pseudo-experiments where the anti-neutrino energy resolution is varied. For each energy resolution hypothesis, an analysis is made on the discrimination power between the normal and inverted hierarchies.

This master thesis begins with a brief overview of the SM and of the neutrino physics. The chapter 2 presents the JUNO project. In chapter 3 the simulation of the anti-neutrino energy spectrum is constructed. The Monte Carlo simulation validation is detailed in chapter 4. The results of the analysis of the simulations are given in chapter 5.

# Chapter 1

# The Standard Model and the neutrino sector

*In this chapter the Standard Model of particle physics is briefly described. The neutrino sector is then presented. The details of the neutrino oscillation computation in the case of 2 flavor and 3 flavor schemes are given. Finally, the last section summaries the present knowledge in the neutrino sector in the Standard Model.*

## 1.1   Standard Model

The actual theoretical formulation of the Standard Model (SM) was finalized in the middle of the seventies. The basis of the model is to link elementary particles (fermions) to each other by interacting force, described by the exchange of a virtual particle (boson). All these phenomena can be developed mathematically using the quantum field theory. In this description each particle is a quantization of the field associated to the interaction. So the particles are classified according to the nature of the field of origin.

On one side there are the gauge bosons coming from interacting fields. In the SM we have 3 distinguishable forces: the electro-magnetic force, the weak interaction and the strong interaction. The gravitation is not described in the SM. For each of the interactions corresponds a force carrier particle. For the electro-magnetic force it is the photon, for the weak interaction the bosons $W^{\pm}$ and $Z$ and for the strong interaction 8 gluons.

On the other side we have the fermions. The fermions are classified in two types: the leptons and the quarks. For the leptons, due to some symmetries, the SM implies two main classes: a charged one with a certain mass (electron-type) and a neutral mass-less one (neutrino-type). Respecting the same symmetries for the quarks, the theory leads also to 2 main types of quarks: the up-type (charge 2/3) and the down-type (charge -1/3). The first flavor family corresponds to the up (u) and down (d) quarks and t be163089424o the electron (e) and the electronic neutrino ($\nu_e$); the second flavor family corresponds to the charm (c) and strange (s) quarks and to the muon and the muonic neutrino ($\nu_\mu$); the last flavor family corresponds to the top (t) and bottom (b) quarks and the tau lepton ($\tau$) and the tauic neutrino ($\nu_\tau$). Then, there is a total of 12 fermions predicted in the SM. The SM predicts also that for each of the 12 fermions it corresponds an anti-particle of the same mass but with opposite charge.

The fermions and the bosons are also differentiated by their spin. The bosons have spin 1 and the fermions have spin 1/2. The elementary particles that compose the matter are only formed with the first family: the u and d quark, and the electron. For example the protons and the neutrons, which compose the nucleus of the atoms, are composed by 3 quarks: uud and udd respectively. The elementary particles of the SM are presented in figure 1.1.

In 2012, physicists at CERN discovered a new particle, the scalar boson H (spin 0), supposed to explain the masses of all elementary particles in the Universe by spontaneous symmetry breaking through the Brout-Englert-Higgs (BEH) mechanism. The values of the masses of the elementary particles (quarks, leptons and gauge bosons) are not predicted by the SM. They are free parameters of the model and they have to be measured experimentally.

In this master thesis, we will focus more specifically on the neutrino particles. As it can be seen in figure 1.1, the masses of the 3 neutrinos are unknown. In the minimal version of the SM the $\nu$ masses are supposed to be zero. However we know now that at least two of the three neutrinos should have non-zero masses as we observe the phenomena of $\nu$-oscillations (described in section 1.3). A more complex model is thus needed to describe this phenomenon. By studying the neutrino oscillations we have a powerful tool to scrutinize the neutrino sector and to discover new physics beyond the SM. The section below gives an overview of the neutrino sector and their unanswered questions.
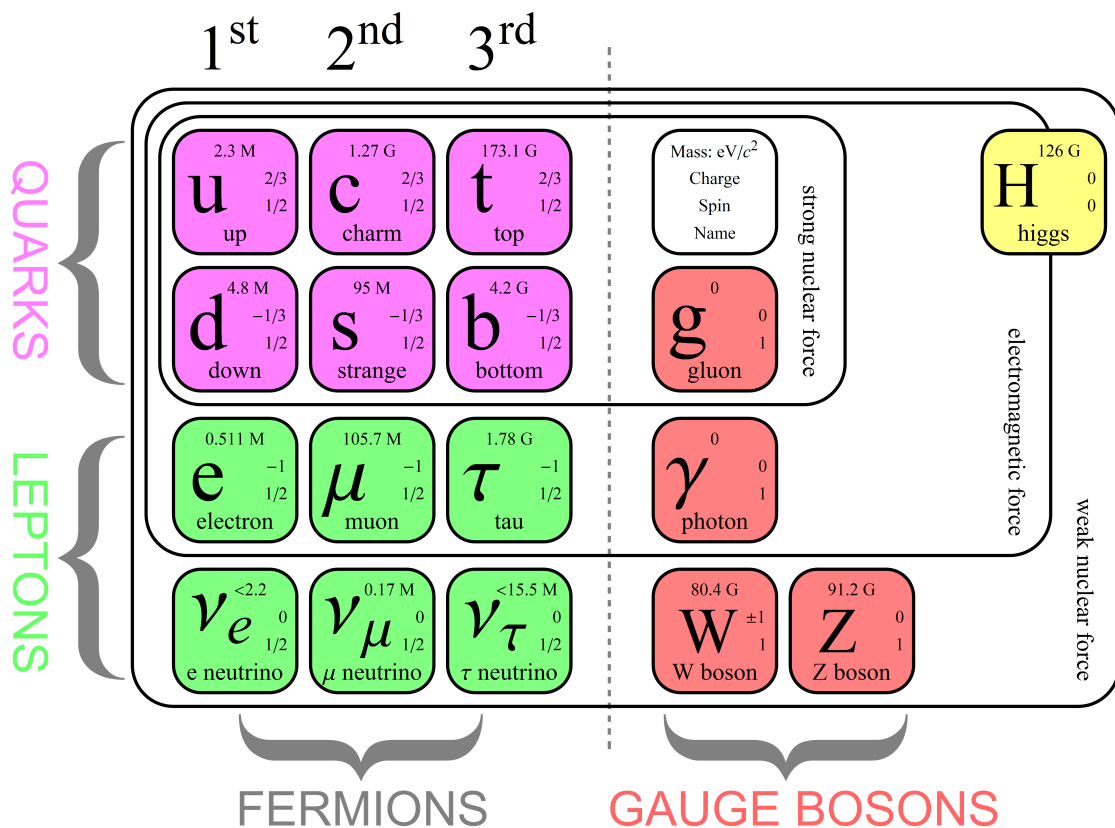


FIGURE 1.1: Actual knowledge of the SM extracted from reference [4].

## 1.2 Neutrinos physics

Neutrino physics today is one of the key challenges of our understanding of Nature. During the last decades the new phenomenon of neutrino oscillations was observed. The 2015, the Nobel Prize of physics was awarded to Takaaki Kajita and Arthur McDonald for the discovery of neutrino oscillations. In 1998 at the Super-Kamiokande detector, an experimental facility in a mine in Japan, T. Kajita and his team detected neutrinos created in reactions between cosmic rays and the earth atmosphere. Measurements show deviation compared to the SM predictions which were explained by the neutrino oscillations between the different neutrino flavors. In the SNO (Sudbury Neutrino Observatory) facility in a mine in Canada, Arthur McDonald and his team studied neutrinos created in nuclear reaction in the sun, and observed a similar phenomena. These works solved the long standing problem of solar neutrinos, which was a major discrepancy between the predicted and measured solar neutrino flux.

The neutrino oscillation phenomenon can be studied using natural sources (neutrinos from the sun or atmospheric neutrinos) and from artificial sources (neutrinos produced in accelerator facilities or in nuclear power plants).

The origin of this phenomenon can be explained by lepton mixing. The mass-state (physical state) of the neutrinos can be expressed by a combination of the flavor states (interacting states) and vice-versa. The main idea is to represent the mixing of neutrinos as a basis change. The change from the flavor basis to the mass basis can be expressed as a rotation with a certain set of angles, called the mixing angles. Neutrinos are created in their flavor eigenstates, via the weak interaction. When a neutrino propagates, the quantum mechanical phases of their mass states advance at slightly different rates due to the small difference in the neutrino masses. There is then a change of mixture in the mass states when neutrino travels, leading to an different mixture of electronic, muonic and tauic neutrinos. The probability to detect a neutrino with a certain flavor state will vary with the distance propagation.

The usual formalism uses a matrix to express the passage from the mass basis to the flavor basis. This matrix is a $3 \times 3$ unitary matrix if we consider no interaction with other neutrino generation. A $3 \times 3$ unitary matrix is characterized by 3 angles and one phase. The expression of this matrix commonly used, is:

$$U = \begin{pmatrix} c_{12}c_{13} & s_{12}c_{13} & s_{13}e^{-i\delta} \\ -s_{12}c_{23} - c_{12}s_{23}s_{13}e^{i\delta} & c_{12}c_{23} - s_{12}s_{23}s_{13}e^{i\delta} & s_{23}c_{13} \\ s_{12}s_{23} - c_{12}c_{23}s_{13}e^{i\delta} & -c_{12}s_{23} - s_{12}c_{23}s_{13}e^{i\delta} & c_{23}c_{13} \end{pmatrix} \quad (1.1)$$

This matrix is called the PMNS matrix (Pontecorvo-Maki-Nakagawa-Sakata matrix). The elements are functions of the 3 mixing angles $\theta_{12}$, $\theta_{13}$ and $\theta_{23}$, with $c_{ij} = cos(\theta_{ij})$, $s_{ij} = sin(\theta_{ij})$. We have also the Dirac phase $\delta$. This phase is related to the CP violation[1].

---

[1]CP violation is a violation of charge conjugation and parity symmetries.

## 1.3 Neutrino oscillations

The neutrinos produced by the weak interaction are of a determined flavor sate. The notations for the mass eigenstates are $\nu_1, \nu_2, \nu_3$ and for the flavor eigenstates are $\nu_e, \nu_\mu, \nu_\tau$. So a neutrino of a certain flavor can be expressed as a superposition of mass eigenstates[2]:

$$
\begin{aligned}
|\nu_e\rangle &= U_{e1}|\nu_1\rangle + U_{e2}|\nu_2\rangle + U_{e3}|\nu_3\rangle \\
|\nu_\mu\rangle &= U_{\mu1}|\nu_1\rangle + U_{\mu2}|\nu_2\rangle + U_{\mu3}|\nu_3\rangle \\
|\nu_\tau\rangle &= U_{\tau1}|\nu_1\rangle + U_{\tau2}|\nu_2\rangle + U_{\tau3}|\nu_3\rangle
\end{aligned}
\tag{1.2}
$$

Where $U_{e1}...U_{\tau3}$ are the 9 elements of the unitary PMNS matrix of equation 1.1.

### 1.3.1 Case of 2 flavor neutrino oscillation

We will first consider the case of two neutrino families. We do this simplification to illustrate easily the situation. We chose two neutrinos, for example the electronic ($\nu_e$) and the muonic ($\nu_\mu$) ones:

$$
|\nu_i\rangle = \sum_{k=1}^{2} U_{ik}|\nu_k\rangle
\tag{1.3}
$$

where $i = e, \mu$. We can understand the mixing as a rotation of the coordinate system. This matrix can be written as:

$$
U = \begin{pmatrix} cos\theta & sin\theta \\ -sin\theta & cos\theta \end{pmatrix}
\tag{1.4}
$$

where $\theta$ is the mixing angle. We can express now the two weak eigenstates as a function of the mass eigenstates:

$$
\begin{aligned}
|\nu_e\rangle &= cos\theta|\nu_1\rangle + sin\theta|\nu_2\rangle \\
|\nu_\mu\rangle &= -sin\theta|\nu_1\rangle + cos\theta|\nu_2\rangle
\end{aligned}
\tag{1.5}
$$

The mass eigenstates are solutions of the Schrödinger equation:

$$
H|\nu_k\rangle = E_k|\nu_k\rangle = i\hbar\frac{d}{dt}|\nu_k\rangle
\tag{1.6}
$$

$E_k = \sqrt{m_k^2 + p_k^2}$ corresponds to the energy of the mass state $k$ and the Hamiltonian can be expressed as:

$$
H = \begin{pmatrix} E_1 & 0 \\ 0 & E_2 \end{pmatrix}
\tag{1.7}
$$

The solutions of the equation 1.6 are plane waves and in the vacuum the propagation states are written:

$$
|\nu_k(t)\rangle = e^{-i(E_k t - p_k x)}|\nu_k(0)\rangle = e^{-i\phi_k}|\nu_k(0)\rangle
\tag{1.8}
$$

with $\phi_k = E_k t - p_k x$. Now we will consider that we have at $t = 0$ a $\nu_e$ which is created:

$$
|\nu_e(0)\rangle = |1\rangle \text{ and } |\nu_\mu(0)\rangle = |0\rangle
\tag{1.9}
$$

---

[2]This development is extracted from the reference [5].

So the mass eigenstates are expressed as follows:

$$|\nu_1(0)\rangle = cos\theta\,|1\rangle \text{ and } |\nu_2(0)\rangle = sin\theta\,|1\rangle \tag{1.10}$$

The evolution of the $|\nu_\mu\rangle$ is given by this formula:

$$
\begin{aligned}
\left|\nu_\mu(t)\right\rangle &= -sin\theta\,|\nu_1(t)\rangle + cos\theta\,|\nu_2(t)\rangle\\
&= -sin\theta e^{-i\phi_1}\,|\nu_1(0)\rangle + cos\theta e^{-i\phi_2}\,|\nu_2(0)\rangle\\
&= -sin\theta e^{-i\phi_1}cos\theta\,|1\rangle + cos\theta e^{-i\phi_2}sin\theta\,|1\rangle\\
&= \frac{1}{2}sin(2\theta)(e^{-i\phi_2} - e^{-i\phi_1})\,|1\rangle
\end{aligned} \tag{1.11}
$$

The probability of oscillation of the $\nu_e$ to $\nu_\mu$ can be computed as:

$$
\begin{aligned}
P_{\nu_e \to \nu_\mu} &= \left|\langle\nu_e(0)|\nu_\mu(t)\rangle\right|^2\\
&= \frac{1}{4}sin^2(2\theta)\left|(e^{-i\phi_2 t} - e^{-i\phi_1 t})\right|^2\\
&= sin^2(2\theta)sin^2\left(\frac{\phi_2 - \phi_1}{2}\right)\\
&= sin^2(2\theta)sin^2\left(\frac{\Delta\phi}{2}\right)
\end{aligned} \tag{1.12}
$$

In the last equality we pose $\Delta\phi = \phi_2 - \phi_1$. We will work in the ultra-relativistic limit i.e. $p \gg m_i$, and $m_1$ is the mass of the state $|\nu_1\rangle$ and $m_2$ is the mass of $|\nu_2\rangle$. We use natural units with $c = \hbar = 1$.

$$
\begin{aligned}
E^2 &= p^2 + m^2 = p^2\left(1 + \frac{m^2}{p^2}\right)\\
E &\approx p(1 + \frac{1}{2}\frac{m^2}{p^2}) = p + \frac{1}{2}\frac{m^2}{p}
\end{aligned} \tag{1.13}
$$

We have used the Taylor development of the function square root trunked at the first order. We can express the $\Delta\phi$ (using $x = c.t$):

$$\Delta\phi = (E_2 - p_2)t - (E_1 - p_1)t \approx \frac{m_2^2}{2p_2}t - \frac{m_1^2}{2p_1}t \approx \frac{m_2^2 - m_1^2}{2p}t \approx \frac{m_2^2 - m_1^2}{2E}t \tag{1.14}$$

The probability of oscillation becomes:

$$P_{\nu_e \to \nu_\mu} = sin^2(2\theta)sin^2\left(\frac{m_2^2 - m_1^2}{4E}t\right) \tag{1.15}$$

If we use now the international unit system, $h$ and $c$ will appear:

$$P_{\nu_e \to \nu_\mu} = sin^2(2\theta)sin^2\left(\frac{(m_2^2 - m_1^2)c^4}{4hE}t\right) \tag{1.16}$$

We can also replace the travel time $t$ by the travel distance $L$ by using this $L = c.t$:

$$P_{\nu_e \to \nu_\mu} = sin^2(2\theta)sin^2\left(\frac{(m_2^2 - m_1^2)c^3}{4hE}L\right) \tag{1.17}$$

In general we use specific units for this formula: $[m^2] = \text{eV}^2/c^4$, $[E] = \text{GeV}$ and $[L] = \text{km}$ and $P_{\nu_e \to \nu_\mu}$ becomes:

$$P_{\nu_e \to \nu_\mu} = sin^2(2\theta)sin^2\left(1.27\frac{\Delta m_{21}^2 L}{E}\right) \tag{1.18}$$

where $\Delta m_{21}^2 = m_2^2 - m_1^2$. In this case there is only one mixing parameter $\theta$, also labeled as $\theta_{12}$.

Figure 1.2 shows the $P_{\nu_e \to \nu_\mu}$ oscillation pattern for a 3 MeV neutrino as function of the distance. The amplitude of the oscillations is linked to the parameter $\theta$. The period is a function of the ratio between the neutrino mass difference and the energy.
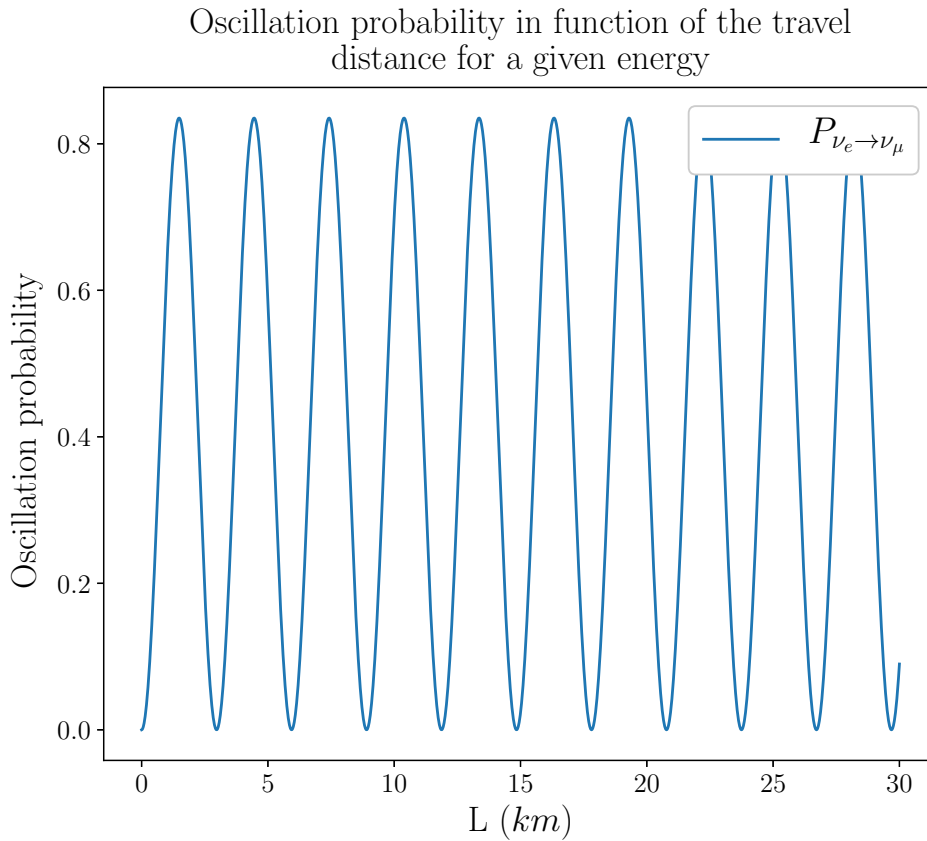


FIGURE 1.2: Graphic of the oscillation probability for $\nu_e$ to $\nu_\mu$ as function of the distance $L$ in kilometer. The parameters: $\Delta m_{21}^2$ and $sin^2(\theta_{12})$ are taken from the table 1.1 and the neutrino energy is chosen at 3 MeV.

In figure 1.3, we represent the normalized oscillation probability as a function of the variable E/L and we fix $\Delta m_{21}^2$ to 1 eV$^2$.
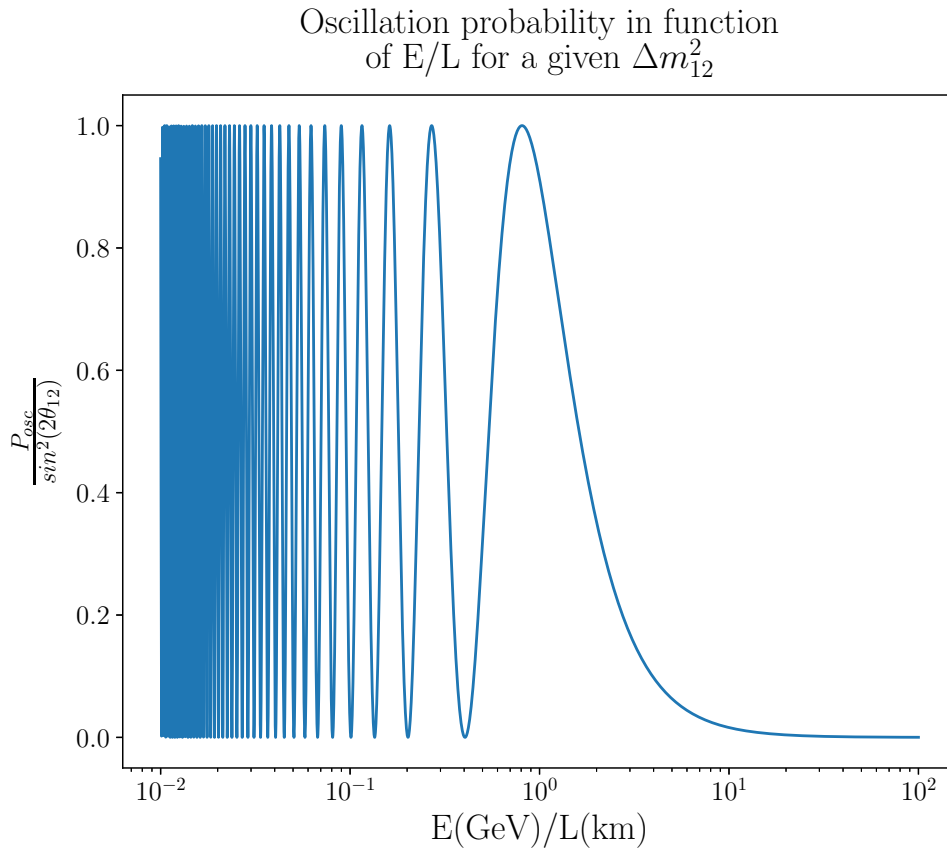
FIGURE 1.3: Graphic of the oscillation probability for $\nu_e$ to $\nu_\mu$ as a function of the distance $L$ in kilometer ($\Delta m_{21}^2 = 1\text{eV}^2$).

### 1.3.2 Case of 3 flavor neutrino oscillation

The 2 flavor neutrino oscillation mechanism described in the previous section can be generalized in the case of 3 flavors. Starting from a $\nu_\alpha$ at $t = 0$, the probability for oscillation into a $\nu_\beta$ at a time $t$ is given by:

$$P_{\nu_\alpha \to \nu_\beta} = \left| \langle \nu_\alpha(0) | \nu_\beta(t) \rangle \right|^2 = \left| \sum_k U_{\alpha k}^* U_{\beta k} e^{-im_k^2 \frac{L}{2E}} \right|^2 \tag{1.19}$$

for $k = 1, 2, 3$. We will now compute the survival probability of one electronic neutrino ($\nu_e$).

The general expression for the survival probability is:[3]

$$P_{\nu_e \to \nu_e} = \left| \sum_k U_{ek}^* U_{ek} e^{-im_k^2 \frac{L}{2E}} \right|^2 \tag{1.20}$$

$$= \sum_k^3 U_{ek}^4 + \sum_{k=1}^3 \sum_{j>k}^3 U_{ek}^2 U_{ej}^2 \left( e^{-i\frac{\Delta m_{kj}^2 L}{2E}} + e^{i\frac{\Delta m_{kj}^2 L}{2E}} \right) \tag{1.21}$$

$$= c_{12}^4 c_{13}^4 + s_{12}^4 c_{13}^4 + s_{13}^4 + 2c_{13}^4 c_{12}^2 s_{12}^2 cos \left( \frac{\Delta m_{21}^2 L}{2E} \right) \tag{1.22}$$

$$+ 2c_{13}^2 s_{13}^2 \left( c_{12}^2 cos \left( \frac{\Delta m_{31}^2 L}{2E} \right) + s_{12}^2 cos \left( \frac{\Delta m_{32}^2 L}{2E} \right) \right) \tag{1.23}$$

$$= 1 - c_{13}^4 sin^2(2\theta_{12}) sin^2 \left( \frac{\Delta m_{21}^2 L}{4E} \right) \tag{1.24}$$

$$- sin^2(2\theta_{13}) \left( c_{12}^2 sin^2 \left( \frac{\Delta m_{31}^2 L}{4E} \right) + s_{12}^2 sin^2 \left( \frac{\Delta m_{32}^2 L}{4E} \right) \right) \tag{1.25}$$

where $\Delta m_{31}^2 = m_3^2 - m_1^2$ and $\Delta m_{32}^2 = m_3^2 - m_2^2$. In the last expression we can see that the oscillation frequency is a function of the mass differences $\Delta m_{21}^2$, $\Delta m_{31}^2$ and $\Delta m_{32}^2$. On the other hand we know from neutrino oscillation measurements that $\Delta m_{21}^2 \ll \Delta m_{32}^2$, $\Delta m_{31}^2$ .

Due to the small value of $\Delta m_{21}^2$ we make the following approximation: $\Delta m_{31}^2 \approx \Delta m_{32}^2 \approx \Delta m_{fast}^2$. This leads to a two $\Delta m^2$ regimes approximation to simplify the equation 1.20. The probability of oscillation $P_{\nu_e \to \nu_e}$ can be rewritten as:

$$P_{\nu_e \to \nu_e} \approx 1 - c_{13}^4 sin^2(2\theta_{12}) sin^2 \left( \frac{\Delta m_{21}^2 L}{4E} \right) \tag{1.26}$$

$$- sin^2(2\theta_{13}) sin^2 \left( \frac{\Delta m_{fast}^2 L}{4E} \right) \tag{1.27}$$

$$= 1 - P_{slow} - P_{fast} \tag{1.28}$$

The fast oscillation regime is described by the $\Delta m_{32}^2$ and $\Delta m_{31}^2$. This part is also called the atmospheric oscillation. The slow oscillation regime is described by the $\Delta m_{21}^2$ and is called the solar oscillation. The survival probability $P_{\nu_e \to \nu_e}$ is represented in figure 1.4. The slow oscillation (red curve) corresponds to the 2 flavors case from section 1.3.1. The green curve in figure 1.4 is the oscillation due to the term in $sin^2(\frac{\Delta m_{13}^2 L}{4E})$ and $sin^2(\frac{\Delta m_{23}^2 L}{4E})$. These two sinuses have a frequency much higher than the red curve. As we can see in table 1.1, the $\Delta m_{31}^2$ and $\Delta m_{32}^2$ are in the range of $2 \times 10^{-3} \ eV^2$ and the $\Delta m_{21}^2$ is more and less equal to $7 \times 10^{-5}$ eV$^2$.

---

[3]The equation is for the normal hierarchy. A complete formula for the two hierarchies is presented in chapter 3.

| Parameter | Best fit | $3\sigma$ interval |
|---|---|---|
| $\Delta m^2_{21}$ | $7.37 \; 10^{-5} \; \text{eV}^2$ | 6.93-7.97 |
| $\Delta m^2$ | $2.5 \; 10^{-3} \; \text{eV}^2$ | 2.37-2.63 |
| $\Delta m^2_{31}$ NH | $2.536 \; 10^{-3} \; \text{eV}^2$ | 2.404-2.67 |
| $\Delta m^2_{31}$ IH | $2.423 \; 10^{-3} \; \text{eV}^2$ | 2.335-2.6 |
| $\Delta m^2_{32}$ NH | $2.463 \; 10^{-3} \; \text{eV}^2$ | 2.335-2.6 |
| $\Delta m^2_{32}$ IH | $2.496 \; 10^{-3} \; \text{eV}^2$ | 2.404-2.67 |
| $sin^2(\theta_{12})$ | 0.297 | 0.250-0.354 |
| $sin^2(\theta_{23})$ NH | 0.437 | 0.379-0.616 |
| $sin^2(\theta_{23})$ IH | 0.569 | 0.383-0.637 |
| $sin^2(\theta_{13})$ NH | 0.0214 | 0.0185-0.0246 |
| $sin^2(\theta_{13})$ IH | 0.0218 | 0.0186-0.0248 |

TABLE 1.1: Table of the parameters extracted from the particle data group's book. NH: normal hierarchy, IH: inverted hierarchy. Where $\Delta m^2 = m_3^2 - (m_1^2 + m_2^2)/2$ and thus in case of NH ($m_1 \leq m_2 \leq m_3$): $\Delta m^2 = \Delta m^2_{31} - \Delta m^2_{21}/2$ and for the IH case ($m_3 \leq m_1 \leq m_2$): $\Delta m^2 = \Delta m^2_{31} + \Delta m^2_{21}/2$ [3][6].
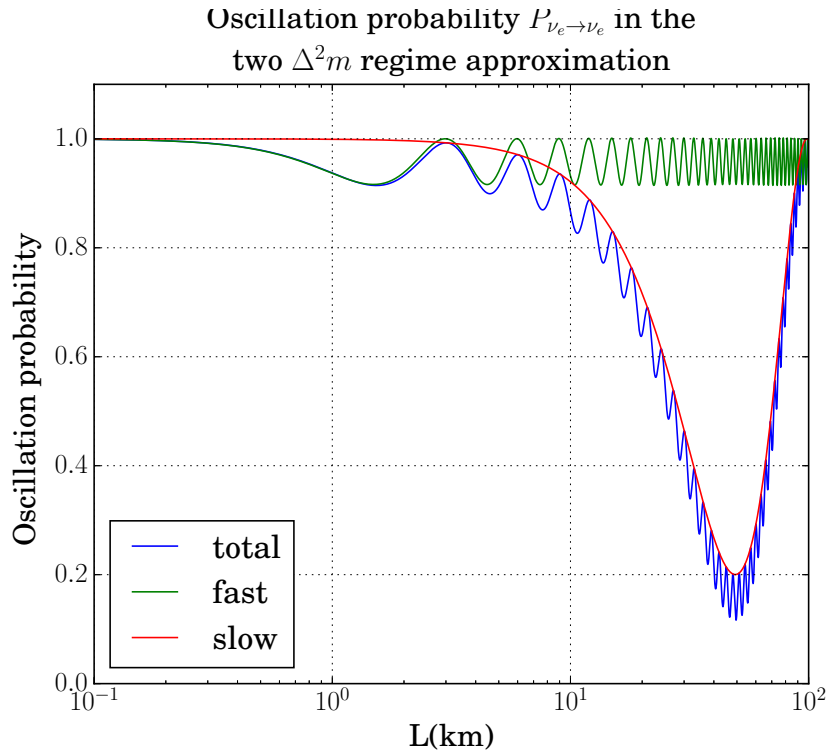


FIGURE 1.4: Graphic of the oscillation probability for $\nu_e$ to $\nu_e$ as a function of the distance $L$ in kilometer for a neutrino of 3 MeV. The parameters: $\Delta m^2_{21}$, $\Delta m^2_{fast}$ (chosen equal to $\Delta m^2$), $sin^2(\theta_{12})$, $sin^2(\theta_{23})$ and $sin^2(\theta_{13})$ are from table 1.1. The hypothesis of the normal neutrino mass hierarchy is used.

## 1.4 Actual knowledge of neutrinos in the Standard Model

Neutrino physics today is a very active research area. The parameters $\Delta m_{21}^2$ and $\theta_{12}$ are measured using solar neutrino oscillation experiment such as KamLAND [7] and Super-Kamiokande-I [8]. The parameters $\theta_{23}$ and $\Delta m_{32}^2$ are measured using different experiments as for example T2K which uses the muon neutrino disappearance to tau neutrino [9]. A recent key result is the high precision measurement of the parameter $sin^2(\theta_{13})$ by the Daya Bay experiment, and the subsequent results obtained by the RENO, Double Chooz and T2K Collaborations [10–13]. The relatively large value measured for $\theta_{13}$ opens up particular possibilities for searching for CP violation effects in neutrino oscillation experiments (see equation 1.1), and for determining the structure of the neutrino mass spectrum.

The actual knowledge of the 3 mixing angles is[4]:

- $\theta_{12} = 33.0°$

- $\theta_{23} = 41.4°$

- $\theta_{13} = 8.4°$

Then the matrix $U$ becomes (supposing $\delta = 0$):

$$U = \begin{pmatrix} 0.8294 & 0.5391 & 0.1462 \\ -0.4899 & 0.5764 & 0.6539 \\ 0.2682 & -0.614 & 0.7422 \end{pmatrix} \tag{1.29}$$

Each of the elements, when squared, corresponds to the probability of measuring one of the mass eigenstates for a given flavor. Taking for example the first line in equation 1.29, we see that $U_{e1}^2 + U_{e2}^2 + U_{e3}^2 = 1$ and $U_{e1}^2$ gives 68.8%, $U_{e2}^2$ gives 29.1% and $U_{e3}^2$ gives 2.1% represented by the red contributions ($\nu_e$ component) in $\nu_1$, $\nu_2$ and $\nu_3$ in figure 1.5.

Concerning the $\Delta m^2$ values we have 2 values determined by the same reference [14][5]:

- $\Delta m_{21}^2 = 7.37\ 10^{-5}\ eV^2$

- $|\Delta m^2| = 2.5\ 10^{-3}\ eV^2$

where $\Delta m^2 = m_3^2 - (m_1^2 + m_2^2)\frac{1}{2}$. We have still one unknown, namely the neutrino mass hierarchy: normal hierarchy (NH) or inverted hierarchy (IH).

Neutrino masses can only be generated through the Brout-Englert-Higgs (BEH) mechanism if three additional neutrino states exist. These states are avoided in the minimal version of the Standard Model (SM) of particle physics and we have no sign of their existence. Even if they exist, we need to understand why SM neutrinos are so light. The heaviest neutrino is at least 11 orders of magnitude lighter than the top quark. "Is there something in addition of the BEH mechanism that makes neutrinos so light?" is one of the open questions about the neutrinos.

---

[4]The measurements are extracted from reference [14].
[5]The error are included in table 1.1

## Neutrino mass hierarchy

For the quarks and the charged leptons, we know that the mass hierarchy is normal. It means that the top quark is heavier than the charm quark and heavier than the up quark, the observation is the same for the other down-quarks and for the charged leptons. But for the neutrino we do not know the mass ordering. To understand the situation we use the figure 1.5:
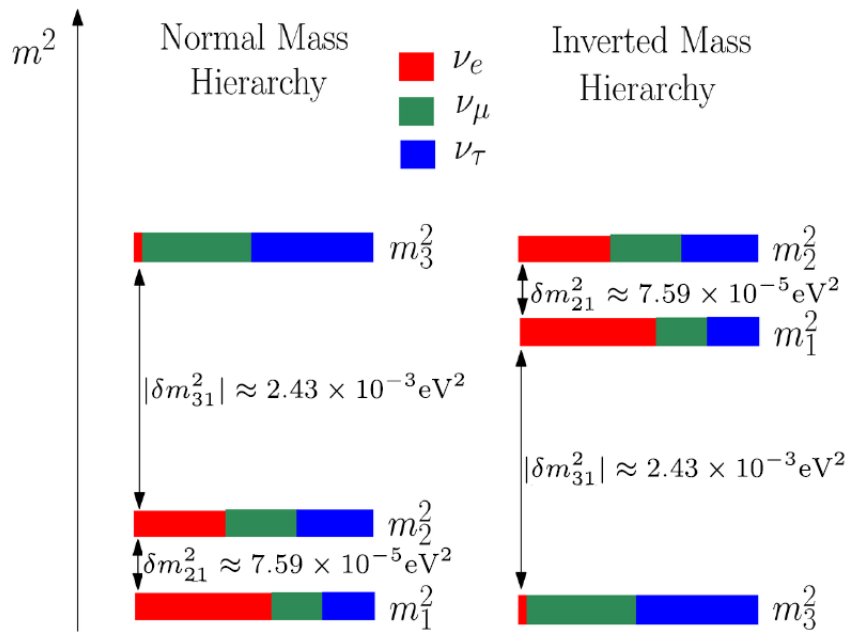


FIGURE 1.5: Figure representing the neutrino mass hierarchy in the normal case (on the left side) and in the inverted case (on the right side). The image is taken from reference [15].

In figure 1.5 we have:

- NH: $m_1 < m_2 < m_3$

- IH: $m_3 < m_1 < m_2$

We define the mass square differences:

- $\Delta m_{21}^2 = m_2^2 - m_1^2$, which is always positive.

- $\Delta m_{32}^2 = m_3^2 - m_2^2$, which is positive for the NH case and negative for IH case.

- $\Delta m_{31}^2 = m_3^2 - m_1^2$, which is positive for the NH case and negative for IH case.

The parameter $\Delta m^2$ can be either positive or negative according to the NH or IH for the neutrino mass spectrum. This parameter is determined in the reference [14] using a global fit. For the NH we can write:

- $\Delta m_{31}^2 = \Delta m^2 + \Delta m_{21}^2/2$

- $\Delta m_{32}^2 = \Delta m^2 - \Delta m_{21}^2/2$

and for the IH case:

- $\Delta m_{31}^2 = \Delta m^2 - \Delta m_{21}^2/2$

- $\Delta m_{32}^2 = \Delta m^2 + \Delta m_{21}^2/2$

The mass hierarchy will affect the oscillation probability. This impact will be used to determine the mass hierarchy by studying the neutrino oscillations as it will be explained in the chapter 3.

To study the neutrino oscillation and to resolve the neutrino mass hierarchy various projects were approved:

- India-based Neutrino Observatory (INO) is working on matter effect on atmospheric neutrino flux. Indeed there is non-standard interaction between the earth matter and the neutrinos. The detector is a magnetized iron calorimeter running in 10 years to have a $3\sigma$ confidence level on the measurement of the mass hierarchy [16].

- The NO$\nu$A is a long-baseline neutrino oscillation experiment using a beam of neutrinos coming from accelerators. To investigate the mass hierarchy of neutrinos it will focus on the $\bar{\nu}_e/\nu_e$ appearances and the $\bar{\nu}_\mu/\nu_\mu$ disappearances. The objective of this experiment is to achieve a precision of $3\sigma$ by taking data over 6 years [17].

- The JUNO experiment is a medium neutrino baseline experiment, medium referring to the distance between the source of anti-neutrino and the detector. The neutrino flux is coming from nuclear reactor. The precision achieved after the 6 years of acquiring data would be $4\sigma$ [18].

This master thesis presents a study of the neutrino mass hierarchy measurement using the future JUNO experiment. If the determination of the neutrino mass hierarchy is the prime science goal of JUNO, the experiment will also determine the solar oscillation parameters with unprecedented accuracy (< 1% level) and will test the three-flavor scenario of neutrino oscillations. Other interesting measurements at JUNO concern the proton decay physics, possible detection of neutrinos from supernovae explosion, and geo-neutrino studies. More details on the science potential of JUNO can be found in the JUNO Collaboration publication "Neutrino Physics with JUNO" [18].

# Chapter 2

# The JUNO project

*In this chapter, we will explain the various components of the JUNO detector and the measurement of the neutrino mass hierarchy by the JUNO experiment.*

## 2.1 The JUNO detector

The Jiangmen Underground Neutrino Observatory (JUNO) experiment [19] is a neutrino medium baseline experiment in China, with the objective to determine the neutrino mass hierarchy after 6 years of data taking and to perform accurate measurements of several neutrino mass and mixing parameters [18, 20–24].

The experiment uses a large liquid scintillator (LS) detector aiming at measuring electronic anti-neutrinos issued from nuclear reactors at a distance of 53 km. The detector will be located at 700 m underground and consists of 20 ktons of liquid scintillator contained in a 35 m diameter acrylic sphere, instrumented by more than 17000 20-inch photomultiplier tubes (PMT), and about 25000 3-inch small PMTs, with a cathode coverage of about 77%. Figure 2.1 presents a schematic view of the JUNO detector.

Preliminary studies in JUNO [19] have shown that the required energy resolution ($\frac{\sigma}{E}$) to discriminate between the normal and inverted neutrino hierarchies at a $3 - 4\sigma$ confidence level for about 6 years of data record is 3% at an energy of 1 MeV. This puts strong constraints on the detector component quality, in particular on the PMTs. The layout of the PMT system has been optimized with a array of small PMTs placed in between the large PMTs as shown in figure 2.2. This is called a double calorimetry system. The addition of the small PMTs is to reduce residual systematic errors that could affect JUNO. Such example is the charge extraction with the large PMTs which is non-trivial. The charge reconstruction has also non-linearity and can introduce an artificial non-uniformity. These effects are energy dependent and thus cannot be fully taken out with calibration. The idea of double calorimetry is to exploit two independent energy estimators experiencing different systematic uncertainties. One calorimetry is made with the large PMTs which perform a charge integration. The second one is made with the small PMTs operating predominantly in photon-counting mode and thus serving as a reference against which to calibrate the large ones [26].

Around the detector vetoes are added to reduce the different backgrounds. The idea of the veto is to determine if the event is coming from a cosmic muon or not. There are two

Top muon veto: plastic scintillator strips

LS: 20 kton LAB based

LS container: acrylic. The maximum stress should be <35 MPa.

Buffer: water

PMTs: 17000 20" PMTs + 34000 3" PMTS for a ~77.8% coverage

Buffer/PMT support: Stainless steel structure

Water Cherenkov veto: 20 kton water

PMTs: 2000 20" veto PMTs
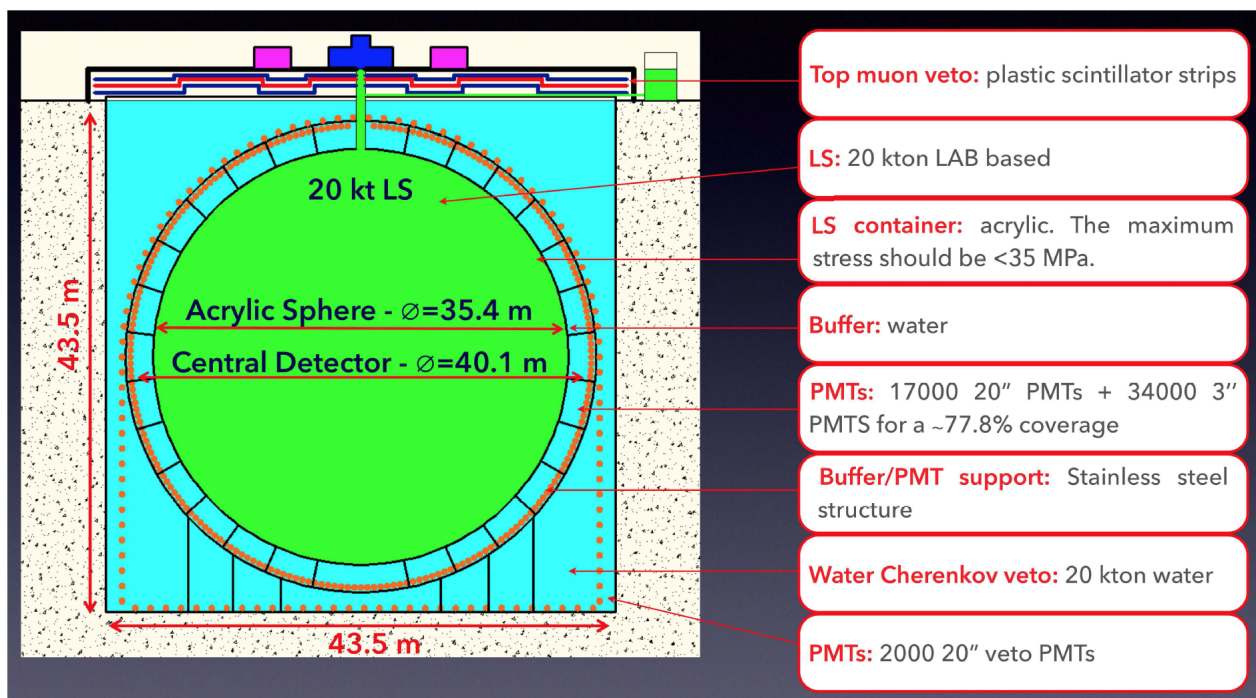
FIGURE 2.1: Schematic view of the JUNO detector. The image is extracted from reference [25].
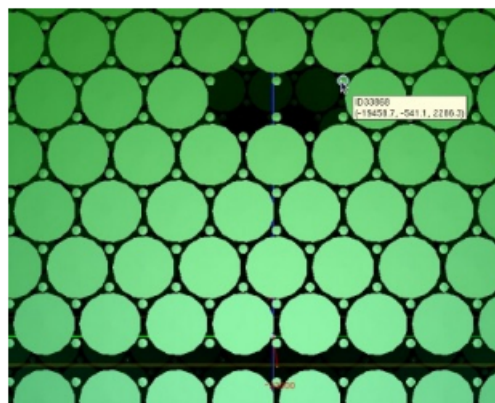


FIGURE 2.2: Schematic layout of the PMTs. Small PMTs are in the gaps between large PMTs [27].
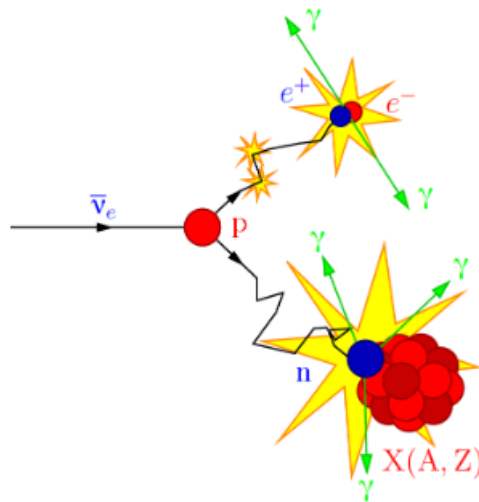
FIGURE 2.3: Schematic description of the inverse $\beta$-decay process of electronic anti-neutrino. This image is taken from reference [28].

vetos. A 20 kton ultra-pure water Cherenkov pool around the central detector instrumented by 2000 20-inch PMTs will tag events coming from outside the neutrino target. We need ultra-pure water to avoid other background noise such as the disintegration of the impurities of the water. It will also act as a passive shielding for neutrons and gammas originating from the rock around the detector.

In addition a muon tracker will be installed on top of the detector (top muon veto). It will tag cosmic muons and will be used to validate the muon track reconstruction performed by the Cherenkov pool.

Due to the large dimension of the PMTs, the measure performed by the PMTs will be affected by the earth magnetic field, and a double coil system is used as shielding.

The inverse $\beta$-decay (IBD) is the reaction used to detect the electronic anti-neutrino. The equation of the reaction is :

$$\bar{\nu_e} + p^+ \rightarrow e^+ + n \tag{2.1}$$

where $\bar{\nu_e}$ is the anti-neutrino coming from the nuclear plan, $p^+$ a proton, $e^+$ a positron and $n$ a neutron. The $e^+$ annihilates with a $e^-$ generating 2 photons of 511 keV. The neutron slows down and is then captured by an atom in the liquid and generates photons. These photons are generated with a certain delay in comparison with the photons from the disintegration of the $e^+$. This is represented in figure 2.3. This process leads to two signals in the detector. The first signal is the detection by the PMTs of the photons coming from the positron annihilation. The second one is coming from the delayed absorption of the neutron.

The international JUNO collaboration was established in 2014, the civil construction started in 2015, the *R&D* for the detector is on its final phase, and the production and test have started for the main components (the large PMTs and the central detector structure). The start of the data taking is expected at the end of 2021.

## 2.2 The measurement of the mass hierarchy

There are two possible methods to determine the mass hierarchy. The first one uses matter effects introduced by collective interactions of neutrinos with electrons in matter (experiments NOνA and INO, see section 1.4). JUNO pursues a second method. It exploits an interference effect between the 3-flavor oscillations in the disappearance of electronic anti-neutrinos emitted from nuclear power reactors [18, 20–24]. The interference manifests itself in a rapid oscillation pattern superimposed over the solar oscillation. The frequency of the pattern depends on the mass hierarchy, as shown in figure 2.4. The various steps in order to obtain this energy spectra are explained in details in chapter 3. The energy spectra is given here only to illustrate the general method. This method provides a clean determination of the mass hierarchy. It does not suffer from correlations with the leptonic CP-violation, which are intrinsic to the first method.
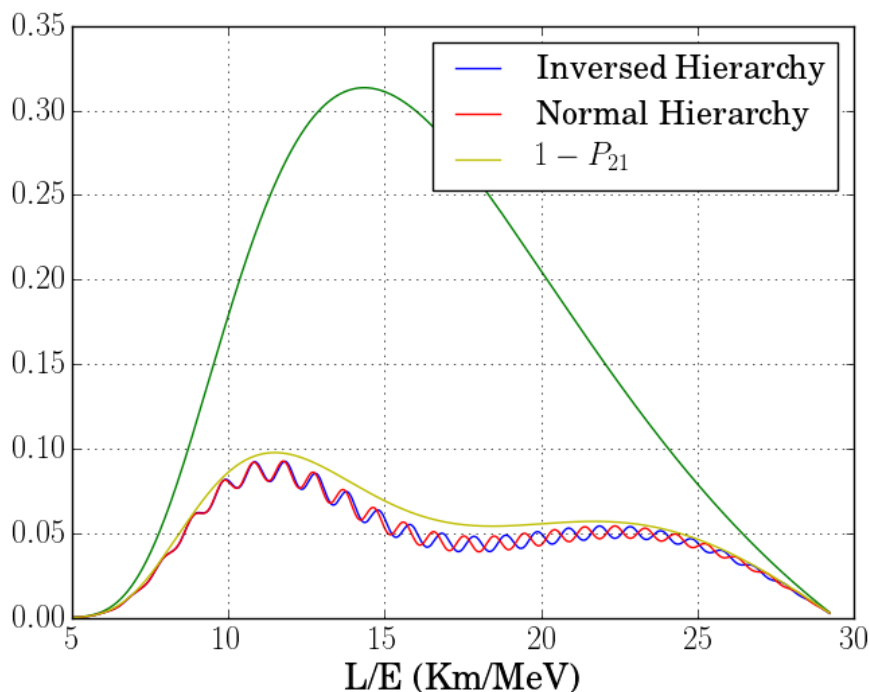


FIGURE 2.4: The (L/E) energy spectrum and the frequency pattern for normal and inverted neutrino mass hierarchy. The parameters for the energy spectrum are taken from table 1.1.

On figure 2.5 we have represented the oscillation probability for $\nu_e \to \nu_e$ as function of the travel distance $L$ (as in figure 1.4) for the two hierarchy cases. The normal hierarchy is the blue curve and the inverted hierarchy is the green curve. The other experiments using electronic anti-neutrinos are also represented. In figure 2.5a we observe that JUNO works in a distance between the other experiments. At this distance (53 km), there is a minimum in the solar oscillation (see section 1.3.2). Working with this distance will allow high precision on the measurement of the solar parameters.

Figure 2.5b is a zoom of figure 2.5a. The distance of 53 km is the optimal distance to place a detector in order to measure the neutrino mass hierarchy. One notices from figure 2.5 that

the main challenge to distinguish the NH and the IH is to have an excellent neutrino energy resolution.
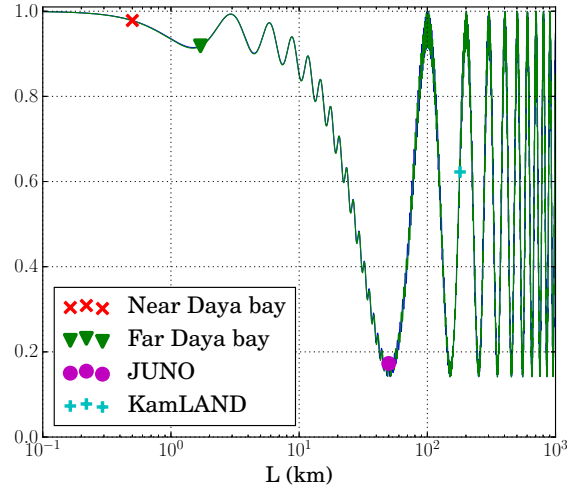


(A)
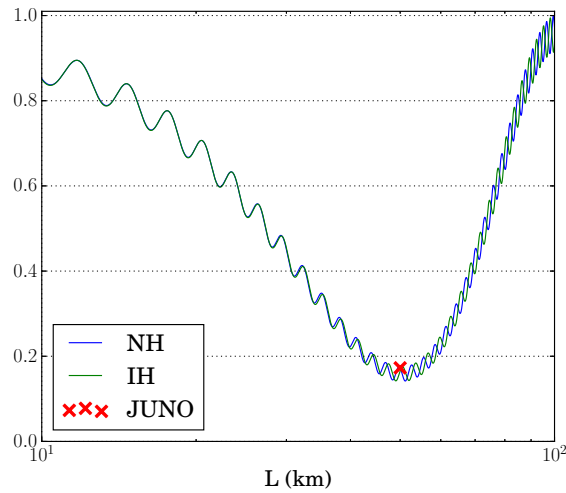


(B)

FIGURE 2.5: Graphic of the oscillation probability for $\nu_e$ to $\nu_e$ as a function of the distance $L$ in kilometer for a neutrino of 3 MeV. The parameters: $\Delta m_{21}^2$, $\Delta m_{31}^2$, $\Delta m_{32}^2$, $sin^2(\theta_{12})$, $sin^2(\theta_{23})$ and $sin^2(\theta_{13})$ are from table 1.1. The distances chosen by Daya bay, KamLAND and JUNO experiments are represented in figure 2.5a. On the lower panel we restrain the figure from 10 km to 100 km.

The neutrino interaction is identified observing the IBD signal in the liquid scintillator, relying on the twofold coincidence between the prompt signal given by the positron ionization and annihilation (1-10 MeV) and the delayed signal of 2.2 MeV given by the neutron capture on hydrogen. The background is divided into an accidental and a correlated contribution. The accidental background is given by radioactivity gammas (from PMTs or surrounding rock), which fake a prompt or a delayed signal, and it can be reduced by passive shielding. The

correlated background is mostly given by cosmogenic isotopes such as $^9$Li produced by muon interactions in the detector or in the rock around it.

With the knowledge of the different origins of the backgrounds, a set of preliminary anti-neutrino selection criteria can be listed below [18]:

- Fiducial volume: the interaction should be located inside the LS at a radius r < 17 m, where the radius of the acrylic curve is 17.5 m. This cut allows to reduce most of the accidental background noise coming from the PMTs surrounding the cuve.

- The prompt energy cut 0.7 MeV < $E_p$ < 12 MeV, $E_p$ is the energy of the positron.

- The delayed energy cut 1.9 MeV < $E_d$ < 2.5 MeV, $E_d$ is the delayed energy.

- The time interval between the prompt and delayed signal $\Delta$T <1.0 ms. We cut the event if the delay between the detection of the energy due to the positron and the detection of the energy due to the neutron is too high.

- The prompt-delayed distance cut $R_{p-d}$ < 1.5 m. $R_{pd}$ is the distance between the point of detection of the energy due the positron and the detection point of the energy due to the neutron.

- Muon veto criteria:

  - for muons tagged by the Water Pool, veto over the whole LS volume for 1.5 ms.
  - for good muon tracks in central detector and water Cerenkov detector, veto over the detector volume within $R_{d2\mu}$ < 3 m and $T_{d2\mu}$ < 1.2 s. $R_{d2\mu}$ and $T_{d2\mu}$ are respectively the radius around the muon trajectory and the time of travel of the muon in the detector.
  - for the tagged, non-trackable muons in central detector, veto over the whole LS volume for 1.2 s.

The anti-neutrino selection efficiency due to the fiducial volume cut is 91.8 %. The energy cut, time cut, and vertex cut have efficiencies of 97.8%, 99.1%, and 98.7%, respectively. Assuming 99% muons have good reconstructed track, the efficiency of the muon veto cut is estimated to be 83%. After the background rejection cuts, a signal of about 60 events per day is expected, with a remaining background of about 3.8 events per day, as shown in table 2.1 [18].

| Selection | IBD efficiency | IBD | Geo-$\nu$s | Accidental | $^9$Li/$^8$He |
|---|---|---|---|---|---|
| - | - | 83 | 1.5 | $\sim 5.7 \times 10^4$ | 84 |
| Fiducial volume | 91.8% | 76 | 1.4 | | 77 |
| Energy cut | 97.8% | | | 410 | 71 |
| Time cut | 99.1 % | 73 | 1.3 | | |
| Vertex cut | 98.7% | | | 1.1 | 1.6 |
| Muon veto | 83 % | 60 | 1.1 | 0.9 | 1.6 |
| Combined | 73% | 60 | | 3.8 | |

TABLE 2.1: The efficiencies of anti-neutrino selection cuts, signal and background rates per day (with reactors of 36 GW thermal power, located at 53 km and for a 20-kton LS detector) [18].

# Chapter 3

# The parameterization of the anti-neutrino energy spectra

*In this chapter, we present the parameterization of the anti-neutrino energy spectra. We study the impact of the neutrino mass hierarchy (NH and IH) on the anti-neutrino energy spectrum measured in JUNO. A Fourier transform method is described to differentiate the energy spectra in the 2 neutrino mass hierarchy cases. Finally the impact of the distance between the reactor plants and the detector on the neutrino mass hierarchy measurement is presented, as well as the effect of varying the neutrino mixing angles and the $\Delta m^2$ parameters.*

## 3.1 The energy spectrum

In this section, we construct the anti-neutrino energy-spectrum that will be measured in JUNO. This energy spectrum is the product of three terms:

- $\phi(E)$: the flux of electronic anti-neutrinos coming from the reactor plants

- $\sigma(E)$: the cross section for a anti-neutrino to interact in the detector

- $P_{\bar{\nu}_e \to \bar{\nu}_e}(E/L)$: the probability that a anti-neutrino produced at the reactor plants stays as a electronic anti-neutrino when arriving in the detector. By CPT symmetry in the SM $P_{\bar{\nu}_e \to \bar{\nu}_e}(E/L) = P_{\nu_e \to \nu_e}(E/L)$ and the equations used in the previous chapter can be used here for $P_{\bar{\nu}_e \to \bar{\nu}_e}(E/L)$.

The energy spectrum $F(E/L)$ is then:

$$F(E/L) = \phi(E)\sigma(E)P_{\nu_e \to \nu_e}(E/L) \tag{3.1}$$

### 3.1.1 Determination of the neutrinos flux

For the flux, we have taken the measurements from the KamLAND experiments [29]. We suppose here that the composition of the reactor fuel is similar between KamLAND and JUNO. The data point from KamLAND are represented in figure 3.1.
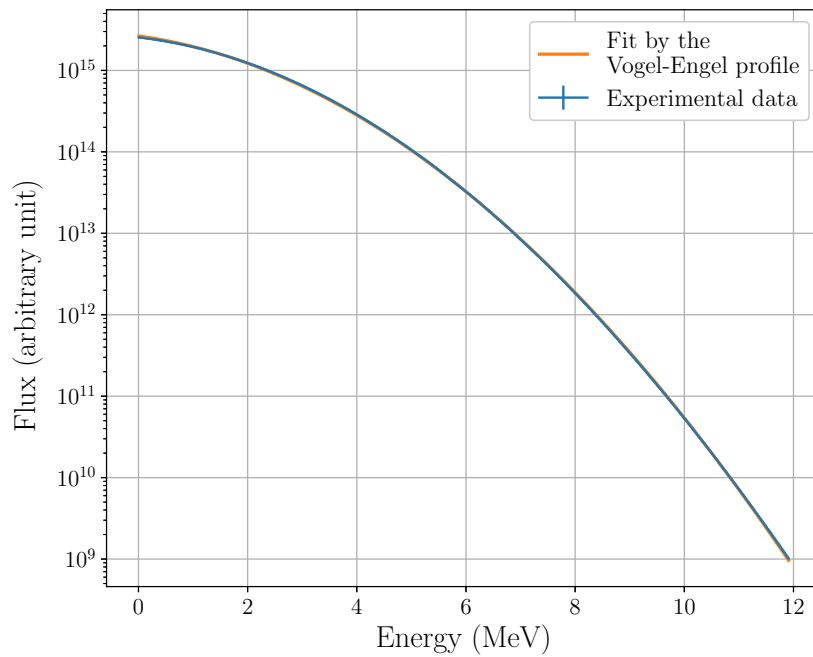
FIGURE 3.1: Flux of electronic anti-neutrinos: data points extracted from reference [29] (in blue) and fitted function (in green).

In order to construct our simulations, we will need a parameterization of the flux $\phi(E)$ as function of the anti-neutrino energy. For this a commonly used parameterization from J. Engel is considered and is explained in the reference [30]. In this publication the following formula is taken to describe the anti-neutrino flux coming from a single production in a nuclear reactor:

$$\frac{dN_\nu}{dE_\nu} = e^{a_0 + a_1 \times E_\nu + a_2 \times E_\nu^2} \tag{3.2}$$

If we have more than one-isotope producing anti-neutrinos, we can simply sum on the different isotopes with a coefficient proportional to the fraction of this isotope in the composition of the nuclear fuel. In this work we used the one-isotope formula.

The data from KamLAND and the result of the fit using equation 3.2 are presented in figure 3.1. We found for the variable $a_0 = 35.51, a_1 = -0.214\,\text{MeV}^{-1}, a_2 = -0.0865\,\text{MeV}^{-2}$. We see that the fit is well contained in a band made of the error of 6% on the flux.

To verify the fit of the experimental data, we represent the relative error in figure 3.2. The relative error is defined as:

$$\delta\phi = \frac{\Delta\phi}{\phi} = \frac{\phi' - \phi_{exp}}{\phi_{exp}} \tag{3.3}$$

where $\phi'$ is the fitted value and $\phi_{exp}$ is the experimental value. The experimental error is 3%. Figure 3.2 shows that on the useful interval (see latter) the relative difference is contained in the experimental error range.

In table 3.1, we have the $a_i$ parameters in the case of a nuclear fuel composed with $^{235}$U , $^{239}$Pu, $^{238}$U and $^{241}$Pu with a specific concentration as presented in reference [29]. We observe
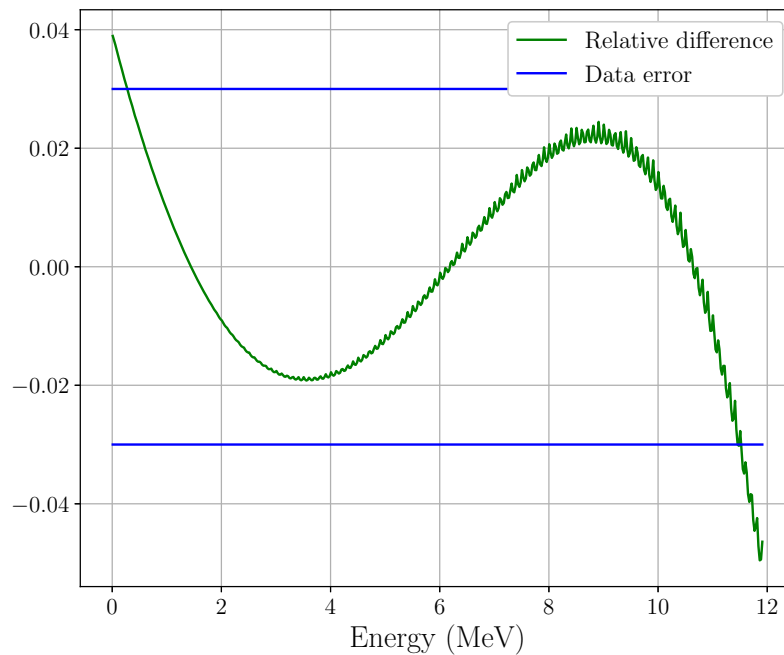
FIGURE 3.2: Relative difference between data and the fit in green. The blue lines represent the error on the data points.

TABLE 3.1: Comparison between the fitted parameter values obtained in this master thesis (last column) with the values obtained by KamLAND extracted from [29].

| Isotope | $^{235}$U | $^{239}$Pu | $^{238}$U | $^{241}$Pu | | Fitted value |
|---|---|---|---|---|---|---|
| $a_0$ | 0.870 | 0.896 | 0.976 | 0.793 | | 35.51 |
| $a_1$ (MeV$^{-1}$) | -0.160 | -0.239 | -0.162 | -0.080 | | - 0.2144 |
| $a_2$ (MeV$^{-2}$) | -0.0910 | -0.0981 | -0.0790 | -0.1085 | | -0.08654 |

that our fitted values for $a_1$ and $a_2$ are in the same range than the ones of KamLAND. For $a_0$ the values are different due to a normalization factor. To validate the one-isotope approximation we compare the shape of the flux in the case of a fitting with a single isotopes emitting electronic anti-neutrinos with the case presented in the reference [29] where we have 4-isotope mixing. The blue curve in figure 3.3b is the case of only one-isotope emitting neutrinos and the green curve is the 4-isotope case.

To only compare the shape and not the absolute value we have normalized the 4-isotope case to the single isotope case. We observe that the shape is similar in the two cases. In figure 3.3b we observe that the relative difference between the one- isotope parameterization and the 4-isotope parameterization is very small. We can conclude that the one-isotope case is a good enough approximation for the rest of the work.
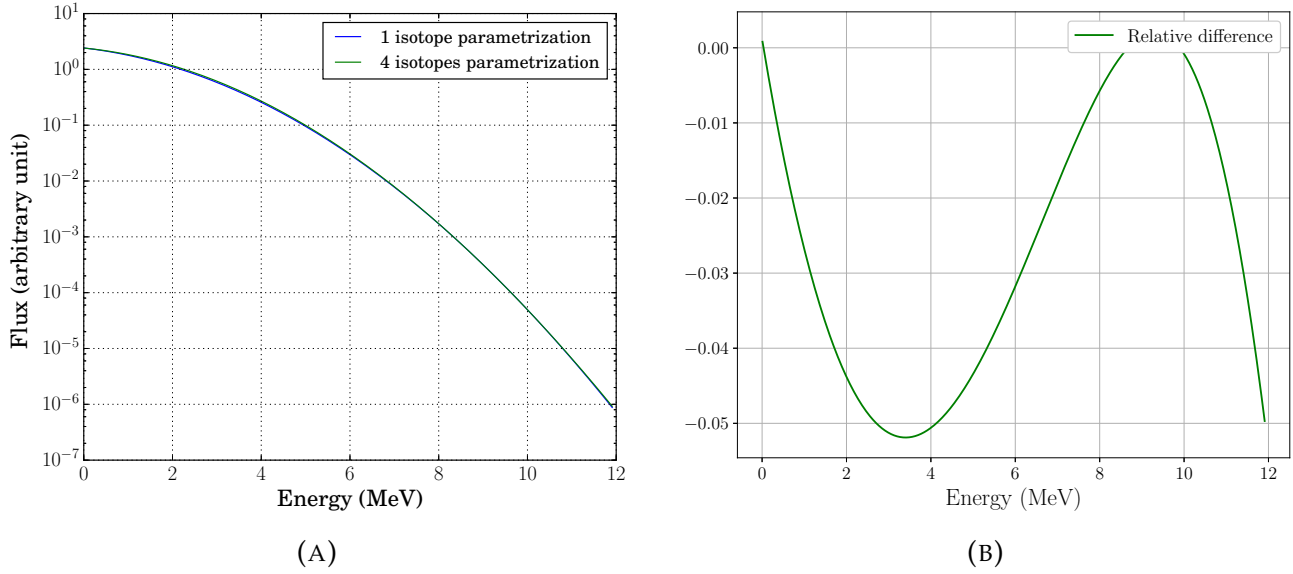
FIGURE 3.3: The figure 3.3a is the fitted fluxes of the electronic anti-neutrinos for the different parameterizations: fit for one-isotope (blue) and fit for four isotopes ( green) using the parameters from table 3.1. The figure 3.3b represents the relative difference between the one-isotope parameterization and the 4-isotope parameterization.

### 3.1.2 Determination of the inverse $\beta$-decay cross section $\sigma(E)$

As explained in section 2.2, the anti-neutrino is detected when it interacts with a proton. We have to parameterize the cross section of this interaction as function of the energy of the incident anti-neutrino. We received as input of this work numerical result from the paper [31]. In this paper, the positron angular distribution is calculated, which at low energies is slightly backward. It is also shown that weak magnetism and recoil corrections have a large effect on the angular distribution, making it isotropic at about 15 MeV and slightly forward at higher energies. The paper explains also that the behavior of the cross section and the angular distribution can be well understood analytically for $E_{\overline{\nu}_e} < \sim 60$ MeV by calculating to $\mathcal{O}(1/M)$, where M is the nucleon mass. Indeed we work with anti-neutrinos in the [0-10 MeV] energy range. The following equation gives the cross section input (the green curve in figure 3.4) :

$$\sigma_{tot}^{(0)} = \frac{2\pi^2}{m_e^5 \cdot f_{p.s.}^R \cdot \tau_n} E_e^{(0)} \cdot p_e^{(0)} \tag{3.4}$$

where $\tau_n$ is the measured neutron lifetime, and $f_{p.s.}^R = 1.7152$ is the phase space factor, including the Coulomb, weak magnetism, recoil, and outer radiative corrections, but not the inner radiative corrections [31]. $E_e^{(0)} = E_\nu - \Delta$ is the positron energy and the positron impulsion $p_e^{(0)} = \sqrt{E_0^2 - m_0^2}$ , $E_\nu$ is the energy of incident anti-neutrino and $\Delta$ the mass difference between the proton and neutron.

To continue the work we need a parametrization of the theoretical value (given in the green curve in figure 3.4) as function of the energy of the incident anti-neutrino. We have fitted
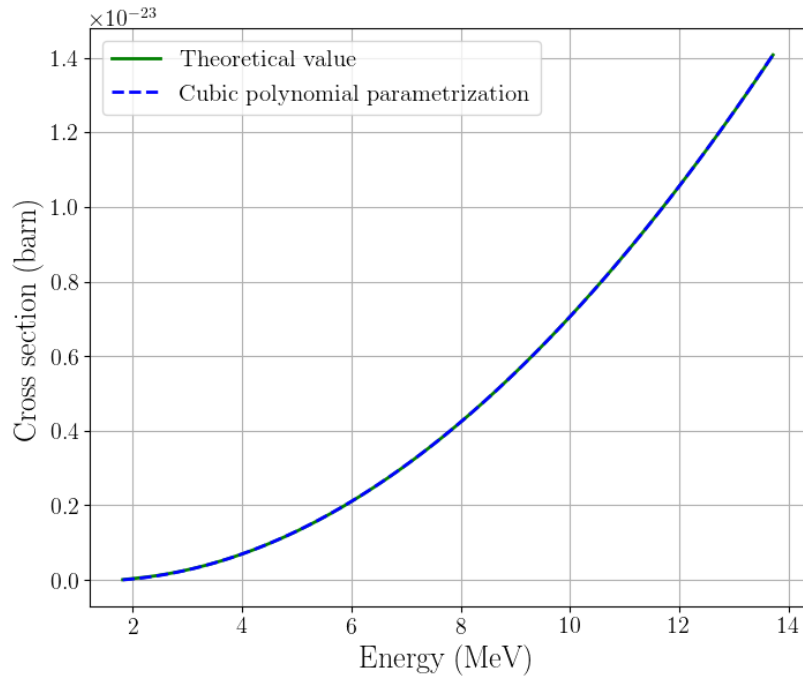
FIGURE 3.4: Graphic of cross section in function of the energy of the neutrinos for the inverse $\beta$ decay.

the theoretical values with a cubic polynomial function of the energy of the anti-neutrino:

$$\sigma'(E_v) = a + b \cdot E_v + c \cdot E_v^2 + d \cdot E_v^3 \tag{3.5}$$

The result of this parameterization is the blue stripped line in figure 3.4. As for the flux, we compute the relative difference between the theoretical value $\sigma_{tot}^{(0)}$ and the parameterization $\sigma'$:

$$\delta\sigma = \frac{\Delta\sigma}{\sigma} = \frac{\sigma' - \sigma_{tot}^{(0)}}{\sigma_{tot}^{(0)}} \tag{3.6}$$

We represent this in figure 3.5. We observe that the relative error is small excepted a the threshold (1.8 MeV). Indeed we lose the threshold comportment by using the cubic polynomial parametrization.

### 3.1.3 Determination of the product $\phi(E).\sigma(E)$

We compute the energy distribution by multiplying the anti-neutrino flux and the inverse $\beta$-decay cross section taken from sections 3.1.1 and 3.1.2, respectively. In figure 3.6, the flux is given as a function of the energy in red, the cross section for the invert $\beta$ decay is given in blue, and the product of the two is shown in green. We observe that the energy range goes from 1.8 MeV to about 10 MeV. Below 1.8 MeV, we are below the inverted $\beta$ decay threshold ($\sigma = 0$) and above 10 MeV the anti-neutrino flux is extremely small. The energy spectrum presented as the green curve in the figure would be the result of the experiment if they are no oscillation
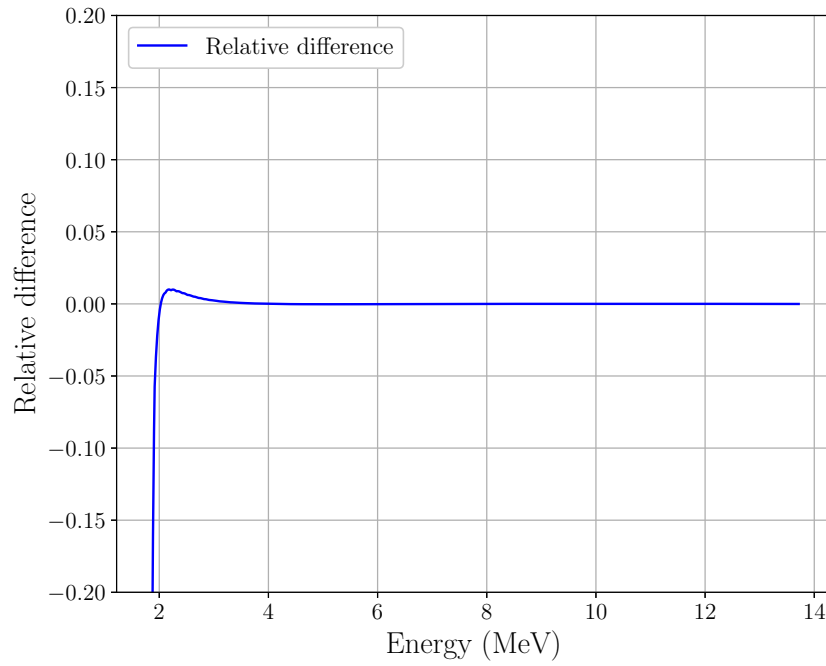
FIGURE 3.5: Relative difference between the parameterization $\sigma'$ and the theoretical values $\sigma_{tot}^{(0)}$ [31].
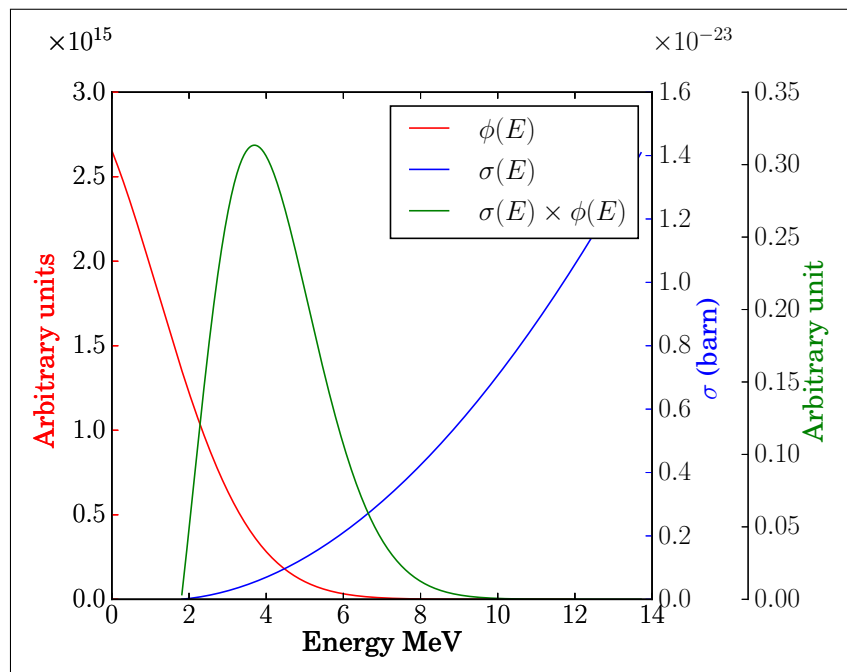


FIGURE 3.6: Graphic of convolution between the flux (in red) and the cross section (in blue). The parameters used for the flux description are taken from the equation 3.2 and table 3.1 (last column). The parameters used for the inverse $\beta$-decay cross section are from figure 3.4

phenomena. The following section highlights the effect of neutrino oscillation on the energy spectra.

## 3.2 Impact of the different mass hierarchies

### 3.2.1 Expression of the oscillation probability with the mass hierarchy terms

From equations 1.24 and 1.25 to make the difference between the two mass hierarchies visible we follow the procedure of the paper [32]. To begin this development we write the probability as:

$$P_{\nu_e \to \nu_e}(L/E) = 1 - P_{21} - P_{31} - P_{32} \tag{3.7}$$

where

$$P_{21} = cos^4(\theta_{13})sin^2(2\theta_{12})sin^2\left(\frac{\Delta m_{21}^2 L}{4E}\right) \tag{3.8}$$

$$P_{31} = sin^2(2\theta_{13})cos^2(\theta_{12})sin^2\left(\frac{\Delta m_{31}^2 L}{4E}\right) \tag{3.9}$$

$$P_{32} = sin^2(2\theta_{13})sin^2(\theta_{12})sin^2\left(\frac{\Delta m_{32}^2 L}{4E}\right) \tag{3.10}$$

$$\tag{3.11}$$

First, we introduce the parameter $\Delta_{ij}$:

$$\Delta_{ij} = \frac{(m_i^2 - m_j^2)L}{4E} \tag{3.12}$$

Then we consider the fast part of the probability : $P_{31}$ and $P_{32}$.

$$P_{Fast} = P_{31} + P_{32} \tag{3.13}$$
$$= sin^2(2\theta_{13})(cos^2(\theta_{12})sin^2(\Delta_{31}) + sin^2(\theta_{12})sin^2(\Delta_{32})) \tag{3.14}$$

In the second term, we express $\Delta_{32}$ as function of the 2 other squared mass differences. Then $\Delta_{32} = |\Delta_{31} \mp \Delta_{21}|$ (the $-$ sign is for the normal mass hierarchy and the $+$ is for the inverted mass hierarchy) and thus we will express the factor $sin^2(\Delta_{32}) = sin^2(|\Delta_{31} \mp \Delta_{21}|)$. By using trigonometry formula and by doing some algebra, the expression of the sinus becomes:

$$sin^2(|\Delta_{31} \mp \Delta_{21}|) = sin^2\Delta_{21}cos(2\Delta_{31}) \mp \frac{1}{2}sin^2(2\Delta_{21})sin(2|\Delta_{31}|) \tag{3.15}$$

By introducing this result in equation 3.7 we obtain the following equation for the survival probability of a electronic anti-neutrino:

$$
\begin{aligned}
P_{\nu_e \to \nu_e} = \ & 1 - cos^4(\theta_{13})sin^2(2\theta_{12})sin^2(\Delta_{21}) & (3.16) \\
& - sin^2(2\theta_{13})(cos^2(\theta_{12})sin^2(\Delta_{31}) + sin^2(\theta_{12})sin^2\Delta_{21}cos(2\Delta_{31})) & (3.17) \\
& \pm \frac{1}{2}sin^2(2\theta_{13})sin^2(\theta_{12})sin^2(2\Delta_{21})sin(2|\Delta_{31}|) & (3.18)
\end{aligned}
$$

We see that only the last term of the equation is affected by the choice of the mass hierarchy; the plus sign is for the NH and the minus sign for the IH.

### 3.2.2   Impact on the product of the cross section and flux

As reminder the energy spectra is given as follows:

$$
F(E/L) = \phi(E)\sigma(E)P_{\nu_e \to \nu_e}(E/L) \tag{3.19}
$$

where the anti-neutrino flux ($\phi(E)$), the cross section ($\sigma(E)$) and the oscillation probability are given respectively in section 3.1.1, 3.1.2 and 3.2.1. Figure 3.7 [1] shows the results of this equation. The green curve is the product $\phi(E)\sigma(E)$ (as in figure 3.6) normalized such as the area below the curve is equal to 1. The yellow curve is when we use instead of the total oscillation probability, the solar oscillation ($1 - P_{21}$) in equation 3.19. The red (blue) curve is the energy spectrum for NH (IH). We have also represented in figure 3.7b, the $L/E$ spectrum to better differentiate two hierarchy cases which are difficult to see in the energy spectrum in figure 3.7a.

## 3.3   Highlighting the different mass hierarchies using Fourier transform

### 3.3.1   Mathematical background

The mathematical aspect was developed in [33]. We will resume it rapidly here. We will use a Fourier cosine transform (FCT) and a Fourier sine transform (FST) defined as :

$$
FCT(\omega) = \int_{t_{min}}^{t_{max}} F(t)cos(\omega t)dt \tag{3.20}
$$

$$
FST(\omega) = \int_{t_{min}}^{t_{max}} F(t)sin(\omega t)dt \tag{3.21}
$$

---

[1]The figure 3.7b is the same as figure 2.4.

(A) dependence in the energy     (B) dependence in L/E
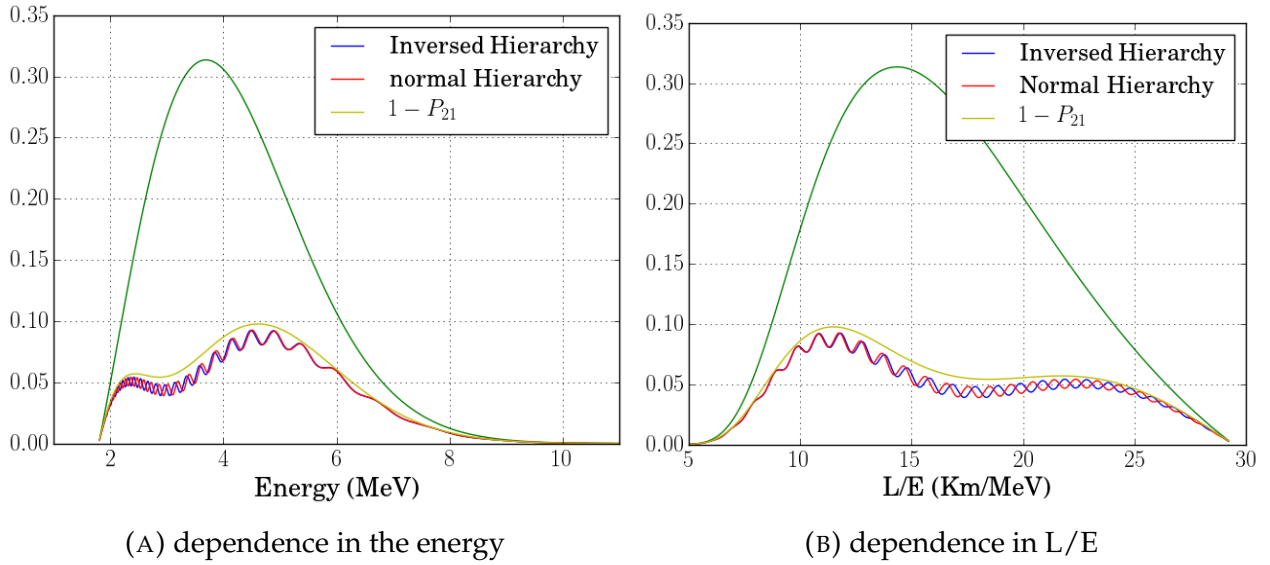
FIGURE 3.7: Energy spectrum (left) and $L/E$ spectrum (right) for the anti-neutrino, both for NH and IH. The normal hierarchy is given by the red spectra and the inverted hierarchy by the blue ones. The yellow line is the $1 - P_{21}$ probability corresponding to the solar oscillation. The green line is the product $\phi(E) \cdot \sigma(E)$ obtained at the figure 3.6. The distance parameter L is fixed at 53 km as in the JUNO experiment.

where $t = L/E$ and, for the bounds of the integral $t_{min} = \frac{L}{E_{max}}$ and $t_{max} = \frac{L}{E_{min}}$. The function F(t) is the anti-neutrino energy spectrum from equation 3.1. The parameter $\omega$ is defined as $\omega = 2 \cdot 1.27 \cdot \delta m^2$ in the reference [33].

### 3.3.2 Application of Fourier transform in case of neutrinos oscillations

We will now use this formalism on the neutrino oscillation both for the NH and for the IH. By applying the formulas 3.20 and 3.21 to the energy spectra on the figures 3.7b we obtain the FCT($\omega$) and FST($\omega$) distributions in figures 3.8a and 3.8b, respectively.

(A) FCT

(B) FST
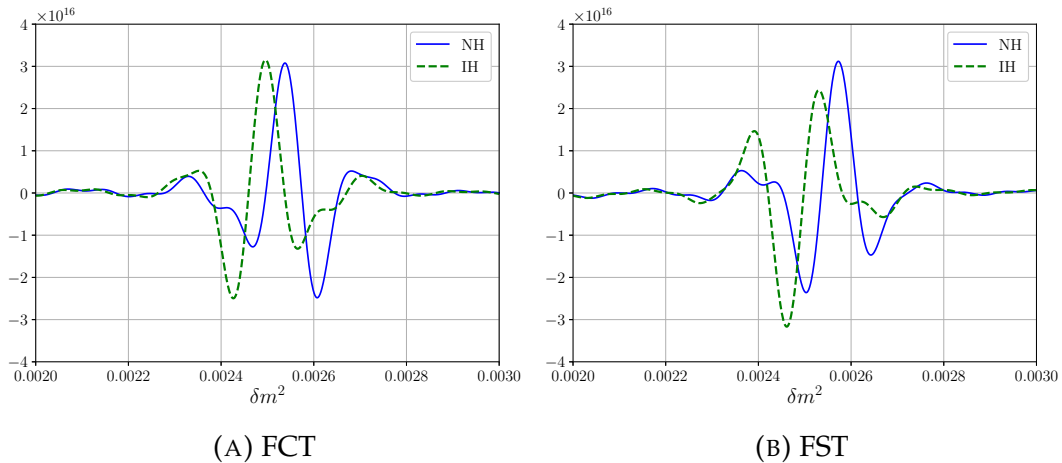
FIGURE 3.8: Fourier cosine transform and Fourier sine transform for the curves in the graphic 3.7b, as function of the parameter $\delta m^2$. The blue curves are for the normal hierarchy and the green are for the inverted hierarchy. The chosen parameters for the integral are $t_{min} = 6625$ and $t_{max} = 29444$ to obtain the agreement with previously published results [18, 33].

To understand the influence of the different components of the oscillation probability on the Fourier transforms we rewrite the oscillation probability as:

$$P_{\nu_e \to \nu_e} = P_{sol} + P_{atm_1} + P_{atm_2} \tag{3.22}$$

where,

$$P_{sol} = 1 - cos^4(\theta_{13})sin^2(2\theta_{12})sin^2(\Delta_{21}) \tag{3.23}$$

$$P_{atm_1} = -sin^2(2\theta_{13})(cos^2(\theta_{12})sin^2(\Delta_{31}) + sin^2(\theta_{12})sin^2\Delta_{21}cos(2\Delta_{31})) \tag{3.24}$$

$$P_{atm_2} = \pm\frac{1}{2}sin^2(2\theta_{13})sin^2(\theta_{12})sin^2(2\Delta_{21})sin(2|\Delta_{31}|) \tag{3.25}$$

Figure 3.9 shows the different Fourier transforms for the different components in the two cases of neutrino mass hierarchy. The results of the Fourier transform are the black curves for the total oscillation probability ($P_{\nu_e \to \nu_e}$), the blue curves are for the solar oscillation ($P_{sol}$), the green curves for the first part of the atmospheric oscillation ($P_{atm_1}$) and the red curves for the second part of the atmospheric oscillation ($P_{atm_2}$). We can first observe that the components of the atmospheric oscillation dominate the FCT and FST spectra in the interested frequency range of $2 \times 10^{-3}$ eV$^2 < \delta m^2 < 3 \times 10^{-3}$ eV$^2$ if the mass square $\Delta m_{31}^2$ and $\Delta m_{32}^2$ are in this range. The contribution of the solar oscillation is very small because $\Delta m_{21}^2$ is infinitesimal compared to $\Delta m_{31}^2$ and $\Delta m_{32}^2$ (see table 1.1). We see also that only $P_{atm_2}$ is affected by the neutrino mass hierarchy. This is important because it gives to the global oscillation probability the following properties:

- For the NH case, the shape of the FCT spectrum has the deepest valley on the right while in the IH case the deepest valley is on the left.

- For the FST spectrum, the peak has a bigger amplitude than the deepest valley for the NH case and the deepest valley has bigger amplitude than the highest peak for the IH case.

These features can be used to distinguish NH and IH.



(A) FCT for NH

(B) FST for NH

(C) FCT for IH

(D) FST for IH
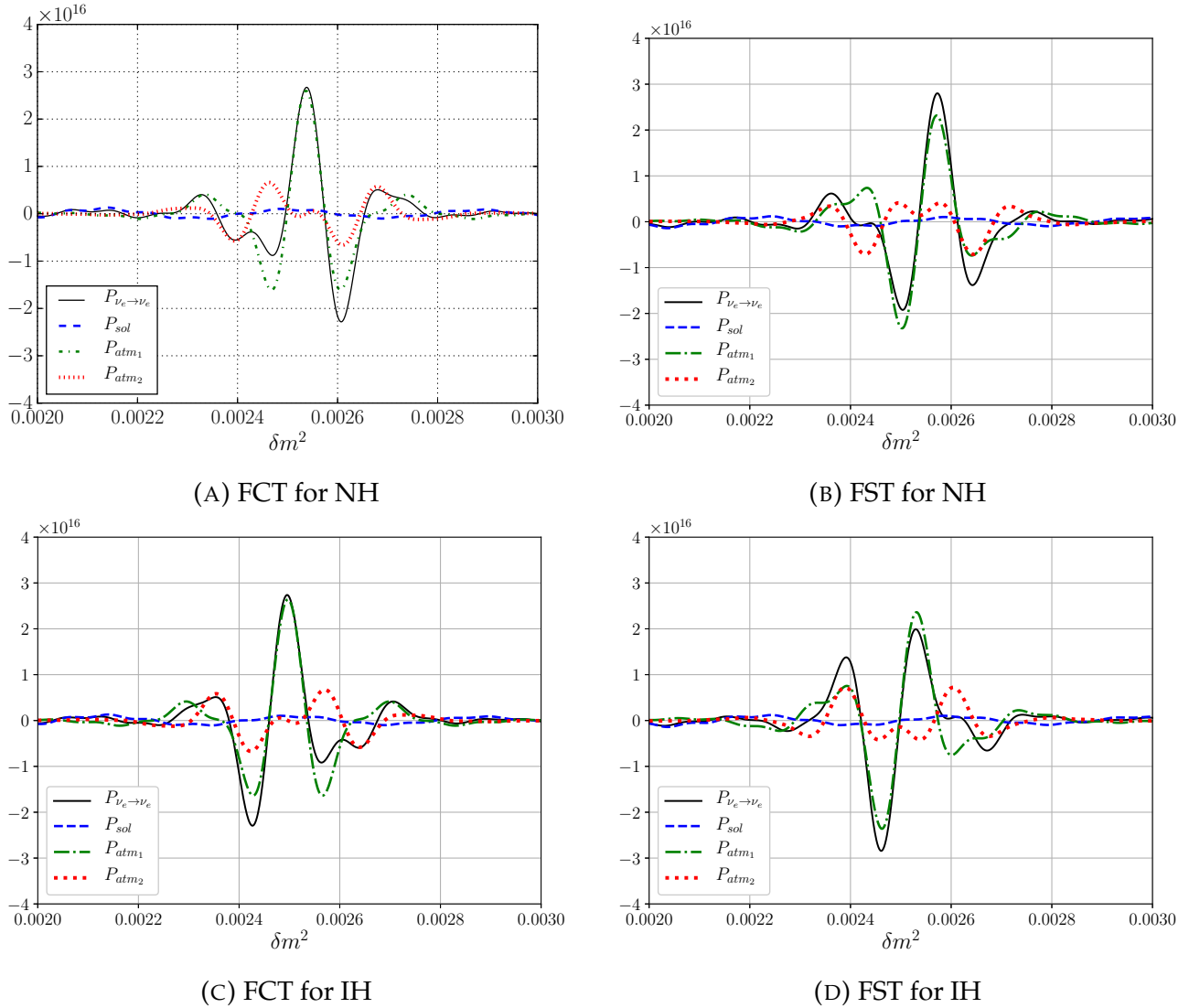
FIGURE 3.9: Fourier cosine and Fourier sine transform spectra for $P_{sol}$ component (blue line), $P_{atm_1}$ component (green line), $P_{atm_2}$ component (red line) and all the components of $P_{\nu_e \to \nu_e}$ (black line) in the cases of NH and IH.

### 3.3.3 Definition of RL and PV

To differentiate between the NH and the IH, two quantities are defined, called RL and PV [33]. The sign of these parameters will characterize the type of mass hierarchy. For the FCT, we take the value of the amplitude of the right valley denoted by R and the amplitude of the left valley denoted by L. This is represented in figure 3.10a. In figure 3.10a, we see the two different sets

(A) FCT



(B) FST
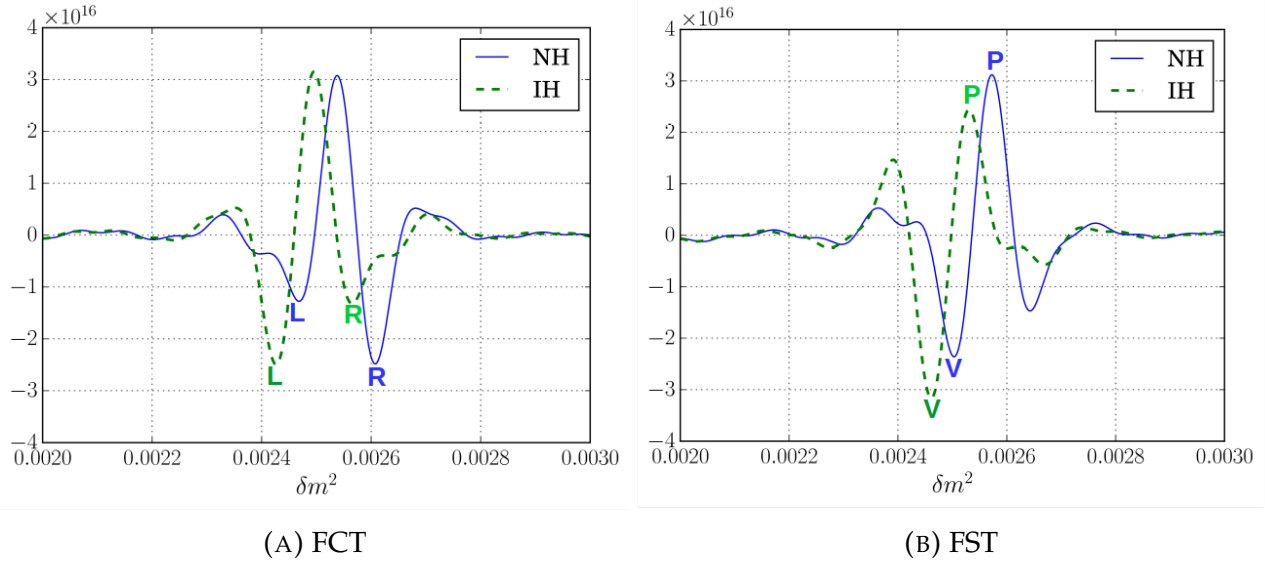
FIGURE 3.10: Theoretical Fourier cosine transform and Fourier sine transform. On the left we have the FCT and the parameters R (amplitude of the right valley) and L(amplitude of the left valley) in the case of NH and IH. The FST is presented on the right with P (amplitude of the peak)and V (amplitude of the valley) parameters in the case of NH and IH.

of value for the normal (in blue) and inverted (in green) hierarchy. The RL parameter is defined as:

$$RL = \frac{R - L}{R + L} \tag{3.26}$$

The sign of this parameter gives the type of hierarchy. Indeed we see in figure 3.10a that the parameter is positive for normal hierarchy and negative for inverted hierarchy .

For the FST, we take the value of the amplitude of the highest peak denoted by P and the amplitude of the deepest valley denoted by V (as it is shown in figure 3.10b). We define the parameter PV as :

$$PV = \frac{P - V}{P + V} \tag{3.27}$$

As for the Fourier cosine transform, the sign of the PV parameter gives the type of mass hierarchy. The plus sign is for normal hierarchy and the minus sign is for inverted hierarchy.

Each point in figure 3.11 corresponds to a pseudo-experiment of 100 000 events simulated using Monte Carlo simulations. The x-value corresponds to the parameter RL computed for the pseudo-experiment and the y-value to parameter PV. We have done 5000 pseudo-experiments for each mass hierarchy. The detailed explanation is provided in chapter 4. The figure illustrates the data clouds corresponding to a given mass hierarchy. Indeed the cloud for the normal hierarchy corresponds to the zone where RL and PV are positive (in blue). And for the inverted hierarchy, all the values are contained in a cloud in the green part of the figure where RL and PV are negative.
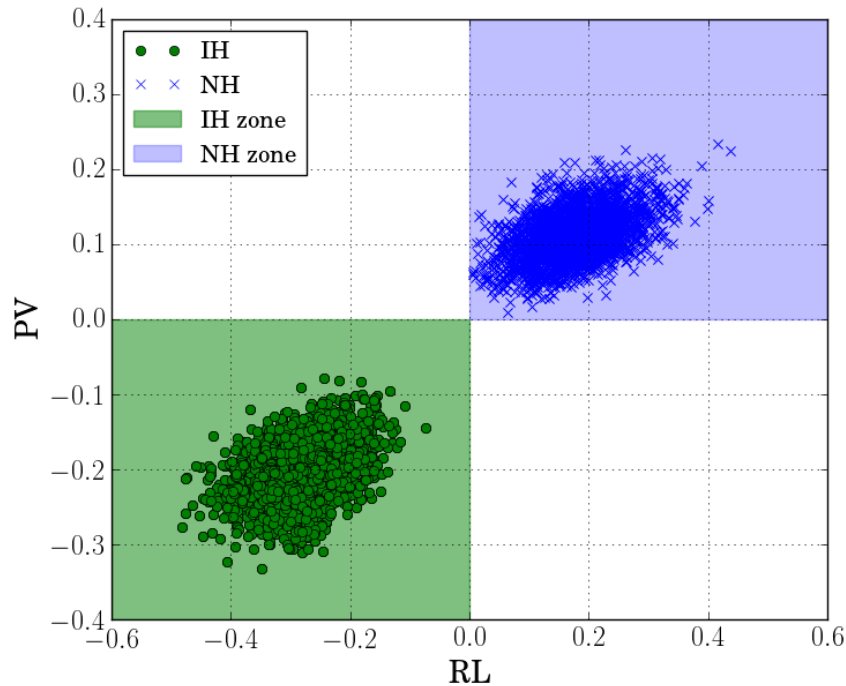
FIGURE 3.11: Example set of 5000 pseudo-experiments simulated by Monte Carlo method using a distance L of 53 km, a statistic of 100 000 events and a perfect energy resolution.

### 3.3.4   Impact of the distance

In this section, we study how the Fourier transforms are affected by changing the distance between the anti-neutrino source and the detector. We already know that the distance is a key parameter in the neutrino oscillations and affects the anti-neutrino energy spectrum. Consequently the distance also affects the RL and PV parameters. Figure 3.12 shows the evolution of the Fourier transforms FCT (left plots) and FST (right plots) when the distance is changed. The reference distance for JUNO is 53 km. The graphics show indeed that the Fourier transforms are changing with the distance. We see that for a distance of 35 km the two hierarchies are less separated that for a distance of 53 km. The general shape of the Fourier transforms is the same for the two cases but the amplitude of variation is smaller in the case of a distance of 35 km. This is explained by considering the equations 3.20 and 3.21. When the distance is decreasing, the upper and lower limits in the integral are also decreasing and the value of the integral also decreases. For the distance of 75 km the value of RL and PV are the same for the two hierarchies.
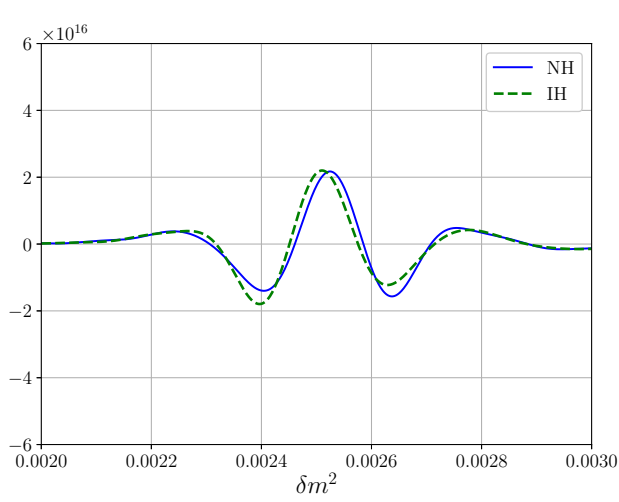
(A) FCT for a distance of 35 km
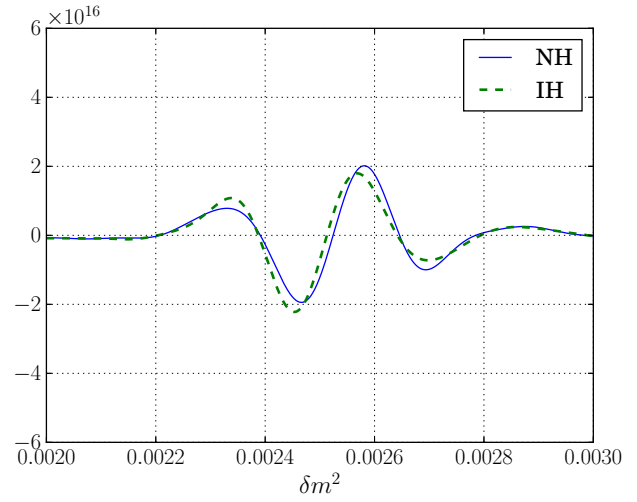
(B) FST for a distance of 35 km
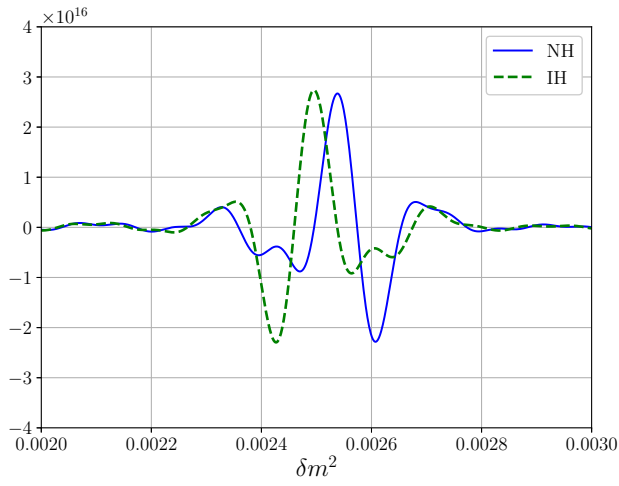
(C) FCT for a distance of 53 km
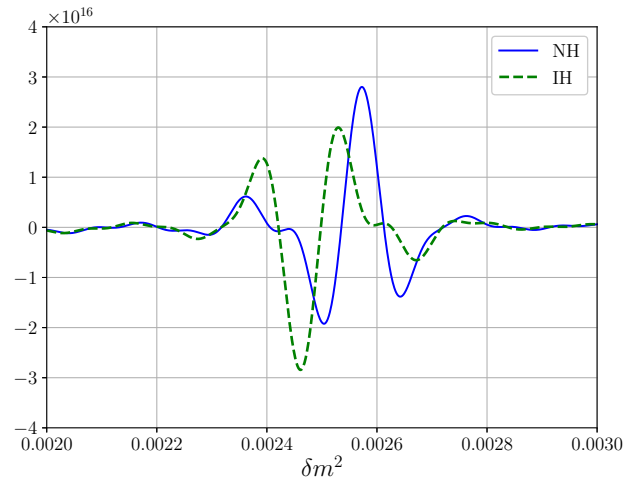
(D) FST for a distance of 53 km
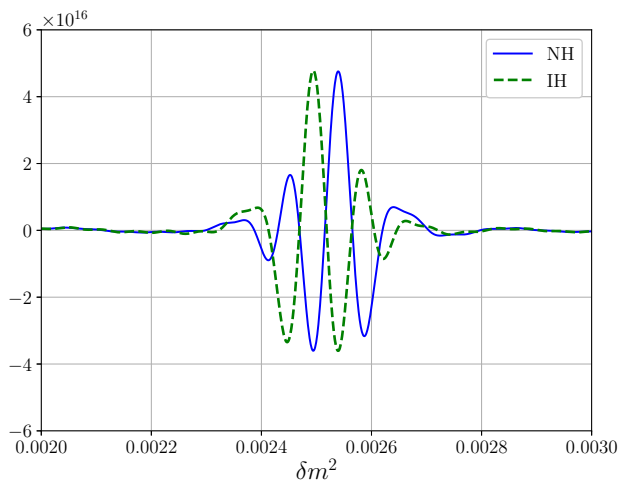
(E) FCT for a distance of 75 km
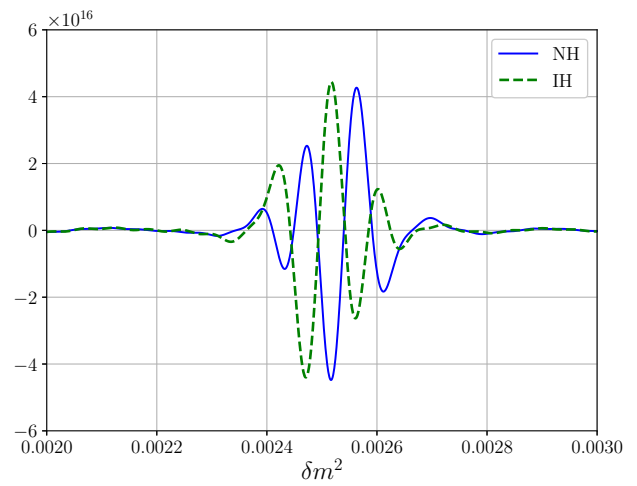
(F) FST for a distance of 75 km

FIGURE 3.12: Shape of the Fourier transform of the spectrum for different distances: 35, 53 and 75 km.

### 3.3.5   Impact of the parameters on the shapes of the Fourier transforms

We have 4 parameters ($sin^2(\theta_{13})$, $sin^2(\theta_{12})$, $\Delta m^2_{21}$ and $\Delta m^2$) playing a role in the anti-electronic neutrino oscillation. These parameters are measured by various experiments with a certain precision. In the following we will study how the experimental errors on these measurements impact the shape of the Fourier sine and cosine transforms. The method used is to take 3 values (the measured value $-3\sigma$, the measured value, and the measured value $+3\sigma$) for each parameter independently and to observe how the FCT and FST are affected. The $3\sigma$ error range is taken from table 1.1.

- $sin^2(\theta_{13})$: Figures 3.13 show the Fourier transforms when varying $sin^2(\theta_{13})$. When $sin^2(\theta_{13})$ is increasing the amplitudes of the Fourier transforms increase also. This is explained by looking at the survival probability:

$$
\begin{aligned}
P_{\nu_e \to \nu_e} = {}& 1 - cos^4(\theta_{13})sin^2(2\theta_{12})sin^2(\Delta_{21}) && (3.28) \\
& - sin^2(2\theta_{13})(cos^2(\theta_{12})sin^2(\Delta_{31}) + sin^2(\theta_{12})sin^2\Delta_{21}cos(2\Delta_{31})) && (3.29) \\
& \pm \frac{1}{2}sin^2(2\theta_{13})sin^2(\theta_{12})sin^2(2\Delta_{21})sin(2|\Delta_{31}|) && (3.30)
\end{aligned}
$$

The blue part of the equation corresponds to the solar oscillation. The green and the red terms are the atmospheric oscillation terms. In the green and red term we have the same factor $sin^2(2\theta_{13})$ as explained in section 3.3.2. Consequently we expect when the value of $\theta_{13}$ increases, the amplitudes of the Fourier transforms increase also. This is indeed observed in figure 3.13. The variation of the amplitude affects the value of RL and PV and then, the discrimination of the mass hierarchy. A study of this is performed in chapter 5

- $sin^2(\theta_{12})$: We have computed the Fourier transforms for the three values of $sin^2(\theta_{12})$. We present this computation in figure 3.14 . We observe that the Fourier transforms change with this parameter. The amplitude of the Fourier transforms decreases when the value of $sin^2(\theta_{12})$ decreases.

- $\Delta m^2$: The value $\Delta m^2$ plays a role inside the equations 3.29 and 3.30 through the parameters $\Delta_{31}$ and $\Delta_{32}$. As presented in figure 3.15 it does not affect the amplitude of the Fourier transforms, but the curves are shifted along the x-axis. As the shape of the Fourier transforms do not vary the power of discrimination is not affected.

- $\Delta^2 m_{21}$: Figure 3.16 shows the shape of the Fourier transforms for the different values of $\Delta m^2_{21}$. As for $sin^2(\theta_{12})$ we do not see differences between the 3 cases. The explanation is also the same. $\Delta m^2_{21}$ is a parameter that matters for the solar term but it doesn't appear in the atmospheric oscillation while the methods study only this oscillation.

  As conclusion, we have shown that only the factor $sin^2(2\theta_{13})$ affects significantly the shapes of the Fourier transforms of the oscillation spectra, and then affect also the parameters PV and RL.

(A) FCT for $-3\sigma$

(B) FST for $-3\sigma$

(C) FCT for the measured value

(D) FST for the measured value

(E) FCT for $3\sigma$

(F) FST for $3\sigma$
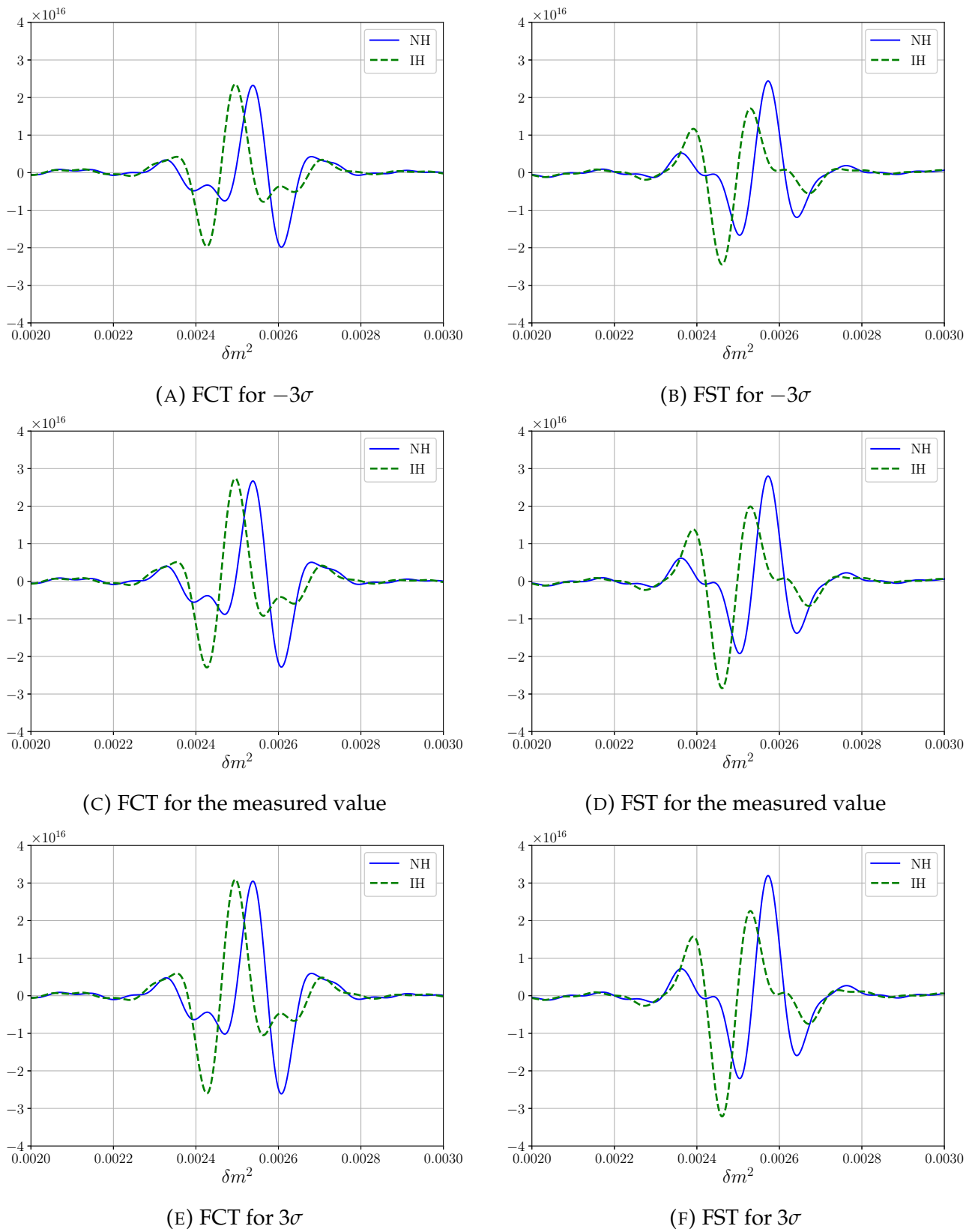
FIGURE 3.13: The Fourier transforms FCT (left plots) and FST (right plots) for various values of the $sin^2(\theta_{13})$ parameter : the measured value $-3\sigma$ (top), the measured value (middle) and the measured value $+3\sigma$ (bottom).

(A) FCT for $-3\sigma$

(B) FST for $-3\sigma$

(C) FCT for for the measured value

(D) FST for the measured value

(E) FCT for $3\sigma$

(F) FST for $3\sigma$
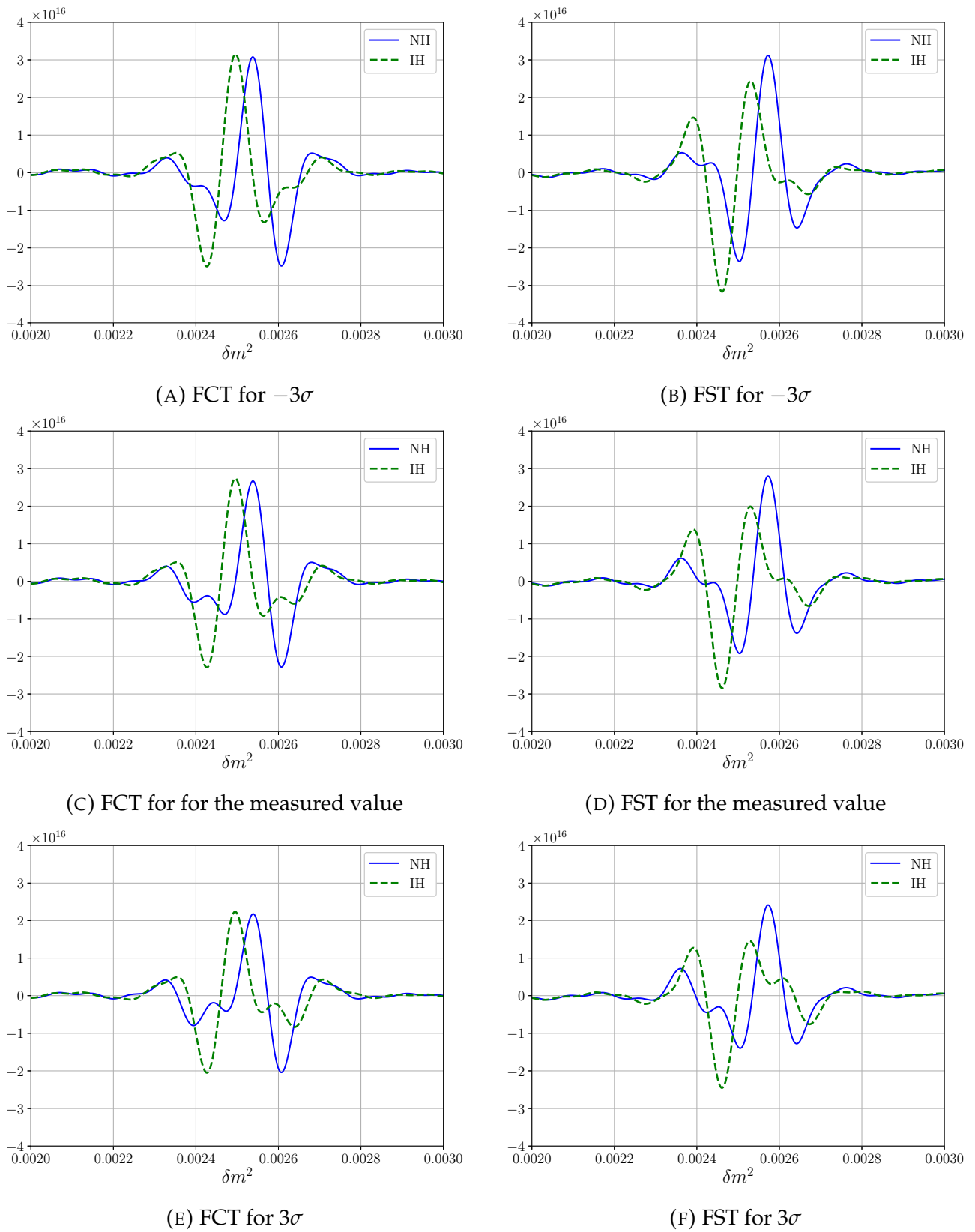
FIGURE 3.14: The Fourier transforms FCT (left plots) and FST (right plots) for various values of the $sin^2(\theta_{12})$ parameter : the measured value $-3\sigma$ (top), the measured value (middle) and the measured value $+3\sigma$ (bottom).
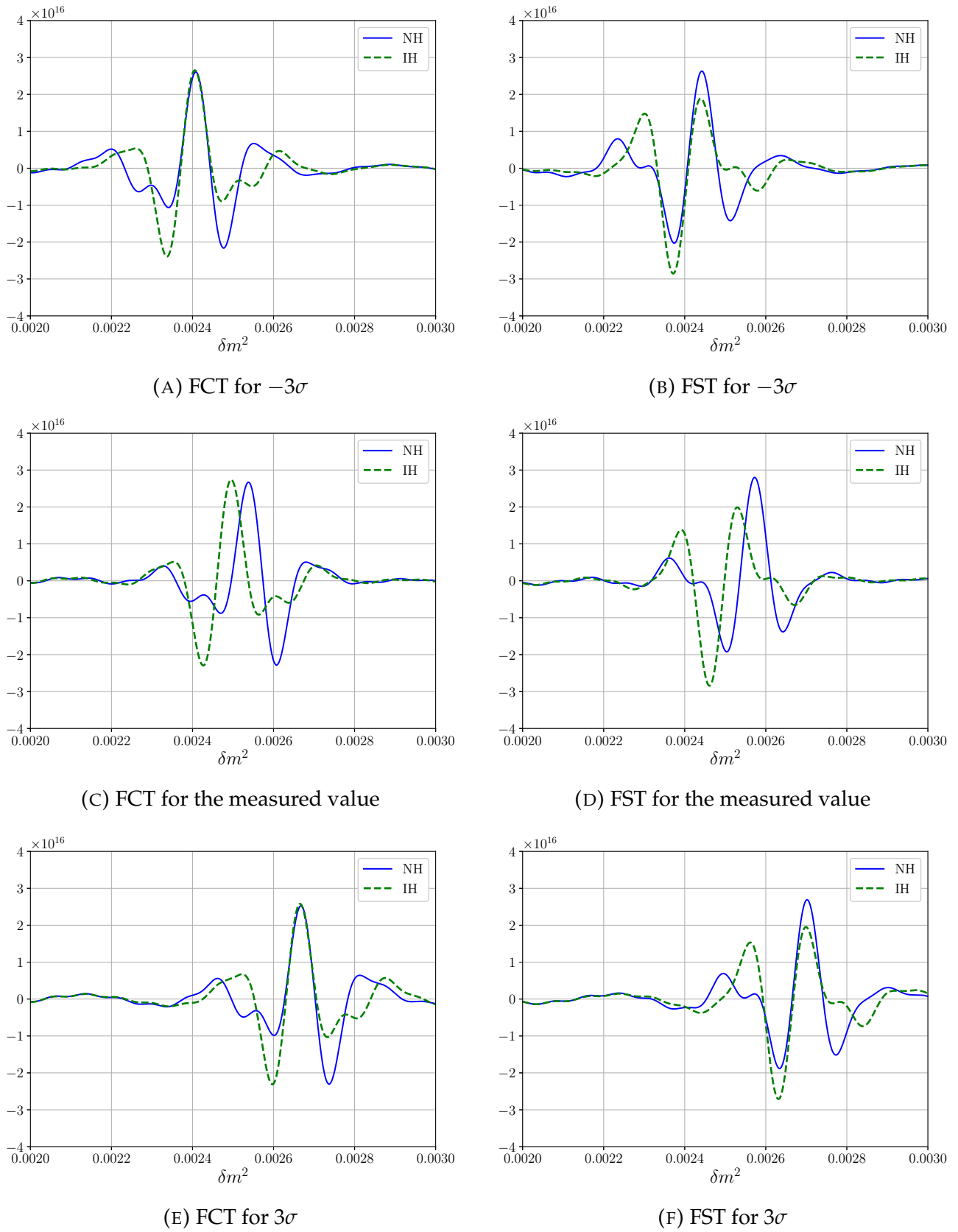
FIGURE 3.15: The Fourier transforms FCT (left plots) and FST (right plots) for various values of the $\Delta m^2$ parameter : the measured value $-3\sigma$ (top), the measured value (middle) and the measured value $+3\sigma$ (bottom).

(A) FCT for $-3\sigma$

(B) FST for $-3\sigma$

(C) FCT for $-3\sigma$

(D) FST for $-3\sigma$

(E) FCT for $3\sigma$

(F) FST for $3\sigma$
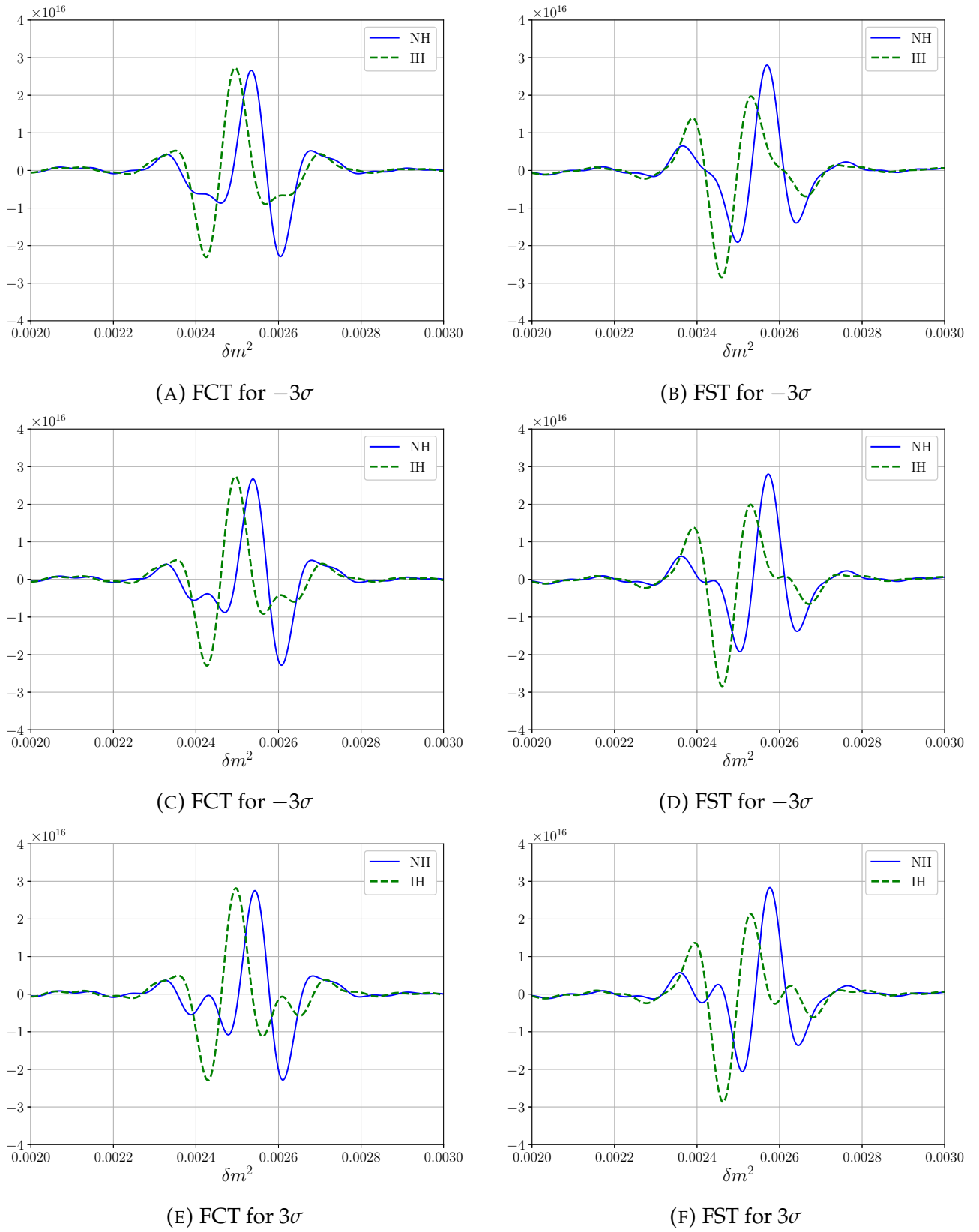
FIGURE 3.16: The Fourier transforms FCT (left plots) and FST (right plots) for various values of the $\Delta m_{21}^2$ parameter : the measured value $-3\sigma$ (top), the measured value (middle) and the measured value $+3\sigma$ (bottom).

# Chapter 4

# Monte Carlo simulation

*In this chapter, we present the Monte Carlo simulations to generate pseudo-experiments. We generalize the Fourier transforms defined for a continuous energy spectra to a discrete energy spectra. We implement a Gaussian incertitude to simulate errors on the anti-neutrino energy from the data acquisition system. We study the impact of the anti-neutrino energy resolution on the Fourier transform distributions.*

## 4.1   Monte Carlo principle

The name Monte Carlo was applied to a class of mathematical methods first used by scientists working on the development of nuclear weapons in Los Alamos in the 1940s. Monte Carlo Simulation is a mathematical technique that generates random variables to give a solution using probabilistic methods to non-probabilistic problems [34].

In our case, we sample the anti-neutrino energy spectra F(E/L) using Monte Carlo methods (see chapter 3 in [34]). To sample this distribution we uniformly generate two random numbers x and y using a pseudo-random number generator (specifically the mrg32k3a generator [35]). x is the energy value chosen in the [1.8, 8.0 MeV] energy range. We have chosen this energy interval to be able to compare the theoretical values of the FST and FCT to the value generated using the Monte Carlo simulation. y is generated in the [0.0, 0.1] range and gives the amplitude of the energy spectrum of the anti-neutrino flux (see figure 3.7a).

The rejection rule is the following : If the value that y takes is lower than the value of the theoretical oscillation energy spectrum (F(x/L) (see equation 3.1) we consider this couple of number as an event (as explained in section 2.2), otherwise we reject it. An example is seen in figure 4.1.

We divide the energy interval [1.8, 8 MeV] into a certain number of bins. A bin takes a hit if, for an event (x,y), x falls within the energy interval of the bin. The histograms in figure 4.2 represent each bin as a blue bar. The height of each bar gives of the number of hits of the bin. The Monte Carlo simulation allow to study how the statistical error affects the discrimination between the two mass hierarchies (see below).

To continue the analysis according to chapter 3, we have to compute the discrete Fourier sine and cosine transforms of the spectrum. The integral over L/E is converted to a sum over
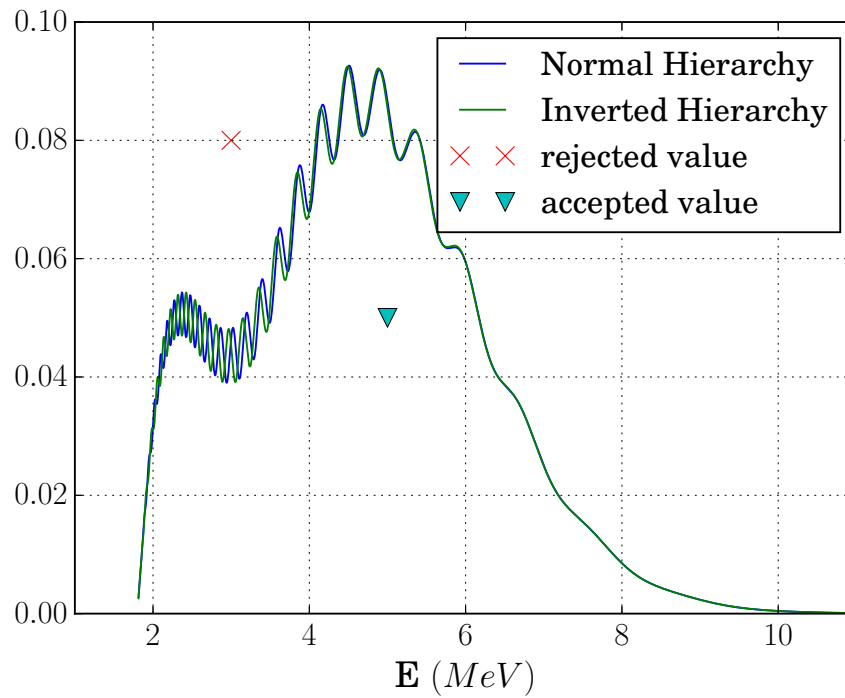
FIGURE 4.1: Example of the Monte Carlo process. The energy spectra for NH (in blue) and for IH (in green) are represented for a distance of 53 km.



(A) NH



(B) IH
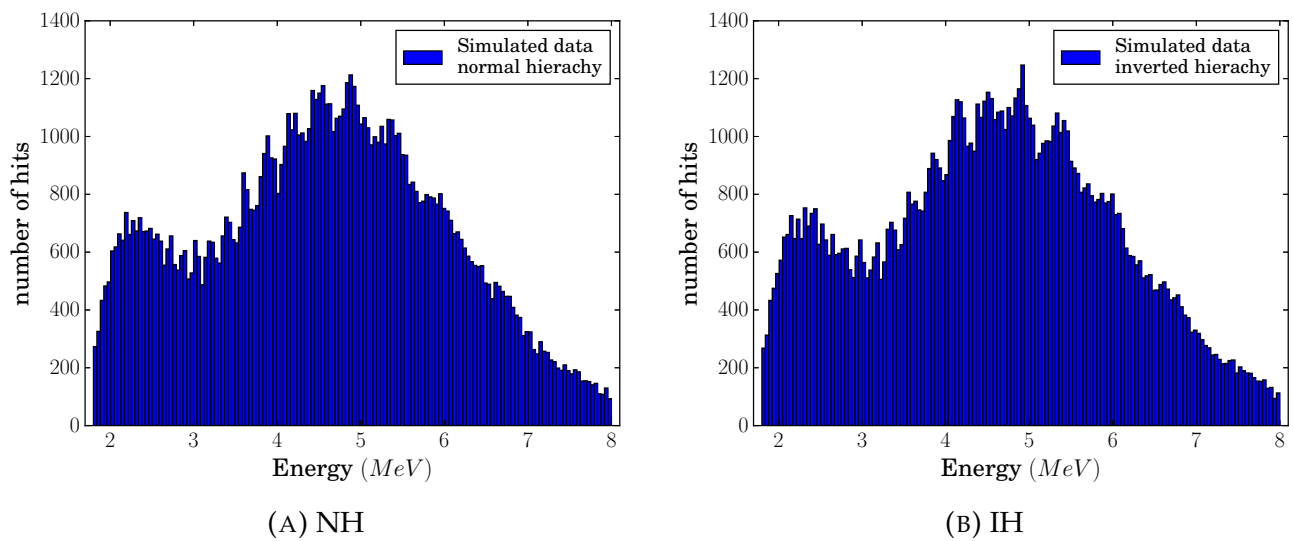
FIGURE 4.2: Histograms of 100 000 events simulated by Monte Carlo method for the normal (left) and inverted (right) neutrino mass hierarchies.

(A) FCT                (B) FST
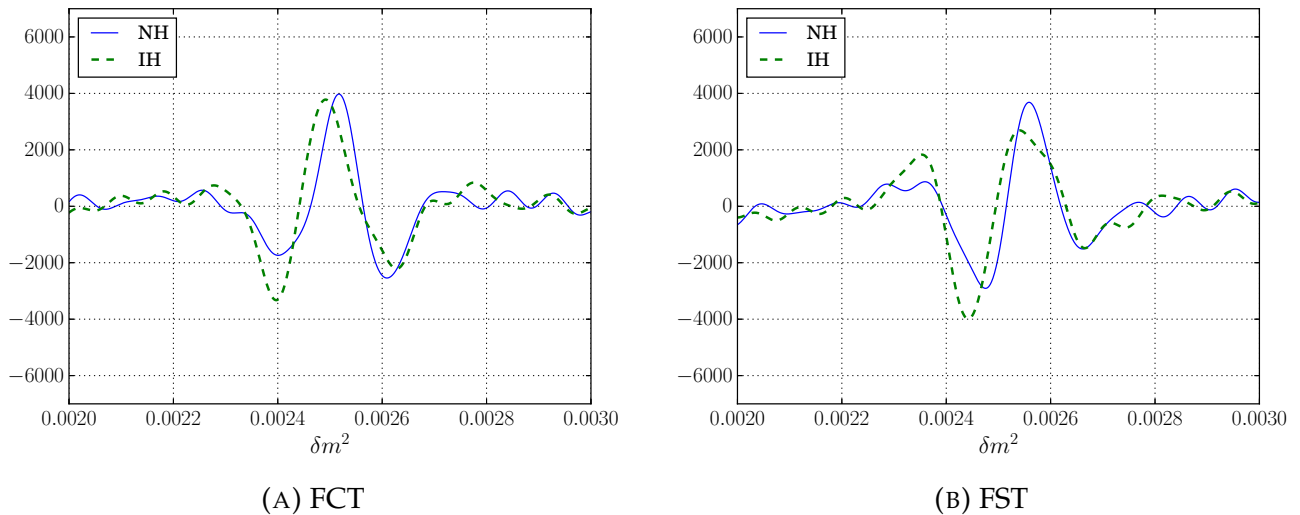
FIGURE 4.3: Fourier cosine (left) and Fourier sine (right) transforms of the discrete spectra of figure 4.2 with prefect energy resolution and 150 bins.

all the events as follows:

$$FCT(\omega) = \int_{t_{min}}^{t_{max}} F(t)cos(\omega t)dt \rightarrow FCT_{disc}(\omega) = \sum_{i}^{N_{event}} cos(\frac{\omega L}{E_i}) \tag{4.1}$$

and

$$FST(\omega) = \int_{t_{min}}^{t_{max}} F(t)sin(\omega t)dt \rightarrow FST_{disc}(\omega) = \sum_{i}^{N_{event}} sin(\frac{\omega L}{E_i}) \tag{4.2}$$

Applying the formula 4.1 and 4.2 to simulated data (in figure 4.2) we obtain discrete Fourier transforms. In figure 4.3a, we have the Fourier cosine transform and in figure 4.3b the Fourier sine transform. Comparing figures 3.8 and 4.3 we see that the Fourier transform depends on the methods being used. The main difference is due to the fact that Monte Carlo technique has statistical errors, distinguishing it from the theoretical methods. This is interesting in our case as it reproduces the reality of detection system.

## 4.2 Impact of the energy resolution on the shape of the Fourier transforms

The resolution affects the results the simulations into two ways. The first one is the number of chosen bins. This is a fixed parameter chosen before each simulation. It affects the resolution as it defines the degree of discretization of the energy interval. The important point is that events with different energies will be put in the same small discrete interval and this leads to error on the Fourier transforms.

The other factor influencing the resolution is the Gaussian error of the detector. Indeed, in order to simulate results close to those ones produced by actual particle detectors, we

brought a slight modification to the Monte Carlo technique as explained in Section 4.1. We simulate a Gaussian distribution (via its standard deviation) around each x point.

### 4.2.1 Impact of the number of bins

To study the impact of the number of bins, we vary the number of bins in the pseudo-experiments. To make the graph more clear we consider no Gaussian energy resolution in these simulations. We started the numerical experiments with a small number of bins. Figure 4.4a shows the histogram of the energy spectrum for NH when the number of bins is set to 100. Figure 4.4b is a zoom of figure 4.4a in the energy interval [1.8, 4 MeV]. We chose this interval for the fine oscillation pattern in it. With this small number of bins the oscillation pattern is vanishing. Comparing this histogram to the energy spectra in figure 4.1 we see that some of the finest oscillations have disappeared. Indeed large bin takes the mean value of the oscillations.

Figures 4.5a and 4.5b[1] show the histogram of the NH energy spectrum in the energy interval [1.8, 4 MeV], when the number of bins is set to 150 and 200 respectively. They both give an accurate representation of the energy spectra of figure 4.1. We conclude that in our simulation 150 bins are high enough to see the oscillation pattern. It is also important to notice that increasing the number of bins beyond a certain limit does not make sense as it implies that the detectors measure energy levels with an arbitrarily high precision. 200 bins correspond to a energy resolution of 3% which will be the maximum obtained in JUNO experiment.

The graphs in figure 4.6 represent the Fourier cosine transforms in the case of 100 bins (left) and of 150 bins (right). In the case of 100 bins, we observe more oscillations than in the 150 case. We conclude as the number of bins decreases, this results in a smoother curve and in additional frequencies appearing in the Fourier transforms.

### 4.2.2 Impact of the Gaussian detection resolution

We study the impact of the Gaussian resolution in our simulations while fixing the number of bins to 150. Figure 4.7a shows the histogram of the energy spectrum for NH with a Gaussian energy resolution of 0.01. With this small resolution the histogram represents the energy spectrum in figure 4.1 fairly accurately. The increase of the resolutions (worst resolution) makes a worst representation of the energy spectrum as we see comparing figures 4.7b and 4.7d. The oscillations are still present (even the finest ones), however their amplitudes is less clear. The reason behind this observation is that higher resolution (higher standard deviation) leads to a energy value of an event falling more frequently in the wrong bin. Therefore the number of hits per bin is more uniformly distributed.

The graphs in figure 4.8 represent the Fourier cosine transforms for the case of a resolution of 0.01 (left) and 0.03 (right). As the resolution increases (become worst) the figures are more deformed compared to the Fourier transforms of the energy spectra in figure 4.3. Moreover the difference between the NH and IH curve becomes less apparent which leads to difficulties in discriminating the mass hierarchy, for the same reason as above.

---

[1]The complete set of the following figures is presented in A.
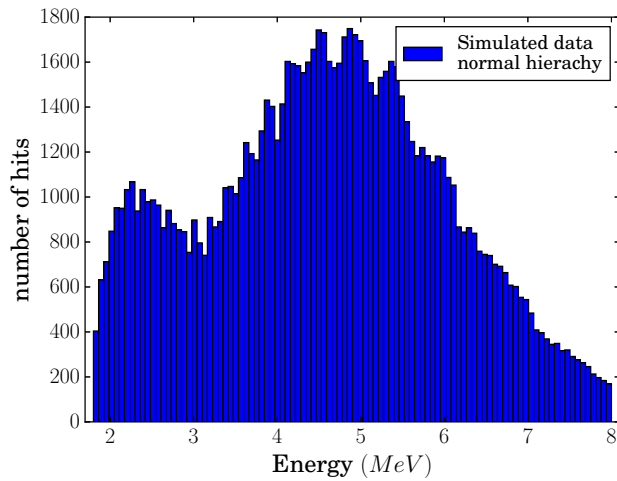
(A) NH and 100 bins
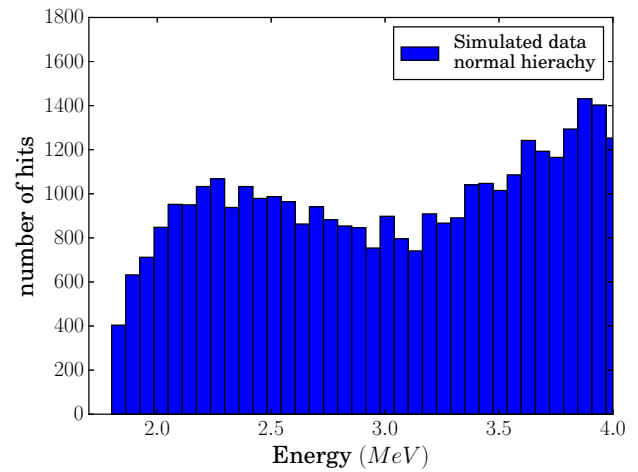
(B) Zoom of figure 4.4a
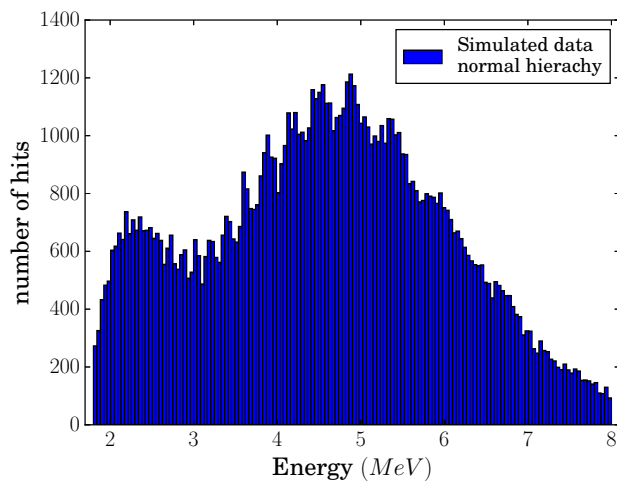
(C) NH and 150 bins
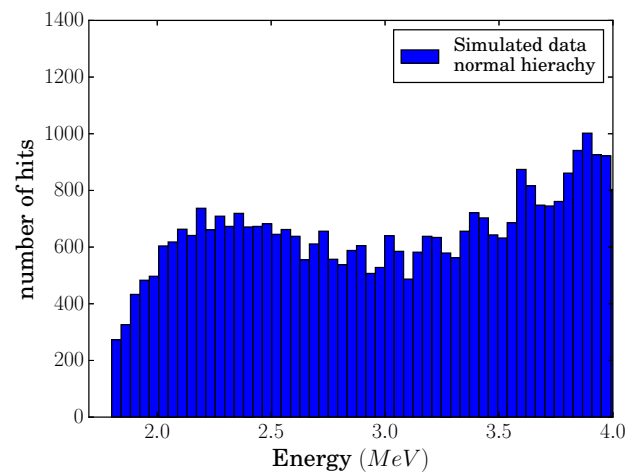
(D) Zoom 4.4c

FIGURE 4.4: Histogram of the Monte Carlo simulation for different binnings: 100 and 150. The number of events is 100 000 and we have a infinite resolution. The plot for the energy interval [1.8, 8 MeV] (right) and zoom for the energy interval [1.8, 4 MeV] (left).

(A) NH and 150 bins

(B) NH and 200 bins
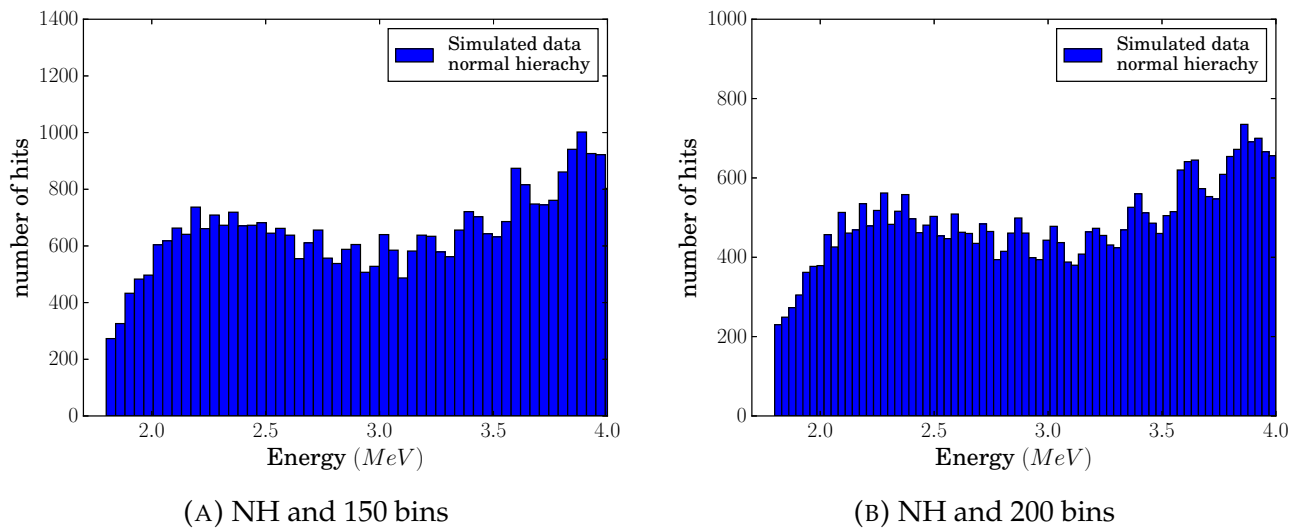
FIGURE 4.5: Histograms of the Monte Carlo simulation for different binnings: 150 and 200. The number of events is 100 000 and we have a infinite resolution.
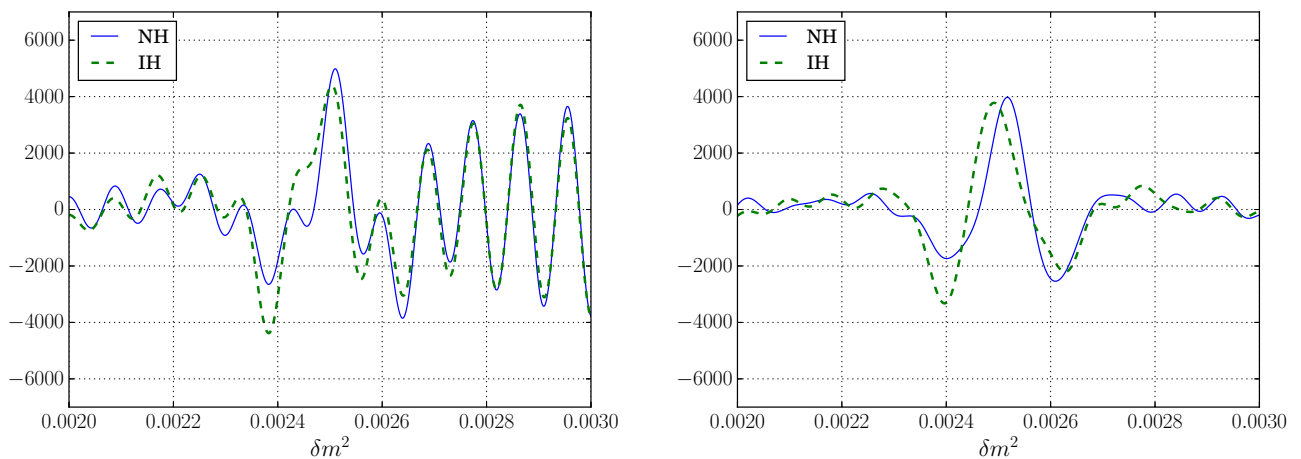


(A) FCT for a binning of 100

(B) FCT for a binning of 150

FIGURE 4.6: FCT spectra simulated by Monte Carlo simulation for different binnings: 100 and 150. The number of events is 100 000 and we have a infinite resolution (see appendix C to complete set of figures).
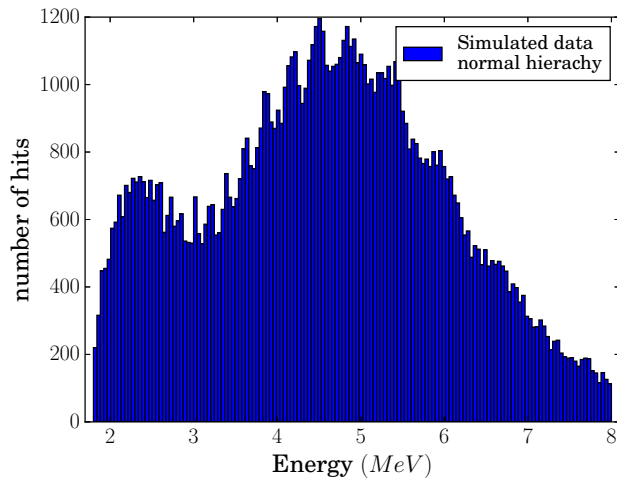
(A) NH and resolution of 0.01
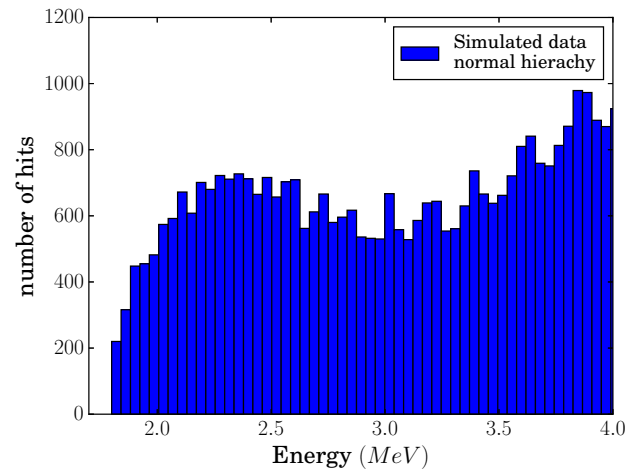


(B) Zoom of figure 4.7a
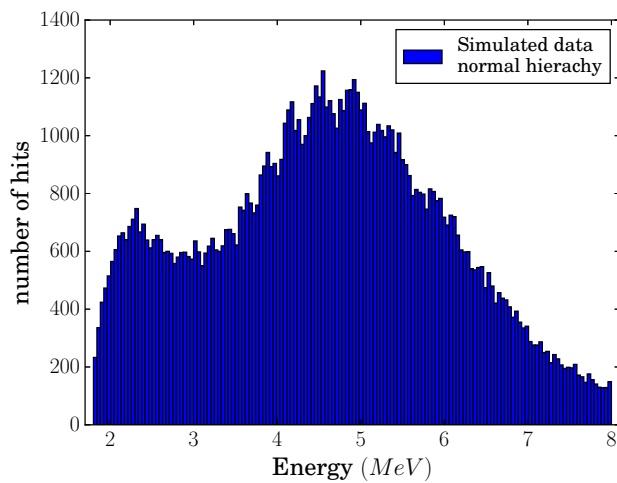


(C) NH and resolution of 0.03
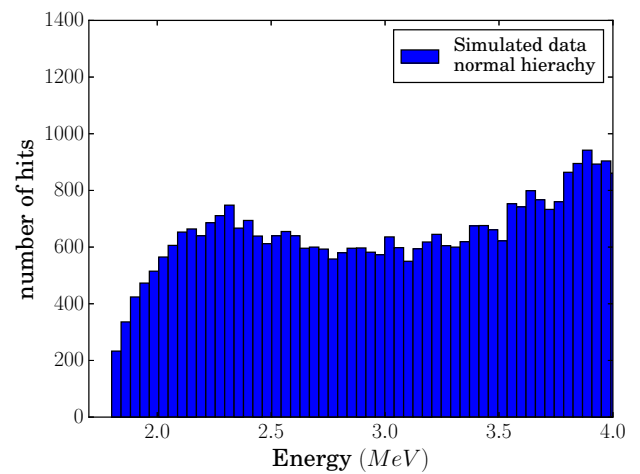


(D) Zoom of figure 4.7c

FIGURE 4.7: Histograms of the Monte Carlo simulation for a resolution of 1% (top) and 3% (bottom). The number of events is 100 000 and the number of bins is 150. The plot for the energy interval [1.8, 8 MeV] (right) and zoom for the energy interval [1.8, 4 MeV] (left).

(A) FCT for resolution of 0.01

(B) FCT for resolution of 0.03
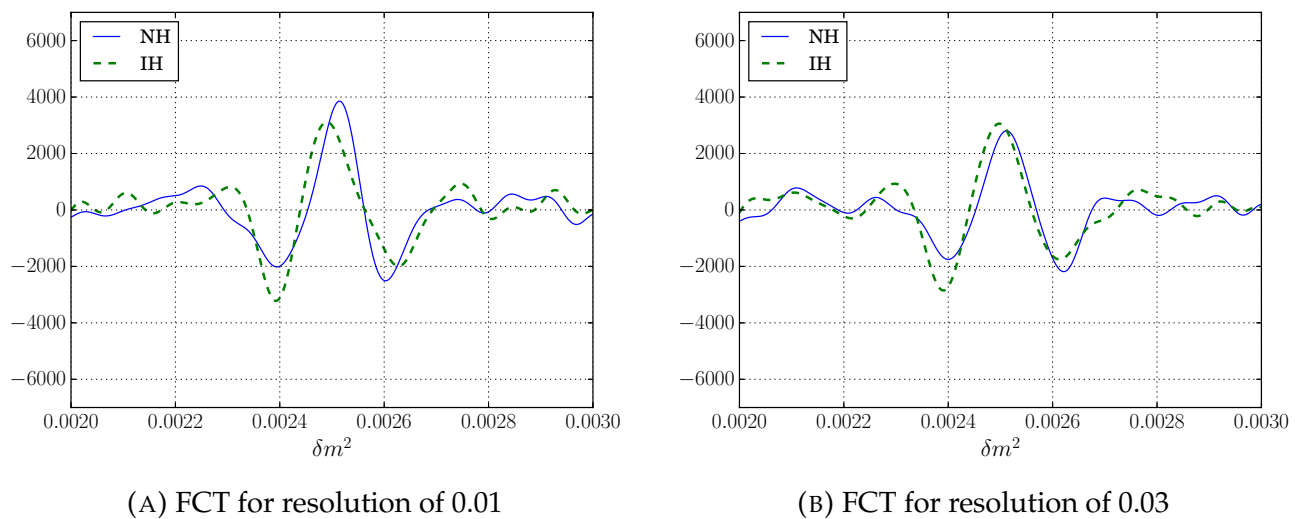
FIGURE 4.8: FCT spectra simulated by Monte Carlo simulation for different resolutions: 1% and 3%. The number of events is 100 000 and we have a number of bins equal to 150 (see appendix C to complete set of figures).

# Chapter 5

# Analysis of the Monte Carlo simulations

*In this chapter we compute the probability of discrimination between the two cases of mass hierarchy. We also analyze the impact of the 4 most important parameters of the simulation: the distance between the electronic anti-neutrino source and the detector, the parameter $\sin^2(\theta_{13})$, the anti-neutrino energy resolution and the number of events, on the discrimination probability.*

## 5.1 Principle

In chapter 4 we have built a Monte Carlo simulation in which each event corresponds to an inverse $\beta$-decay interaction resulting in the detection of an electronic anti-neutrino. To evaluate the neutrino mass hierarchy discrimination probability, we use the parameters PV and RL defined in section 3.3.3. We use the Monte Carlo simulations to evaluate the distribution of the parameters PV and RL. For each set of parameters, we perform 2000 simulations. For each of them we compute the FCT and FST spectra and deduce the values of PV and RL. The distribution of these two parameters is represented in two different ways in figure 5.1.

Figure 5.1a shows PV as function of the parameter RL. The two hierarchies form two distinguishable clouds but it does not allow to determine a distribution law. The histogram in figure 5.1b addresses this previous issue by transforming the graph using the technique already seen in paper [36]. We draw a histogram of the blue (resp. green) points where the x-axis represents the sum of the PV and RL coordinates of blue (resp. green) points of the cloud. The resulting distribution is fitted by a Gaussian distribution. With this feature, we are able to compute the neutrino mass hierarchy discrimination probability.

Assuming a normal hierarchy, we compute the validation probability of this hypothesis with our numerical experiment. We first fit the PV+RL histogram with a Gaussian distribution. Figure 5.2a shows the interpolation with a Gaussian function. We denote the distribution in the NH case as $N(PV + RL)$ and the distribution in the IH case as $I(PV + RL)$.

We now fix the confidence level at $3\sigma \approx 99.73\%$. We define the discrimination probability at $3\sigma$ as the following integral:

$$\mathcal{P}(\sigma) = \int_{x(\sigma)}^{\infty} N(PV + RL)d(PV + RL) \tag{5.1}$$

where $\sigma$ is the confidence interval, $x(\sigma)$ (the vertical black line in figure 5.2b) is the value PV+RL such as $I(PV + RL) = \sigma$. $I(PV + RL)$ is the green line in figure 5.2b and $N(PV + RL)$ the blue curve. The integral defined in equation 5.1 corresponds to the colored area in figure 5.2b. If the two clouds of figure 5.1a are well distinguishable, the two Gaussian distributions of figure 5.2a do not overlap and result resulting in a discrimination probability of value 1.



(A) PV as function of RL.

(B) Histogram of PV+RL.
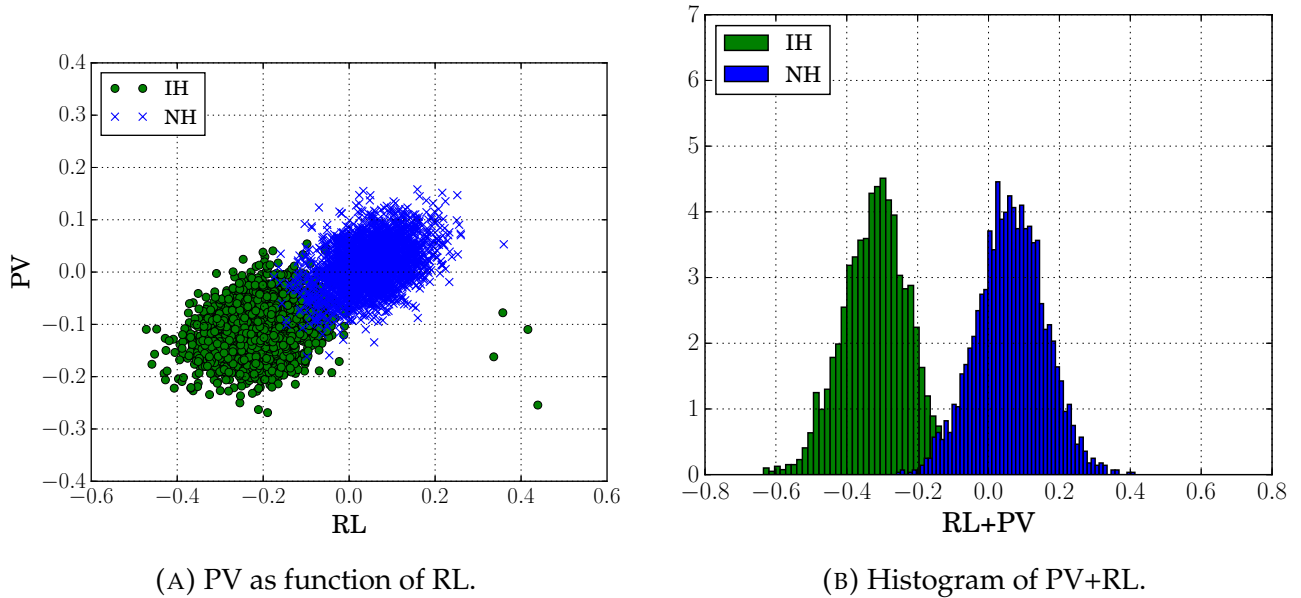
FIGURE 5.1: Simulation of 2000 experiments of 100 000 events each to study the distribution of the parameters PV and RL with a resolution of 4% at 1 MeV.



(A) Histogram of PV+RL with a Gaussian fit.

(B) Gaussian fits of the histograms.
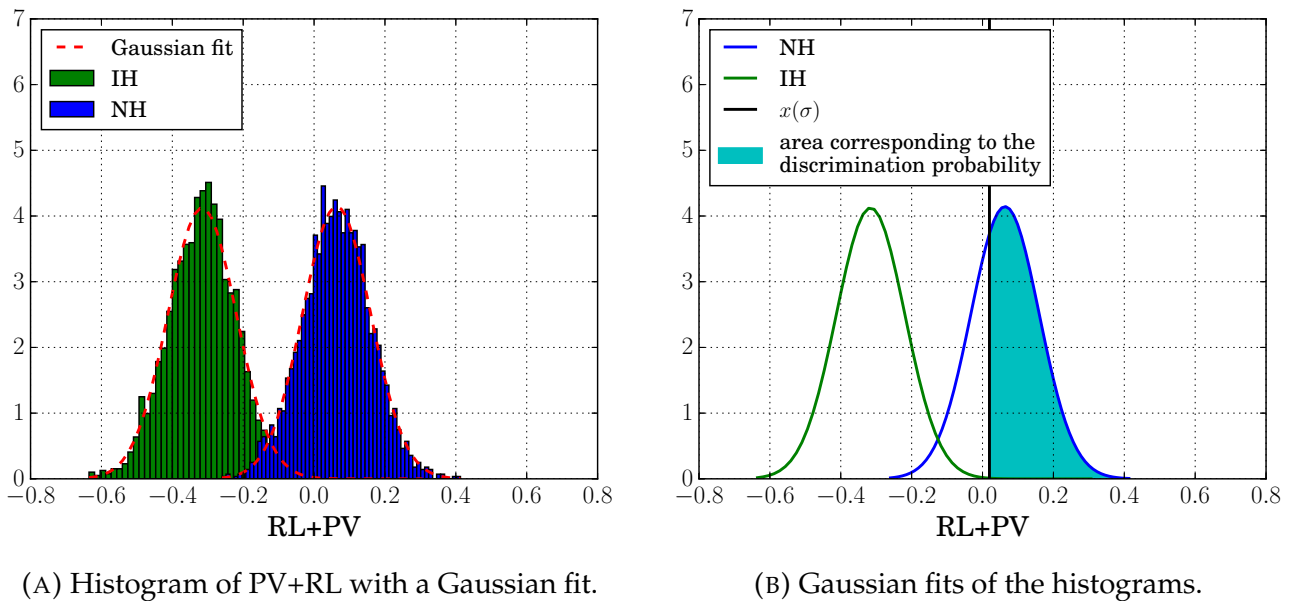
FIGURE 5.2: Simulation of 2000 experiments of 100 000 events each to study the distribution of the parameters PV and RL with a resolution of 4% at 1 MeV. The blue area is the integral defined in equation 5.1 that representing the discrimination probability.
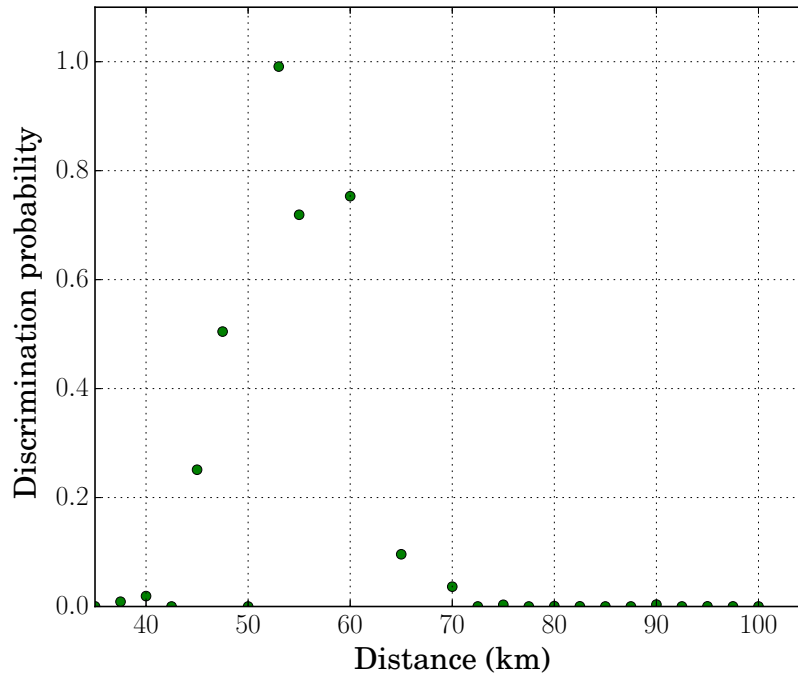
FIGURE 5.3: Discrimination probability at $3\sigma$ as a function of the distance between the anti-neutrino source and the detector. The other parameters are the standard ones: the detector resolution equal to 3% at 1 MeV, $sin^2(\theta_{13})$ equal to the measured value and number of events for each simulation equal to 100 000.

## 5.2 Impact of the distance

In figure 5.3 we have plotted the discrimination probability as a function of the distance between the anti-neutrino source and the detector. We note that only a distance of 53 km gives a discrimination probability close to 1. The discrimination probability decreases when the distance deviates from 53 km. The shape of the data plots is explained by comparing the Fourier transforms in figure 3.12 . For instance, for a distance of 35 km, the difference between the valleys of the blue curve are the same as those of the green curve resulting in very similar PV+RL values. Consequently, as shown in figure 5.4 , the two histograms overlap strongly resulting in a small value for the discrimination probability. However, the exact opposite happens at a distance of 53 km. Indeed, as shown in figures 3.12c and 3.12d, the RL and PV values are positive in the NH but negative in the IH.The same reasoning applies to the other distances. The only peculiar behavior happens at a distance of 50 km where unexpectedly the discrimination probability has a very small value. This results from of a second green cloud appearing due to statistical errors, as shown in figure 5.5 . Note that the distance chosen for the JUNO facility is 53 km to have the maximum discrimination probability.
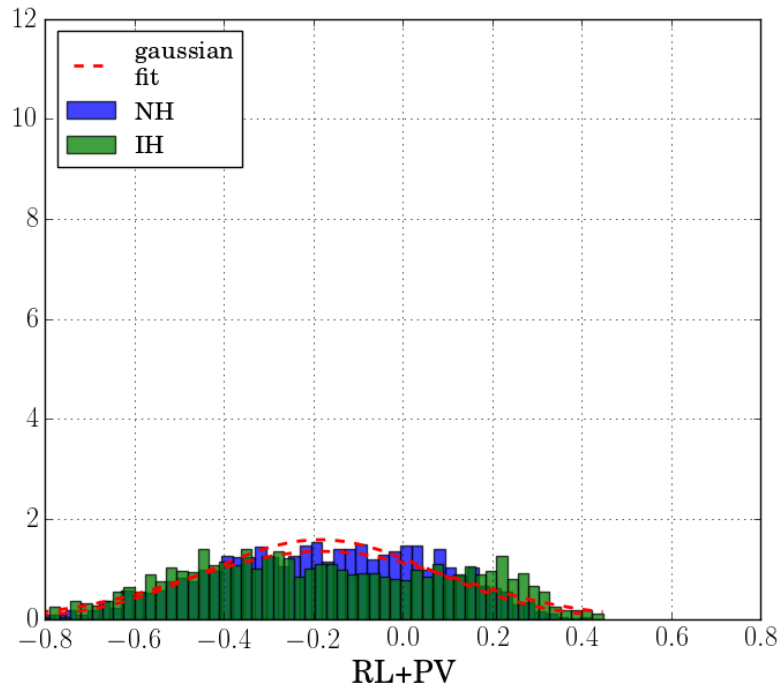
FIGURE 5.4: PV+RL plots for 2000 experiments of 100 000 events each, resolution of 3% at 1 MeV, a distance of 35 km and the measured value for $sin^2(\theta_{13})$.
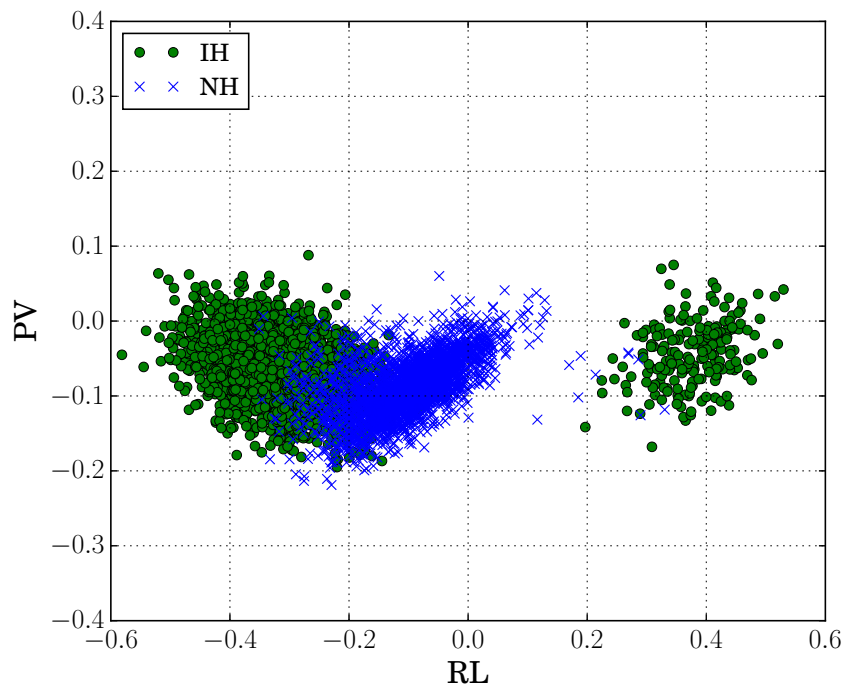


FIGURE 5.5: PV+RL plots for 2000 experiments of 100 000 events each, resolution of 3% at 1 MeV, a distance of 50 km and the measured value for $sin^2(\theta_{13})$.
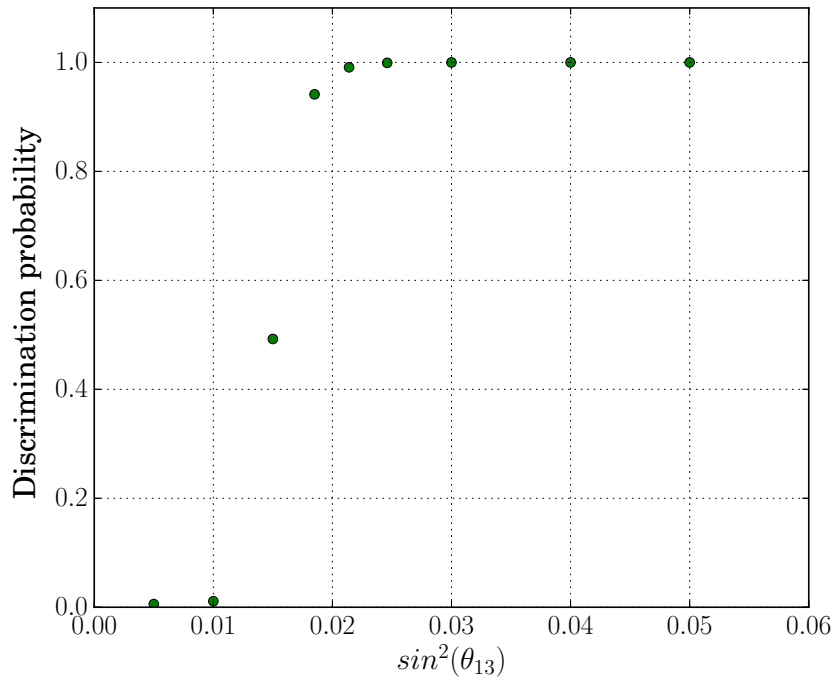
FIGURE 5.6: Discrimination probability at $3\sigma$ as a function of the parameter $sin^2(\theta_{13})$. The other parameters are the standard ones: the detector resolution equal to 3% at 1 MeV, the distance between the anti-neutrino source and the detector equal to 53 km, number of events for each simulation equal to 100 000.

## 5.3 Impact of the parameter $sin^2(\theta_{13})$

In figure 5.6 we have plotted the discrimination probability as a function of the parameter $sin^2(\theta_{13})$. The reason behind the behavior of the points on the graph can be explained by comparing their corresponding FCTs and FSTs. Some of these graphs are shown in figure 3.13. We observe that as $sin^2(\theta_{13})$ increases, the amplitude of Fourier transform becomes larger and therefore the blue and green histograms are more separated. We see that at the expected value of $sin^2(\theta_{13})$ the discrimination probability is close to 1.

## 5.4 Impact of the resolution and the number of events

In figure 5.7 we have plotted the discrimination probability as a function of the resolution of the detector. The shape of the data plot can be explained by comparing their corresponding FCTs and FSTs. Some of these graphs are shown in figure 4.8. We observe that as resolution decreases, discrete Fourier transforms are closer to the theoretical Fourier transforms are therefore the blue and green histograms are more separated. At the expected value of resolution (3% at 1 MeV) the discrimination probability is near 1. Note that minor changes of this parameter to its value have a huge effect on the discrimination probability. Thus important choice have to be made while designing a detector (see chapter 2).
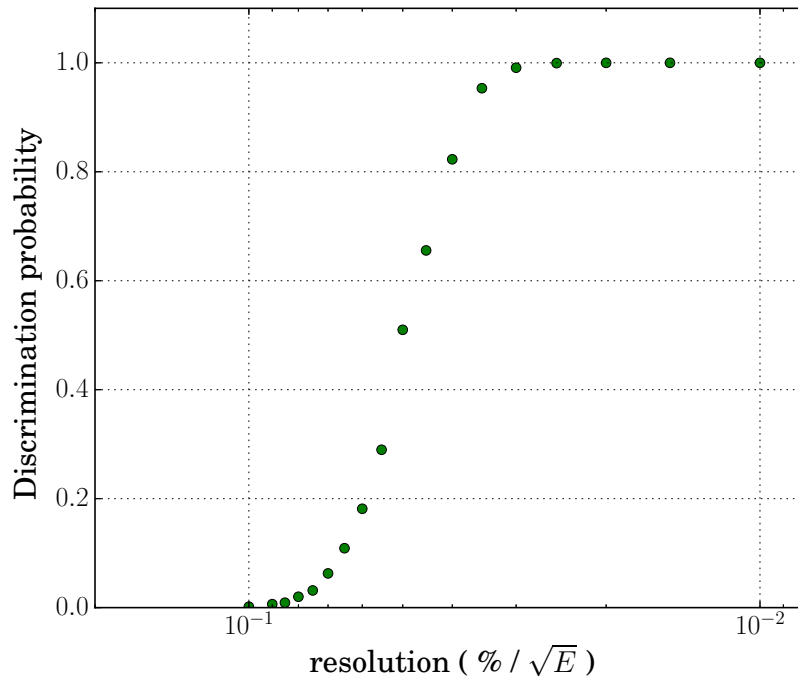
FIGURE 5.7: Discrimination probability at $3\sigma$ as a function of the detector resolution. The other parameters are the standard: the distance between the anti-neutrino source and the detector equal to 53 km, $sin^2(\theta_{13})$ equal to the measured value and number of events for each simulation equal to 100 000.

In figure 5.10 we have plotted the discrimination probability as a function of the number of events. We corroborate it by comparing the corresponding FCTs and FSTs. Some of these graphs are shown in Figure 5.8. We observe that as the number of events increases, the amplitude of the discrete Fourier transforms increases while their unwanted oscillations decrease. These unwanted oscillations are due to statistical error. As shown in figure 5.9, these two effects make the distinction between the green and the blue clouds easier and eliminate the parasitic cloud due statistical error. In turn, the discrimination probability increases.

As a remark, the number of events is determined by the time during which the detector is taking data, the size of the detector and the incoming anti-neutrino flux from the nuclear plants.

We conclude this section by highlighting the difference between the resolution of the detector and the number of the events. The comparison of figure 5.7 and figure 5.10, shows that the discrimination probability grows faster with the resolution than the number of events. In a practical point of view, this means that while designing detectors, we could increase the discrimination probability more easily by lowering the resolution rather than increasing the number of events.
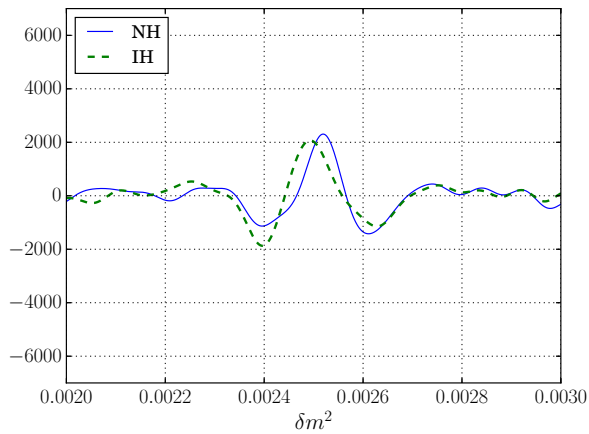
(A) FCT for a number of events =50 000
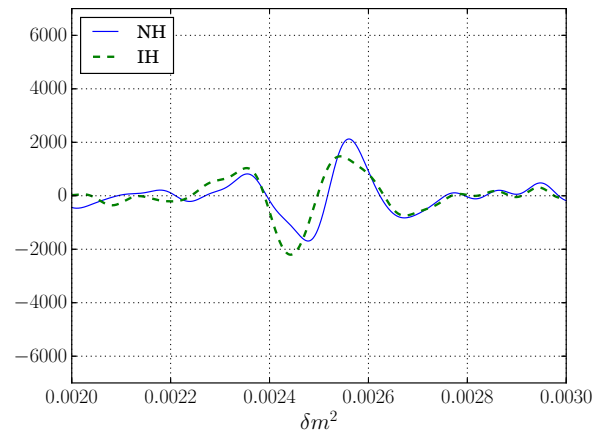
(B) FST for number of events =50 000
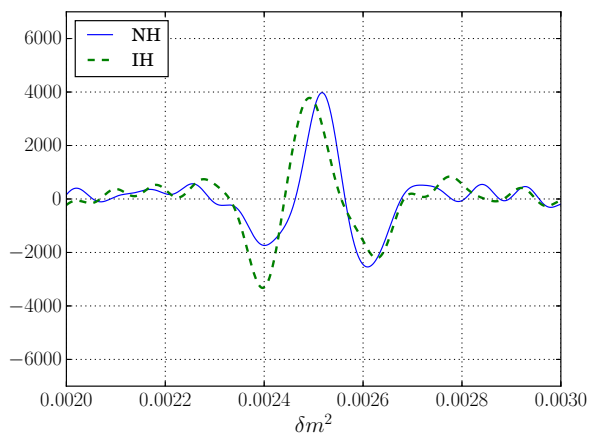
(C) FCT for number of events =100 000
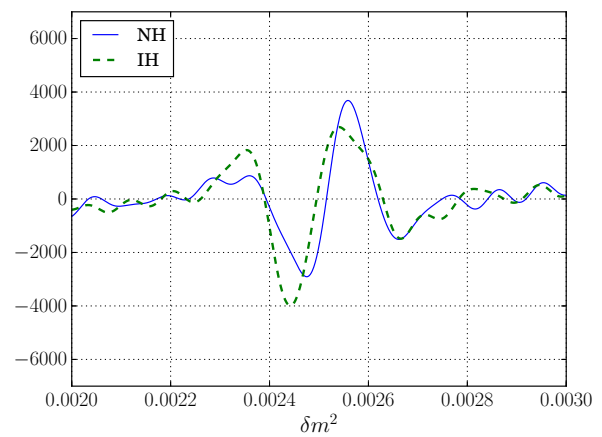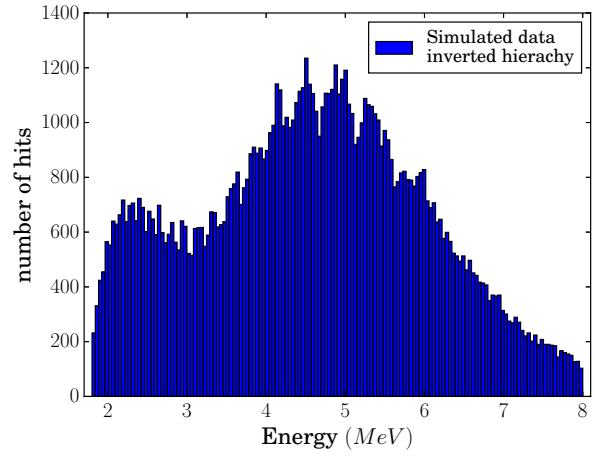
(D) FST for a number of events =100 000
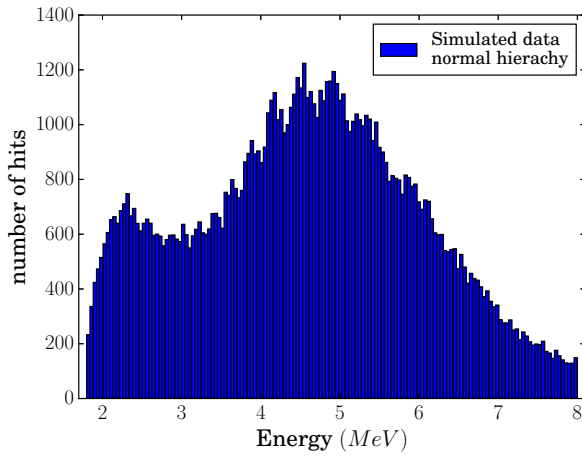
FIGURE 5.8: Shape of the Fourier transform of the spectrum simulated by Monte Carlo simulation for different number of events: 50 000, 100 000 and 150 000. The resolution is 3% at 1 MeV and we have a have chosen a binning of 150.

(A) PV+RL plots for a number of events = 50 000

(B) PV+RL plots for a number of events = 100 000
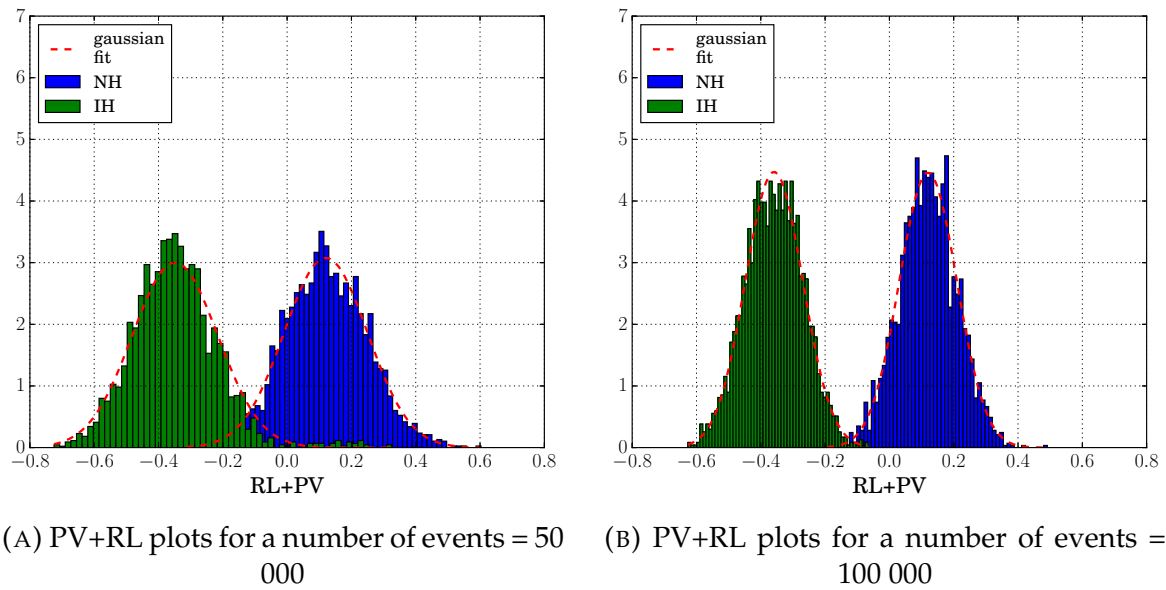
FIGURE 5.9: PV+RL histograms for the two neutrino mass hierarchies. With a number of simulations of 2000 experiments of with a number of events 50 000 and 100 000. The resolution is the standard 3% at 1 MeV for a distance of 53 km and the measured value for $sin^2(\theta_{13})$.
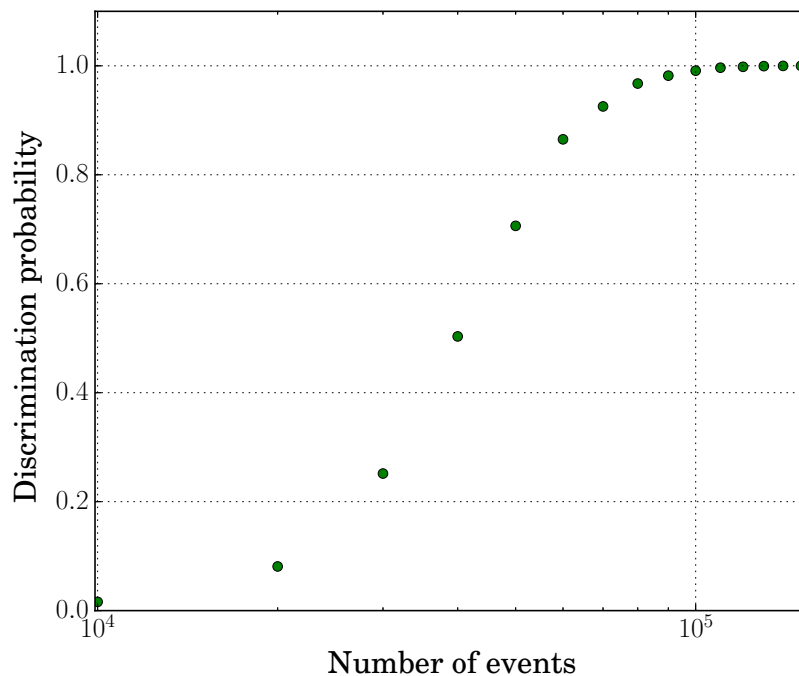


FIGURE 5.10: Discrimination probability at $3\sigma$ as a function of the number of events. The other parameters are the standard ones: the detector resolution equal to 3% at 1 MeV, the distance between the anti-neutrino source and the detector equal to 53 km and $sin^2(\theta_{13})$ equal to the measured value.

# Conclusion

Monte-Carlo simulations of this present work shows that the experimental set-up of the JUNO detector - i.e., 100,000 events, a distance between the source and the detector of 53 km, an energy resolution of 3% at 1 MeV, will allow the accurate measurement of the neutrino mass hierarchy with a confidence level of 3 $\sigma$, in the inverse $\beta$-decay process where electronic anti-neutrinos produced by the nuclear plant are detected when they interact with protons.

By using the data from KamLand, we have expressed the neutrinos flux as a function of the anti-neutrino energy, with very little differences between the experimental data and the fitted function. We have also shown that a single isotope case is appropriate for performing the Monte-Carlo simulations. A parametrization of the theoretical values of the inverse $\beta$-decay cross section $\sigma(E)$ with a cubic polynomial function is used, as a function of the energy of the anti-neutrino.

A formulation of the oscillation probability with the mass hierarchy terms has been derived to express the spectra of the JUNO detector as a function of the energy (MeV) and L/E (km/MeV) for both the normal and the inverted hierarchy.

Fourier transforms have been applied to the different components of the oscillation probability (i.e., the solar oscillation, the first part of the atmospheric oscillation, the second part of the atmospheric oscillation). The atmospheric oscillation parts show important properties which can be used to differentiate between NH and IH. Indeed the shape of the Fourier cosine transform and Fourier sine transform are strongly different as function of the chosen mass hierarchy. Our study also shows that only measurement errors on one of the 4 parameters playing a role on the neutrino oscillation, i.e. : $sin^2(\theta_{13})$, did affect significantly the shape of Fourier transforms. To characterize the shape of these curves, the parameters PV and RL are defined. Moreover these parameters are especially convenient for the numerical simulations.

On the numerical side, Monte-Carlo simulations are intrinsically a very appropriate approach to validate the experimental set-up of the JUNO detector, as it replicates through a randomized numerical sampling, the actual data acquisition process. The statistical errors of our Monte Carlo techniques, as developed by randomly sampling the anti-neutrino energy spectra, did properly reproduce the measurement variability of JUNO detection system. 100,000 events falling in an optimal number of 150 simulation bins of the [ 1.8, 8 MeV] energy interval gets a fairly accurate shape of Fourier transforms and energy spectra.

Monte-Carlo calculations have been run to estimate the impact of 4 key parameters: 1- the distance between the nuclear plant and the detector, 2- the mixing angle $sin^2(\theta_{13})$ , 3- the number of events, 4- the resolution of data acquisition, along the whole process. For the value of these 4 factors as in the JUNO facility specifications, our calculation shows that the discrimination probability with a confidence level of 3 $\sigma$, is equal to 0.991. An important additional

insight, derived from the fact that discrimination probability grows faster with the energy resolution than with the number of events, means that while designing detector lowering, the measurement system resolution is more important than increasing the number of measurements.

As mentioned, this work did focus on the validation and the influence of the 4 most critical parameters of the JUNO experimental set-up on the mass hierarchy measurements. Further work should assess the influence of each experimental parameter of JUNO, such as PMT sensitivity, background noise, noise from electronic data acquisition system resolution, . . .

# Appendix A

# Graphics of impact of the energy resolution on the shape of the Fourier transforms of the spectrum
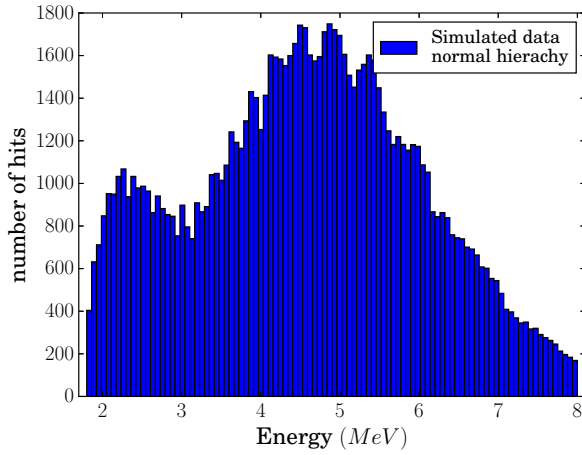
(A) NH and 100 bins
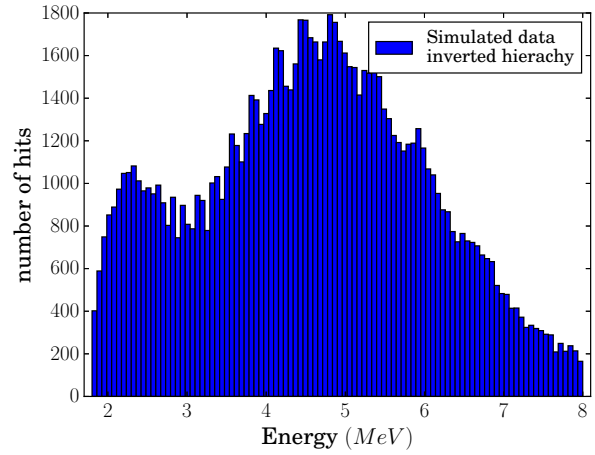
(B) IH and 100 bins
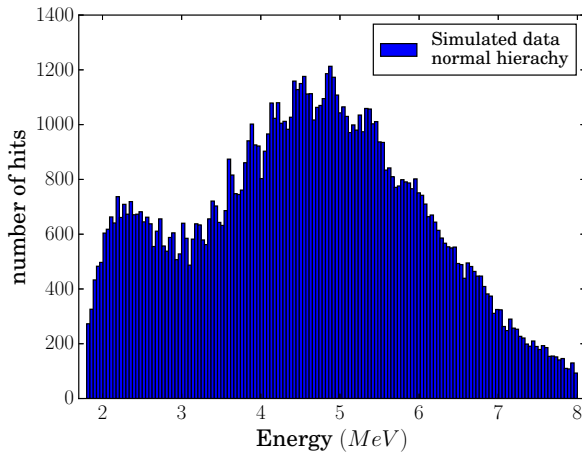
(C) NH and 150 bins
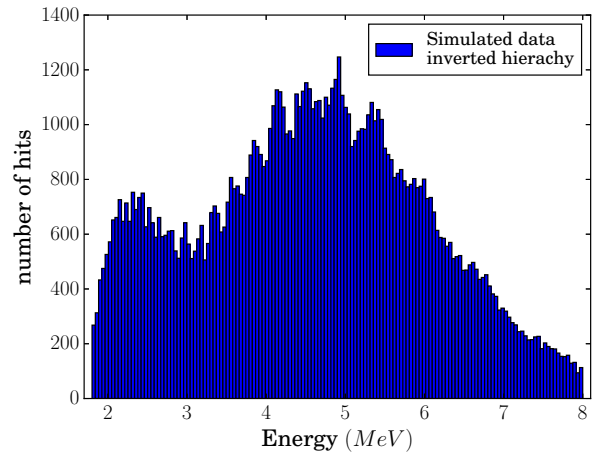
(D) IH and 150 bins
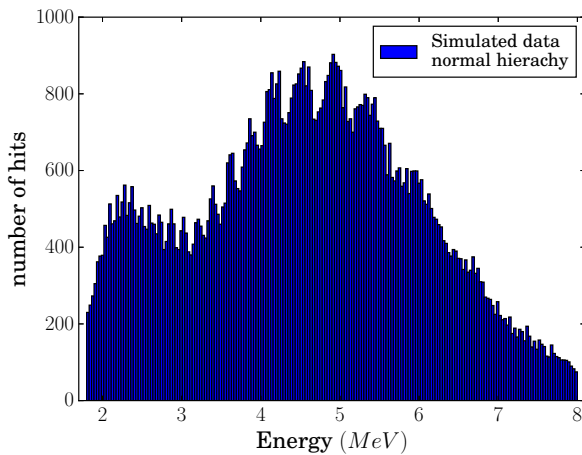
(E) NH and 200 bins
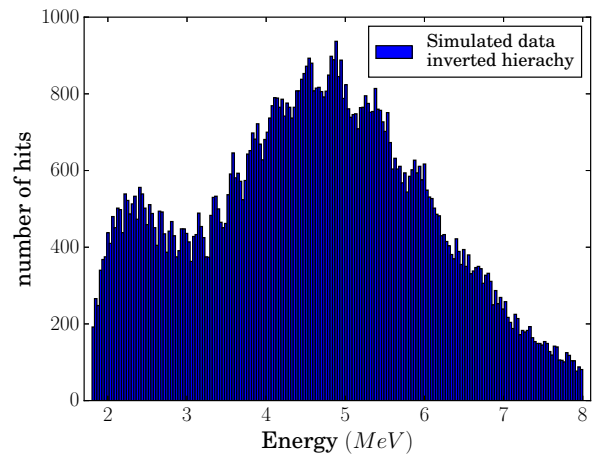
(F) IH and 200 bins

FIGURE A.1: Histogram of the Monte Carlo simulation for different binnings: 100, 150 and 200 The number of eventsis 100 000 and we have a infinite resolution.
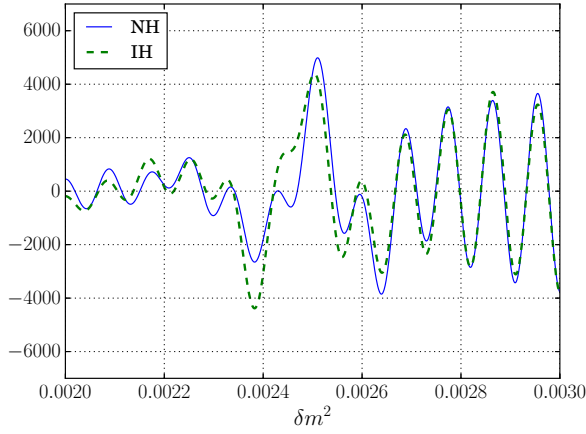
(A) FCT for a binning of 100
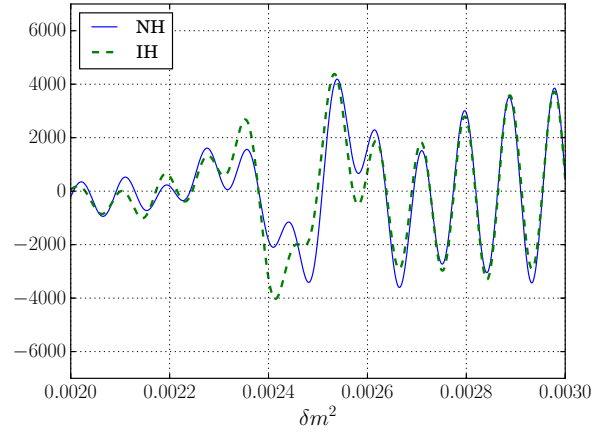
(B) FST for a binning of 100
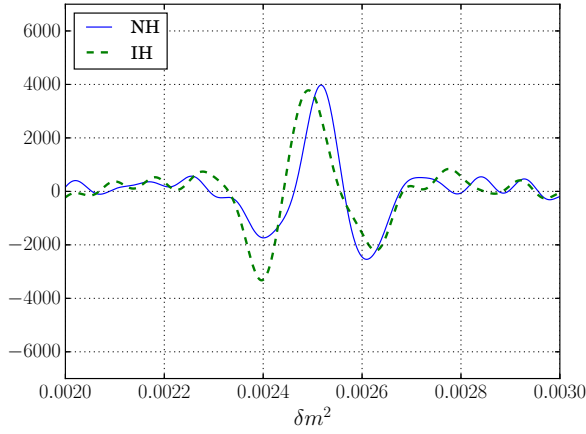
(C) FCT for a binning of 150
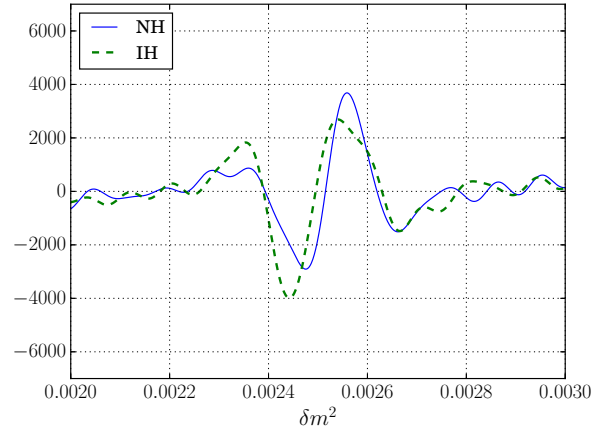
(D) FST for a binning of 150
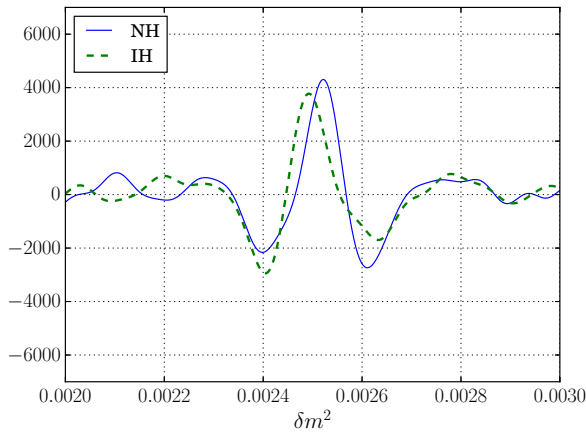
(E) FCT for a binning of 200
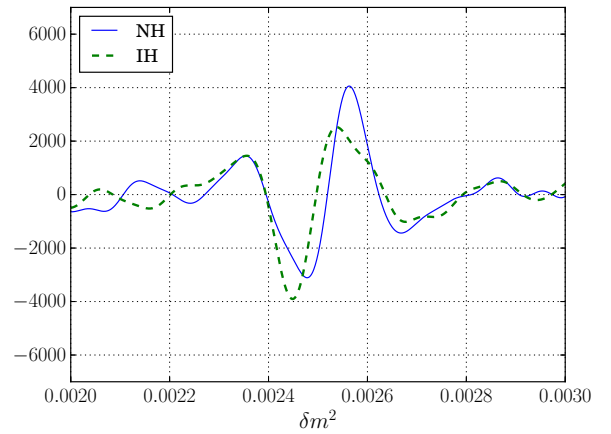
(F) FST for a binning of 200

FIGURE A.2: Shape of the Fourier transform of the spectrum simulated by Monte Carlo simulation for different binnings: 100, 150 and 200. The number of events is 100 000 and we have a infinite resolution.
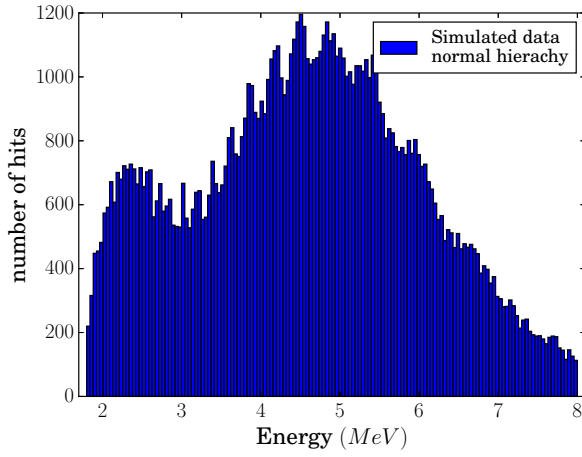
(A) NH and resolution of 0.01

(B) IH and resolution of 0.01

(C) NH and resolution of 0.03
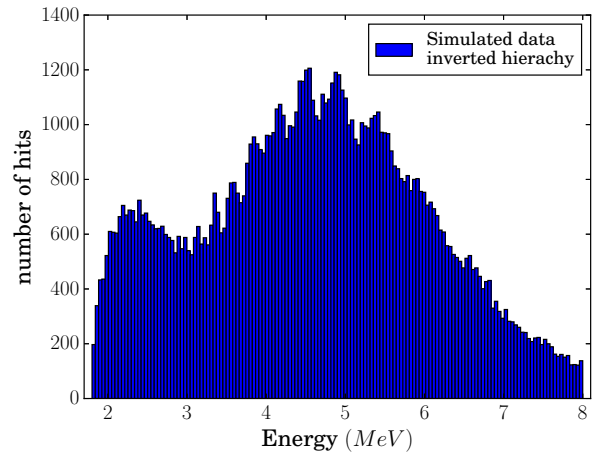
(D) IH and resolution of 0.03
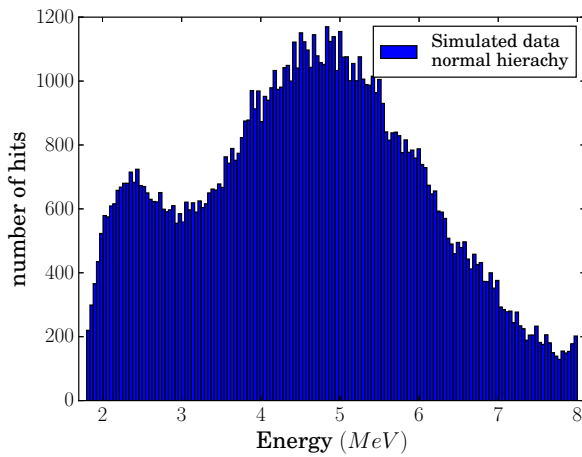
(E) NH and resolution of 0.09
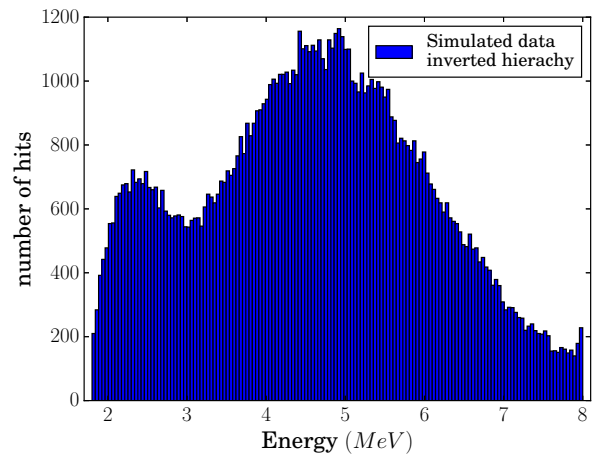
(F) IH and resolution of 0.09

FIGURE A.3: Histogram of the Monte Carlo simulation for different resolutions: 0.01, 0.03 and 0.09. The number of events is 100 000 and the number of bins is 150.
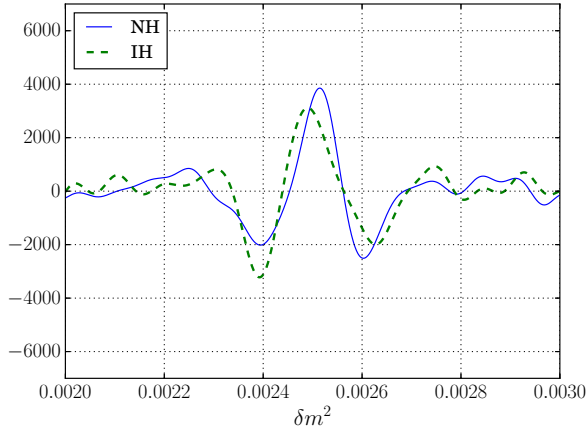
(A) FCT for a resolution of 0.01
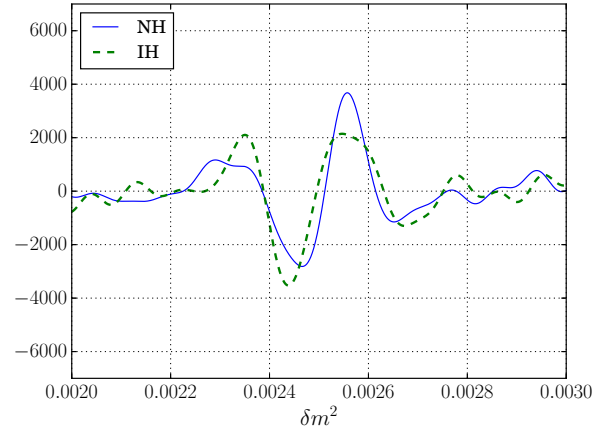
(B) FST for a resolution of 0.01
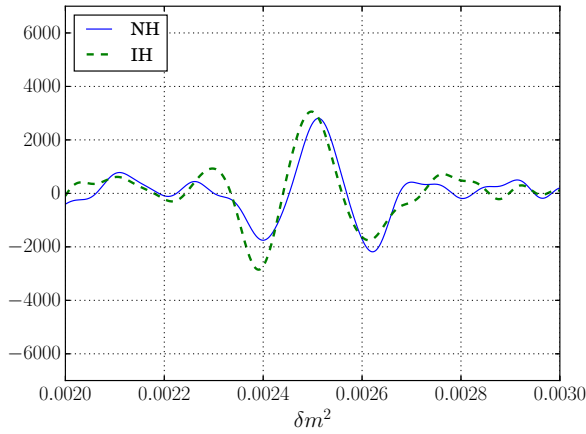
(C) FCT for a resolution of 0.03
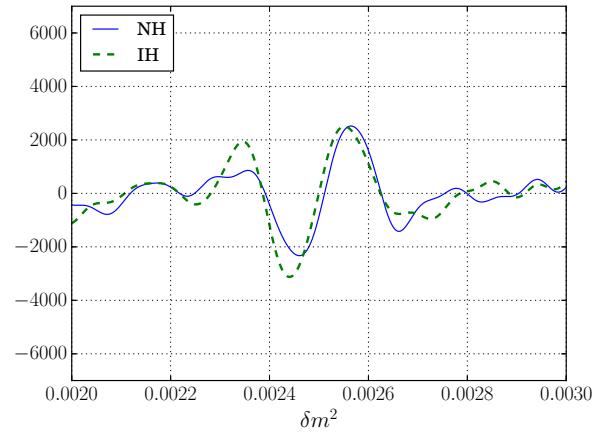
(D) FST for a resolution of 0.03
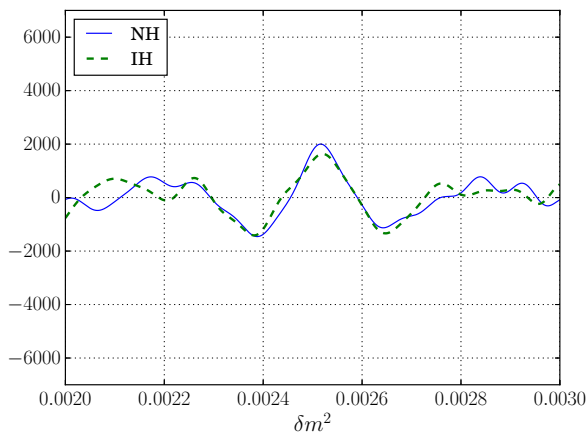
(E) FCT for a resolution of 0.09
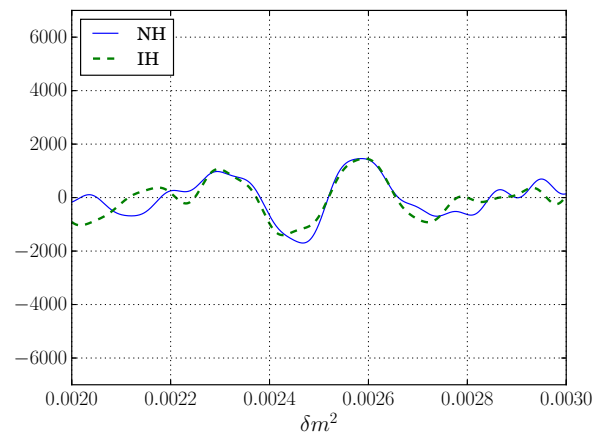
(F) FST for a resolution of 0.09

FIGURE A.4: Shape of the Fourier transform of the spectrum simulated by Monte Carlo simulation for different resolutions: 0.01, 0.03 and 0.09. The number of events is 100 000 and we have a have chosen a binning of 150.
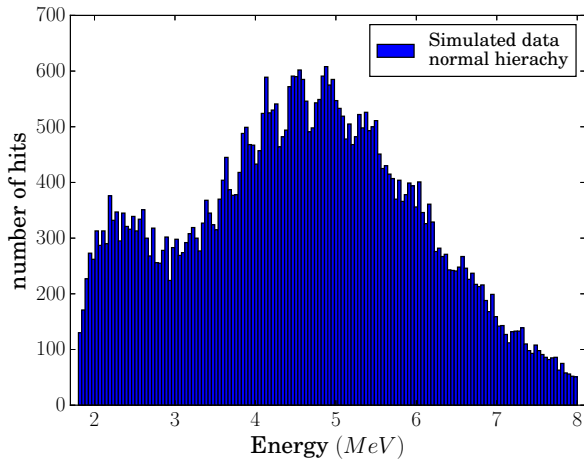
(A) NH and number of events =50 000
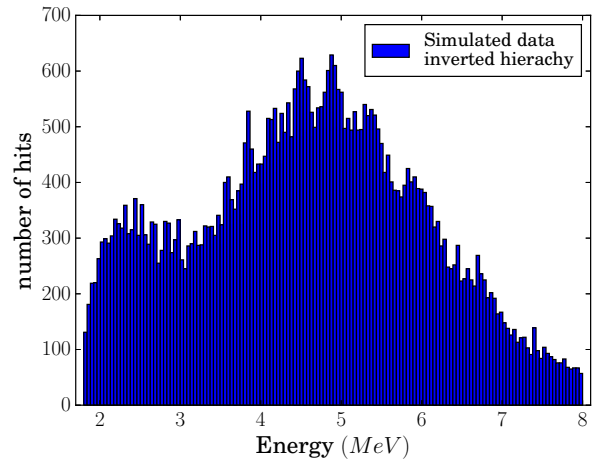
(B) IH and number of events =50 000
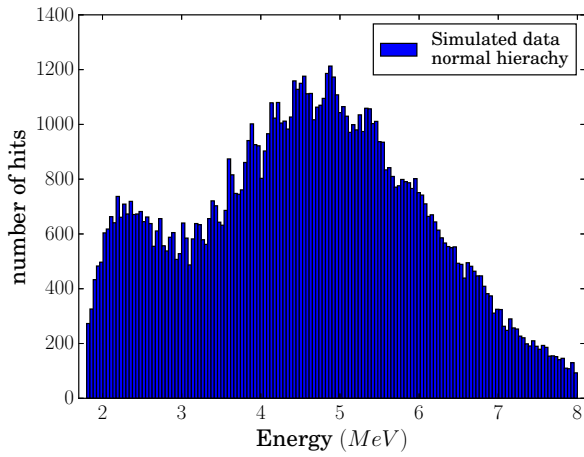
(C) NH and number of events =100 000
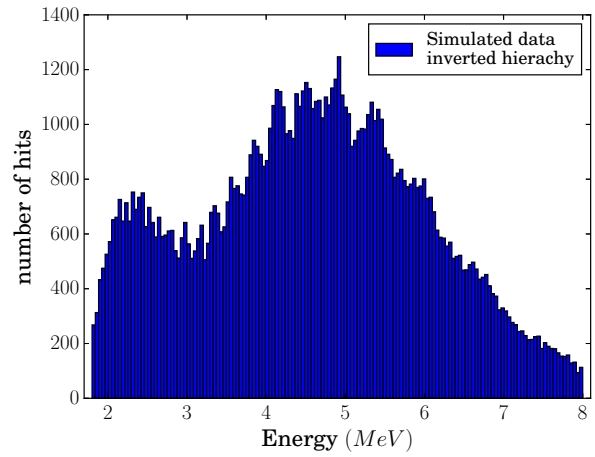
(D) IH and number of events =100 000
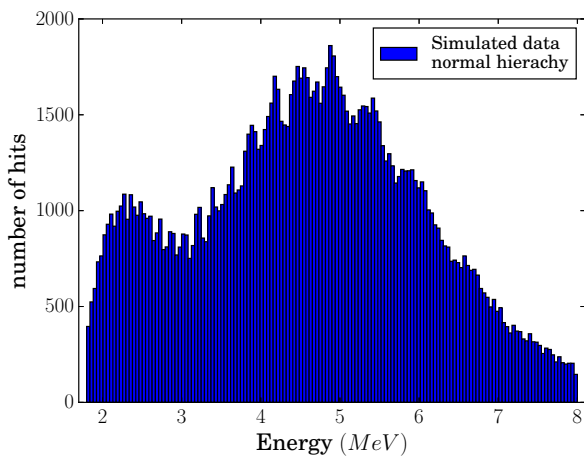
(E) NH and number of events =150 000
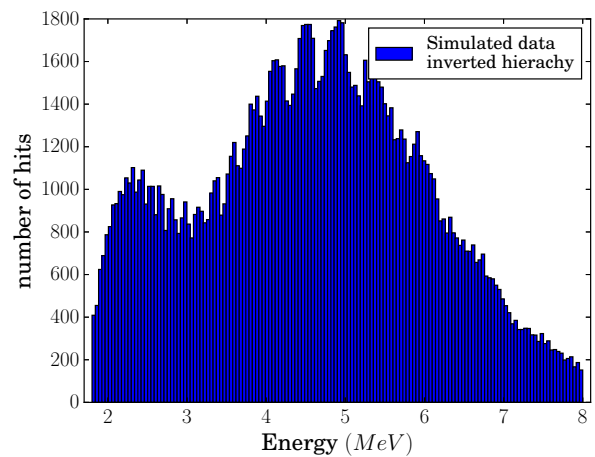
(F) IH and number of events =150 000

FIGURE A.5: Histogram of the Monte Carlo simulation for different number of events: 50 000, 100 000 and 150 000. The resolution is 3% at 1 MeV and we have a have chosen a binning of 150.
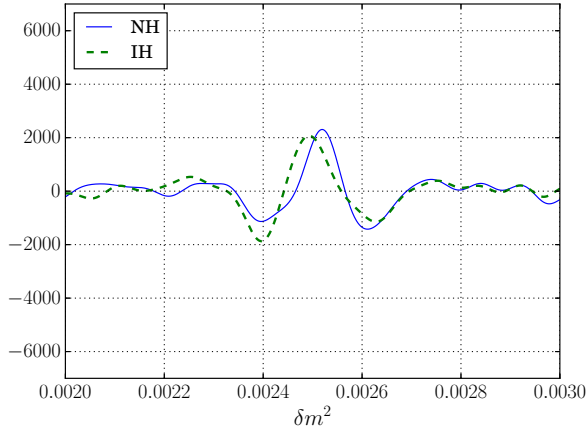
(A) FCT for a number of events =50 000
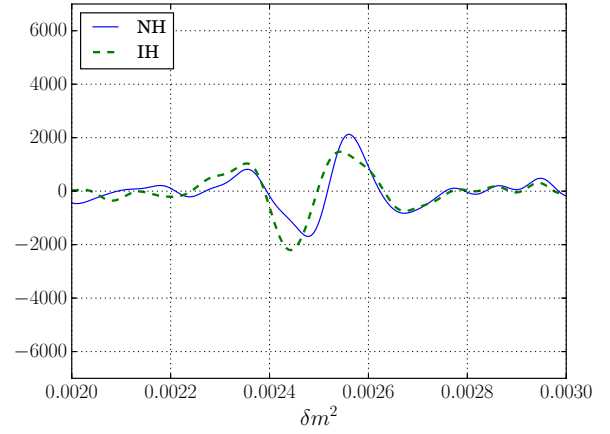
(B) FST for number of events =50 000
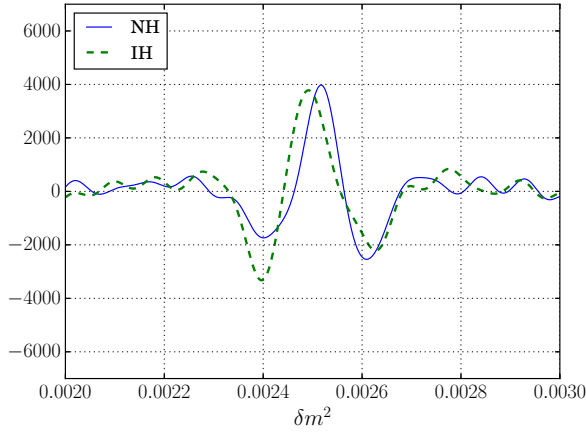
(C) FCT for number of events =100 000
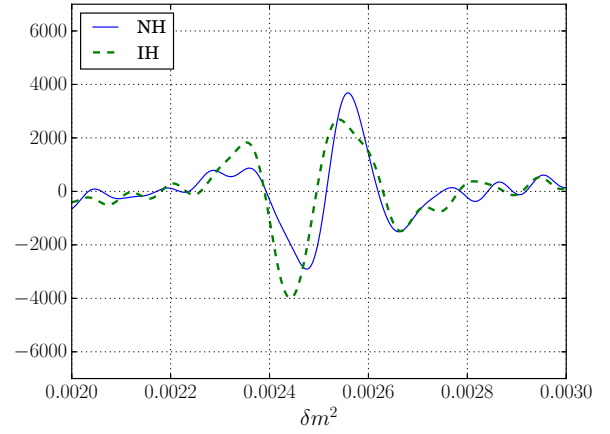
(D) FST for a number of events =100 000
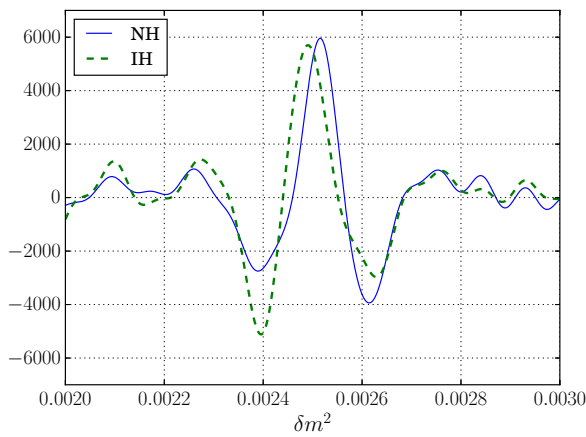
(E) FCT for a number of events =150 000
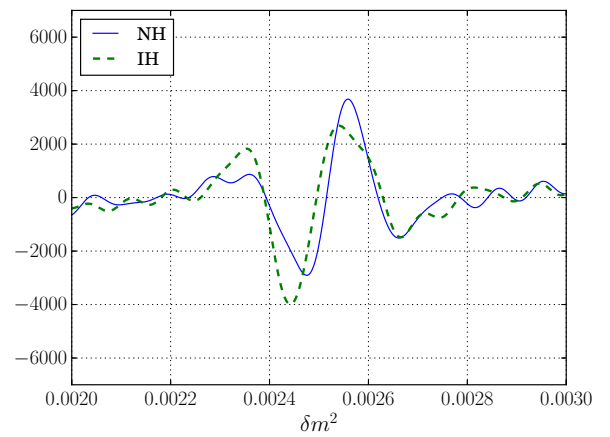
(F) FST for a number of events =150 000

FIGURE A.6: Shape of the Fourier transform of the spectrum simulated by Monte Carlo simulation for different number of events: 50 000, 100 000 and 150 000. The resolution is 3% at 1 MeV and we have a have chosen a binning of 150.

# Appendix B

# Additional PV as function of RL plots

## B.1   PV as function of RL plots for different distances



(A) PVXRL plots for a distance of 35 km

(B) PV as function of RL plots for a distance of 50 km

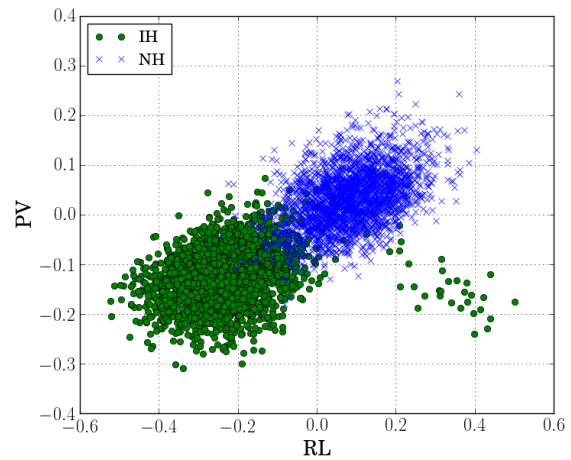(C) PV as function of RL plots for a distance of 75 km 53

(D) PV as function of RL plots for a distance of 75 km
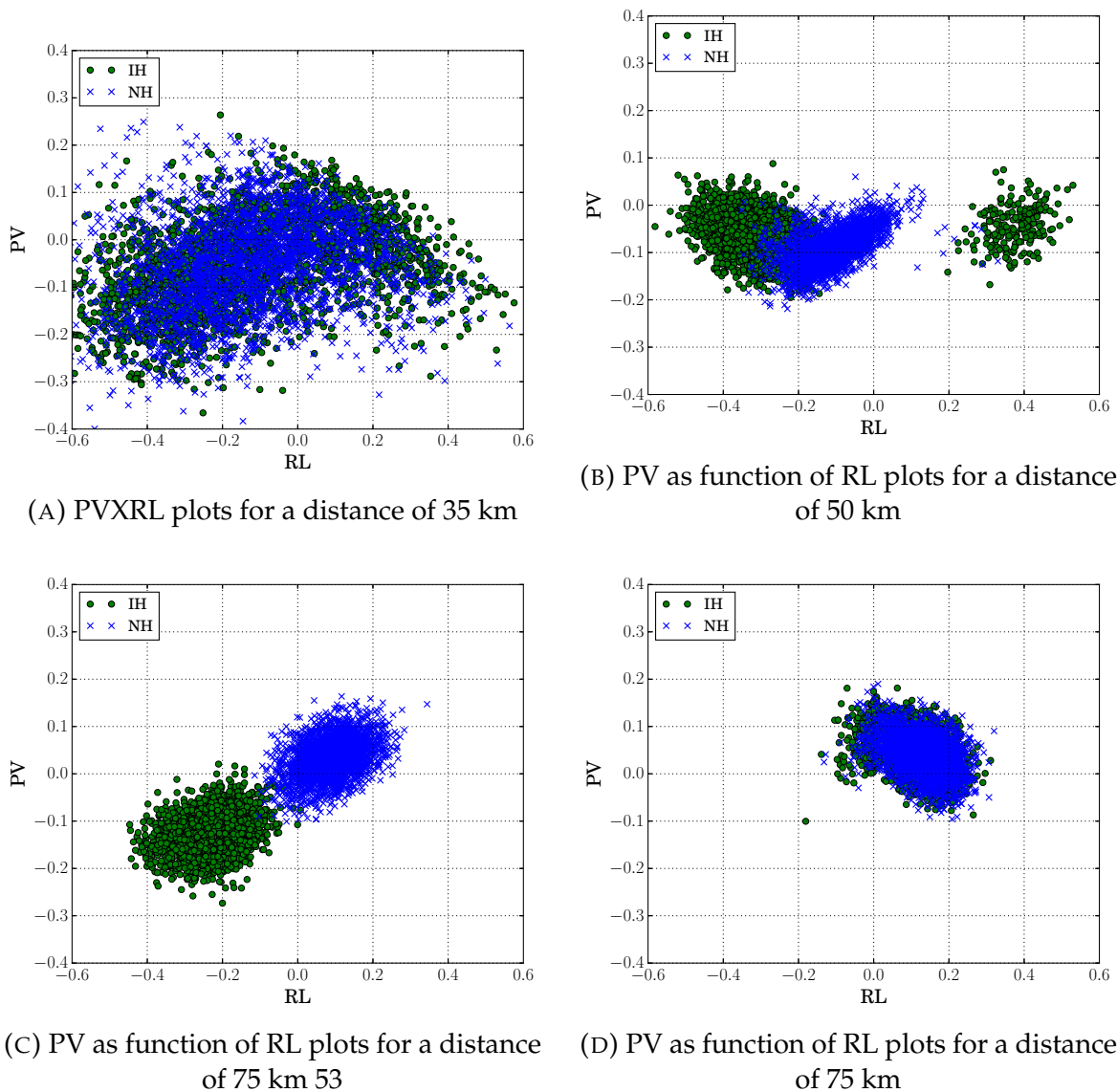
FIGURE B.1: PV as function of RL for the two neutrino mass hierarchies. With a number of simulations of 2000 experiments of 100 000 events each a resolution of 3% at 1 MeV for a distance of 35, 50, 53 and 75 km.

## B.2   PV as function of RL plots for different value of $sin^2(\theta_{13})$
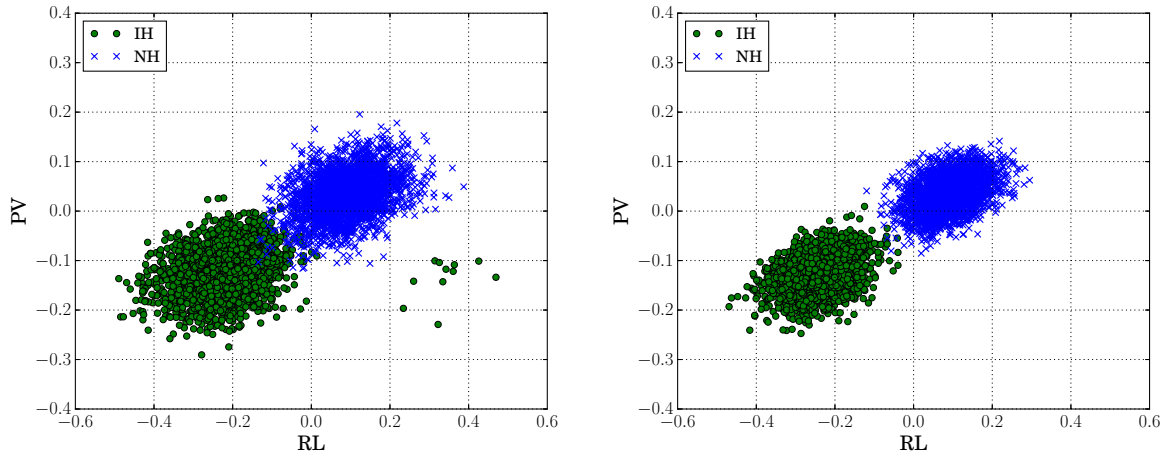


(A) PV as function of RL plots for measured value $-3\sigma$

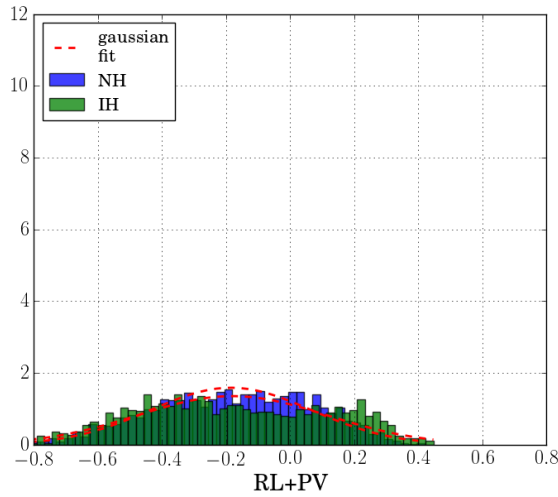(B) PV as function of RL plots for measured value $+3\sigma$
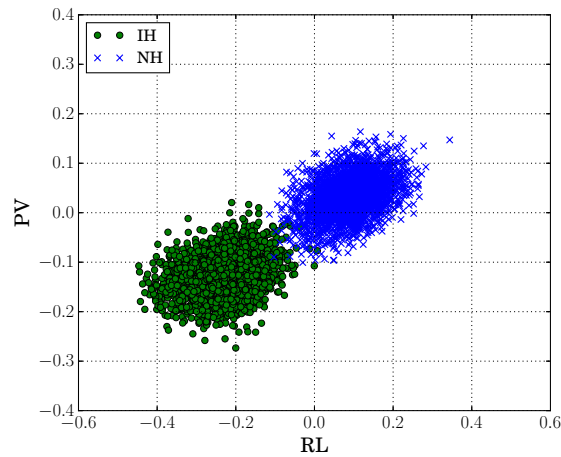
(C) PV as function of RL plots for measured value

FIGURE B.2: PV as function of RL for the two neutrino mass hierarchies. With a number of simulations of 2000 experiments of 100 000 events each a resolution of 3% at 1 MeV for a distance of 53 km for 3 value of $sin^2(\theta_{13})$: measured value $-3\sigma$ (top left), measured value $+3\sigma$ (top right) and measured value (bottom).

## B.3   PV as function of RL plots for different detector resolution
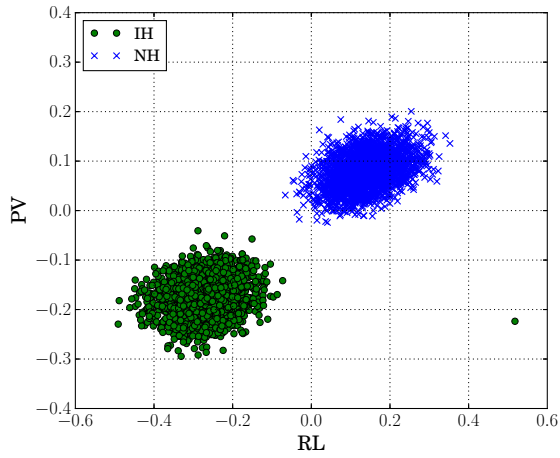


(A) PV as function of RL plots for a resolution of 1%
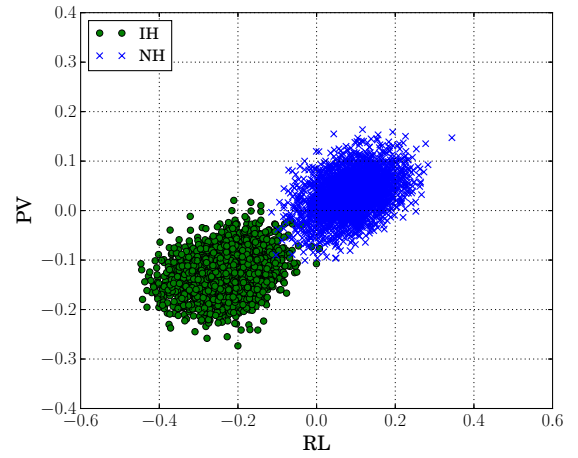
(B) PV as function of RL plots for a resolution of 3%
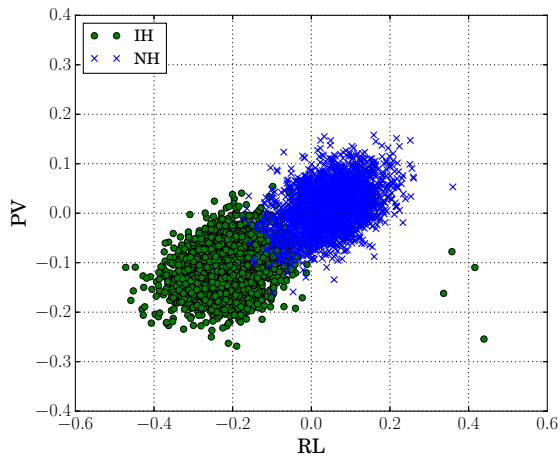
(C) PV as function of RLplots for a resolution of 4%
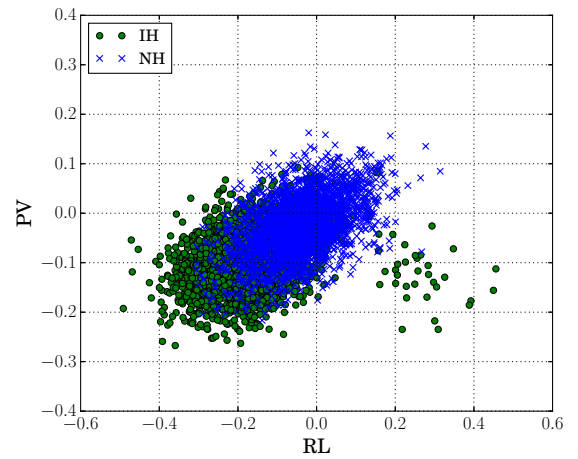
(D) PV as function of RL plots for a resolution of 7%

FIGURE B.3: PV as function of RL for the two neutrino mass hierarchies. With a number of simulations of 2000 experiments of 100 000 events each for a distance of 53 km and the measured value for $sin^2(\theta_{13})$. The resolution of the detector is different for each plot.

## B.4   PV as function of RL plots for different number of events
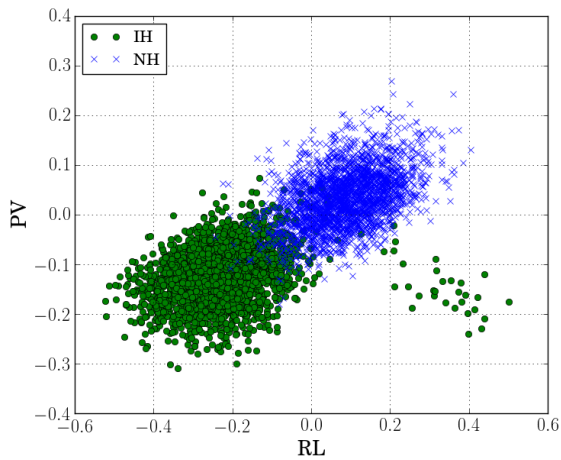


(A) PV as function of RL plots for a number
of events = 50 000



(B) PV as function of RL plots for a number
of events = 80 000
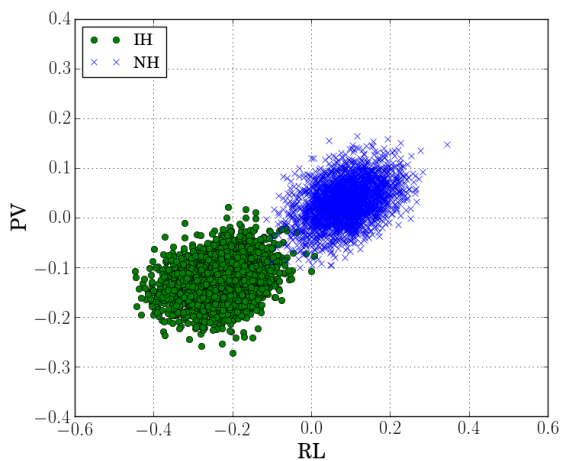


(C) PV as function of RL plots for a number
of events = 100 000
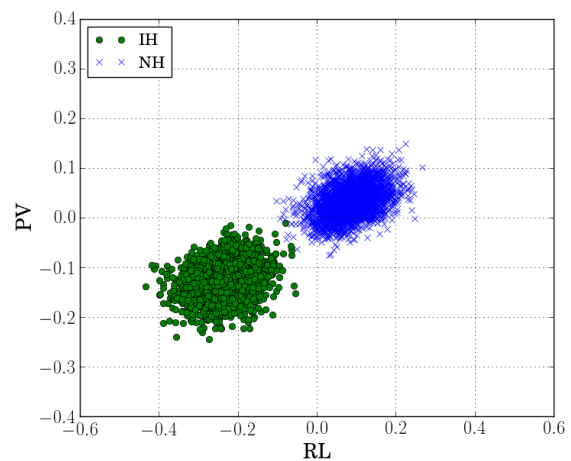


(D) PV as function of RL plots for a number
of events = 150 000

FIGURE B.4: PV as function of RL for the two neutrino mass hierarchies. With a
number of simulations of 2000 experiments of with a variating number of events:
50 000, 80 000, 100 000 and 150 000. The resolution is the standard 3% at 1 MeV for
a distance of 53 km and the measured value for $sin^2(\theta_{13})$.

# Appendix C

# Additional PV+RL plots

## C.1 PV+RL plots for different distances



(A) PV+RL plots for a distance of 35 km
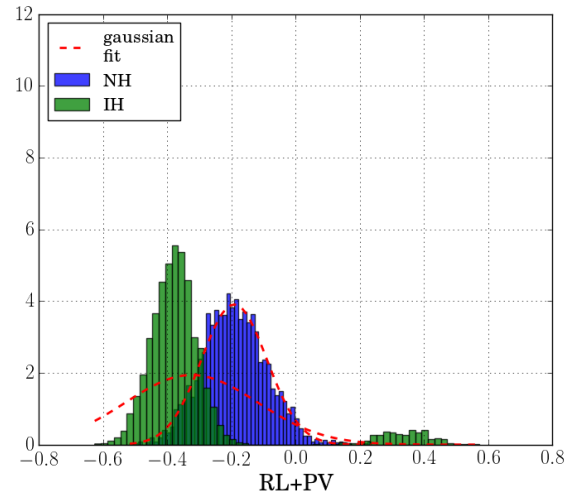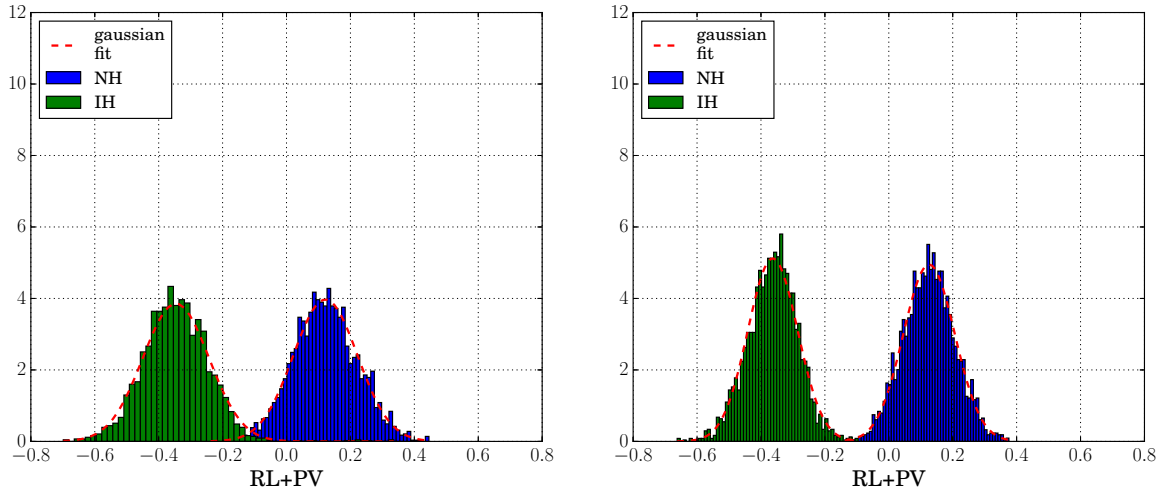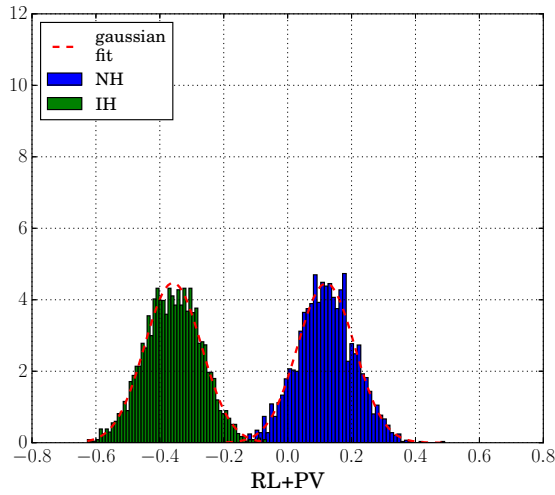
(B) PV+RL plots for a distance of 50 km
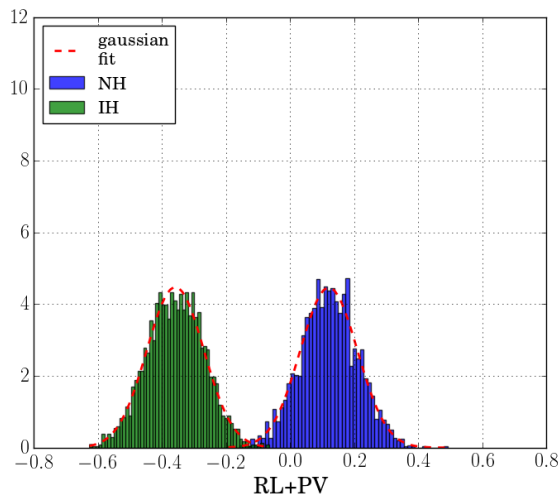
(C) PV+RL plots for a distance of 75 km 53
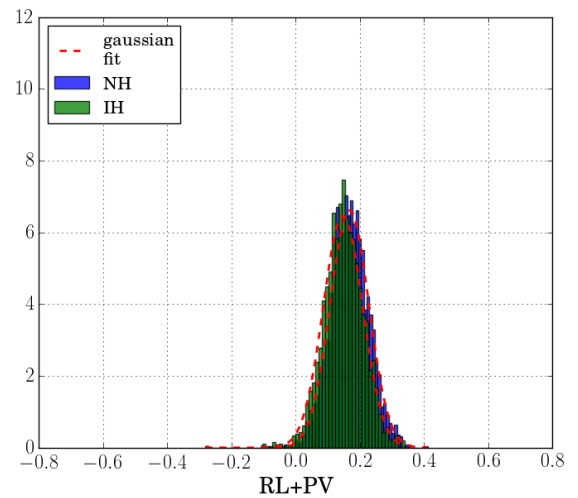
(D) PV+RL plots for a distance of 75 km

FIGURE C.1: PV+RL histograms for the two neutrino mass hierarchies. With a number of simulations of 2000 experiments of 100 000 events each a resolution of 3% at 1 MeV for a distance of 35, 50, 53 and 75 km.

## C.2 PV+RL plots for different value of $sin^2(\theta_{13})$



(A) PV+RL plots for measured value $-3\sigma$



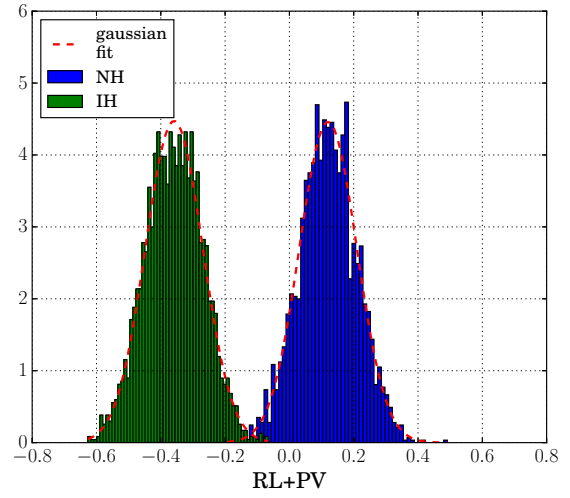(B) PV+RL plots for measured value $+3\sigma$



(C) PV+RL plots for measured value

FIGURE C.2: PV+RL histograms for the two neutrino mass hierarchies. With a number of simulations of 2000 experiments of 100 000 events each a resolution of 3% at 1 MeV for a distance of 53 km for 3 value of $sin^2(\theta_{13})$: measured value $-3\sigma$ (top left), measured value $+3\sigma$ (top right) and measured value (bottom).
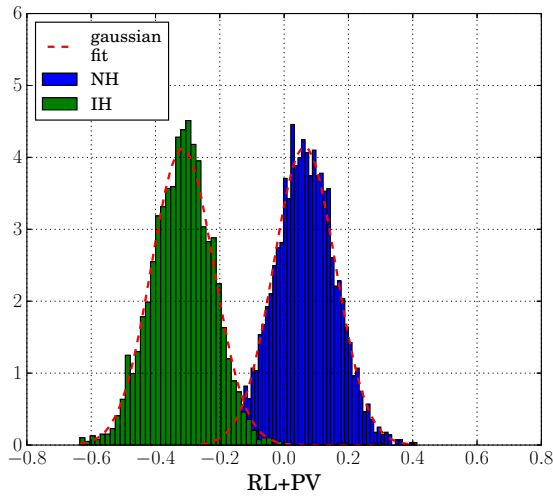
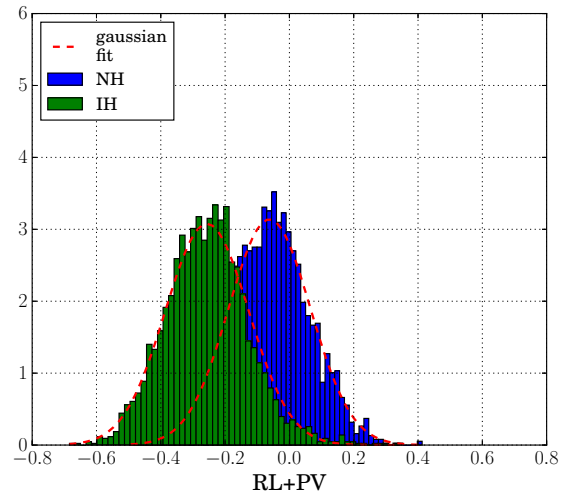## C.3 PV+RL plots for different detector resolution
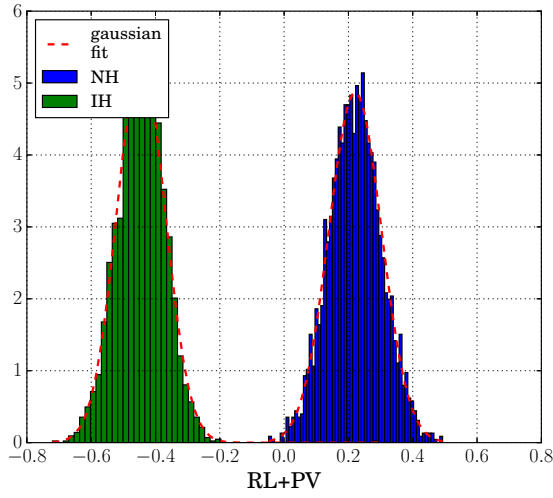


(A) PV+RL plots for a resolution of 1%
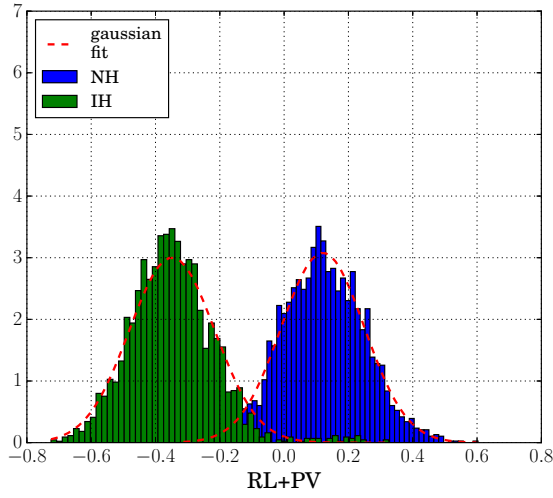
(B) PV+RL plots for a resolution of 3%

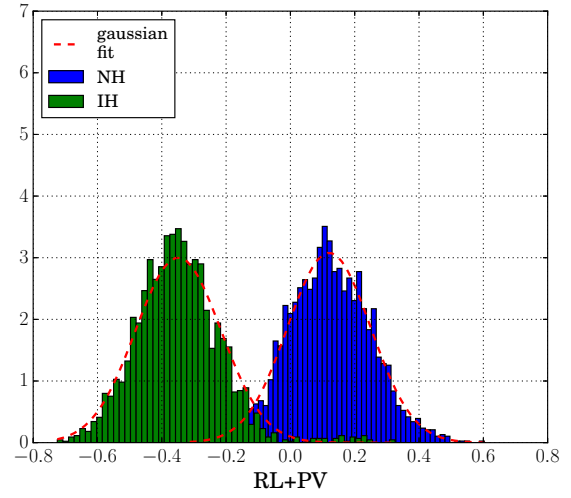(C) PV+RL plots for a resolution of 4%

(D) PV+RL plots for a resolution of 7%

FIGURE C.3: PV+RL histograms for the two neutrino mass hierarchies. With a number of simulations of 2000 experiments of 100 000 events each for a distance of 53 km and the measured value for $sin^2(\theta_{13})$. The resolution of the detector is different for each plot.
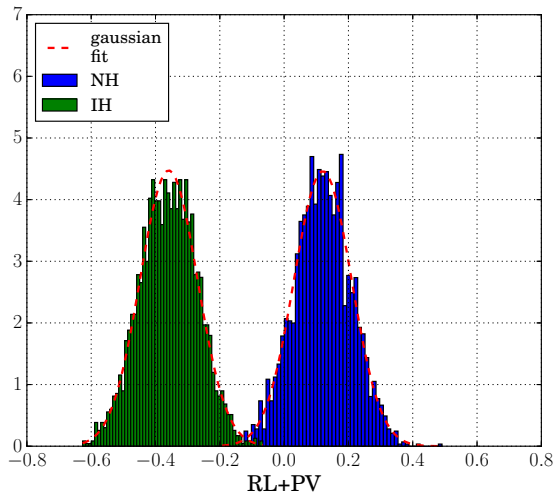
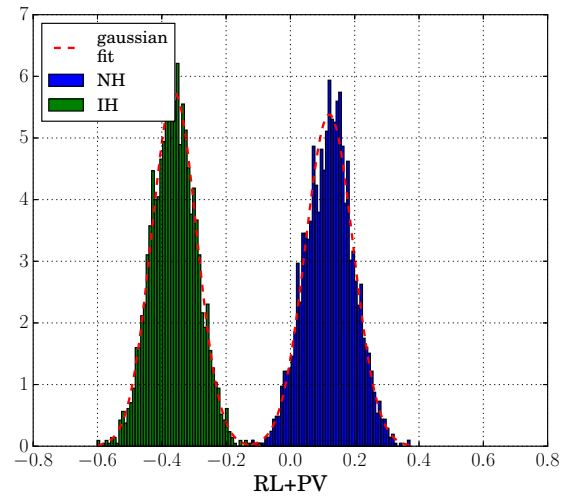## C.4 PV+RL plots for different number of events



(A) PV+RL plots for a number of events = 50 000

(B) PV+RL plots for a number of events = 80 000

(C) PV+RL plots for a number of events = 100 000

(D) PV+RL plots for a number of events = 150 000

FIGURE C.4: PV+RL histograms for the two neutrino mass hierarchies. With a number of simulations of 2000 experiments of with a variating number of events 50 000, 80 000, 100 000 and 150 000 events each. The resolution is the standard 3% at 1 MeV for a distance of 53 km and the measured value for $sin^2(\theta_{13})$.

# Bibliography

[1] Frederick Reines and Clyde L. Cowan. "The Neutrino". In: *Nature* 178.4531 (1956).

[2] Nobel Fundation. URL: https://www.nobelprize.org/nobel_prizes/physics/laureates/2015/ (visited on 09/04/2018).

[3] K.A. Olive. "Review of Particle Physics". In: *Chinese Physics C* 40.10 (2016), p. 100001. DOI: 10.1088/1674-1137/40/10/100001. URL: https://doi.org/10.1088/1674-1137/40/10/100001.

[4] *Standard model*. 2016. URL: https://cosmology.education/images/standard_model.png (visited on 09/04/2018).

[5] Barbara Clerbaux. "Physique des particules". Phys-F416, ULB. Sept. 2017.

[6] F. Capozzi and al. "Status of three-neutrino oscillation parameters, circa 2013". In: *Physical Review D* 89.9 (2014). DOI: 10.1103/physrevd.89.093018. URL: https://doi.org/10.1103/physrevd.89.093018.

[7] Abhijit Bandyopadhyay et al. "On the measurement of solar neutrino oscillation parameters with KamLAND". In: *Physics Letters B* 581.1-2 (2004), pp. 62–74. DOI: 10.1016/j.physletb.2003.11.063. URL: https://doi.org/10.1016/j.physletb.2003.11.063.

[8] S. Fukuda and al. "Determination of solar neutrino oscillation parameters using 1496 days of Super-Kamiokande-I data". In: *Physics Letters B* 539.3-4 (2002), pp. 179–187. DOI: 10.1016/s0370-2693(02)02090-7. URL: https://doi.org/10.1016/s0370-2693(02)02090-7.

[9] K. Abe and al. "Measurement of Neutrino Oscillation Parameters from Muon Neutrino Disappearance with an Off-Axis Beam". In: *Physical Review Letters* 111.21 (2013). DOI: 10.1103/physrevlett.111.211803. URL: https://doi.org/10.1103/physrevlett.111.211803.

[10] Jun Cao and Kam-Biu Luk. "An overview of the Daya Bay reactor neutrino experiment". In: *Nuclear Physics B* 908 (2016), pp. 62–73. DOI: 10.1016/j.nuclphysb.2016.04.034. URL: https://doi.org/10.1016/j.nuclphysb.2016.04.034.

[11] J. K. Ahn et al. "RENO: An Experiment for Neutrino Oscillation Parameter $\theta_{13}$ Using Reactor Neutrinos at Yonggwang". In: (2010). arXiv: 1003.1391 [hep-ex].

[12] Fumihiko Suekane and Thiago Junqueira de Castro Bezerra. "Double Chooz and a history of reactor $\theta_{13}$ experiments". In: *Nuclear Physics B* 908 (2016), pp. 74–93. DOI: 10.1016/j.nuclphysb.2016.04.008. URL: https://doi.org/10.1016/j.nuclphysb.2016.04.008.

[13] Leïla Haegel. *The latest T2K neutrino oscillation results*. 2017. DOI: 10.22323/1.314.0112. arXiv: 1709.04180 [hep-ex].

[14] Francesco Capozzi et al. "Global constraints on absolute neutrino masses and their ordering". In: *Physical Review D* 95.9 (2017). DOI: 10.1103/physrevd.95.096014. URL: https://doi.org/10.1103/physrevd.95.096014.

[15] Gabriel Martínez-Pinedo. URL: https://theorie.ikp.physik.tu-darmstadt.de/nucastro/research_nu_oscillations.html (visited on 09/04/2018).

[16] Sandhya Choubey et al. "Neutrino physics with non-standard interactions at INO". In: *Journal of High Energy Physics* 2015.12 (2015), pp. 1–22. DOI: 10.1007/jhep12(2015)126. URL: https://doi.org/10.1007/jhep12(2015)126.

[17] R.B. Patterson. "The NOvA experiment: status and outlook". In: *Nuclear Physics B - Proceedings Supplements* 235-236 (2013), pp. 151–157. DOI: 10.1016/j.nuclphysbps.2013.04.005. URL: https://doi.org/10.1016/j.nuclphysbps.2013.04.005.

[18] Fengpeng An and al. "Neutrino physics with JUNO". In: *Journal of Physics G: Nuclear and Particle Physics* 43.3 (2016), p. 030401. DOI: 10.1088/0954-3899/43/3/030401. URL: https://doi.org/10.1088/0954-3899/43/3/030401.

[19] Zelimir Djurcic et al. "JUNO Conceptual Design Report". In: (2015). arXiv: 1508.07166 [physics.ins-det].

[20] S.T. Petcov and M. Piai. "The LMA MSW solution of the solar neutrino problem, inverted neutrino mass hierarchy and reactor neutrino experiments". In: *Physics Letters B* 533.1-2 (2002), pp. 94–106. DOI: 10.1016/s0370-2693(02)01591-5. URL: https://doi.org/10.1016/s0370-2693(02)01591-5.

[21] Shao-Feng Ge et al. "Determination of mass hierarchy with medium baseline reactor neutrino experiments". In: *Journal of High Energy Physics* 2013.5 (2013). DOI: 10.1007/jhep05(2013)131. URL: https://doi.org/10.1007/jhep05(2013)131.

[22] Yu-Feng Li et al. "Unambiguous determination of the neutrino mass hierarchy using reactor neutrinos". In: *Physical Review D* 88.1 (2013). DOI: 10.1103/physrevd.88.013008. URL: https://doi.org/10.1103/physrevd.88.013008.

[23] A. B. Balantekin et al. "Neutrino mass hierarchy determination and other physics potential of medium-baseline reactor neutrino oscillation experiments". In: *Proceedings, 2013 Community Summer Study on the Future of U.S. Particle Physics: Snowmass on the Mississippi (CSS2013): Minneapolis, MN, USA, July 29-August 6, 2013*. 2013. arXiv: 1307.7419 [hep-ex]. URL: https://inspirehep.net/record/1245021/files/arXiv:1307.7419.pdf.

[24] R. N. Cahn and al. "White Paper: Measuring the Neutrino Mass Hierarchy". In: *Proceedings, 2013 Community Summer Study on the Future of U.S. Particle Physics: Snowmass on the Mississippi (CSS2013): Minneapolis, MN, USA, July 29-August 6, 2013*. 2013. arXiv: 1307.5487 [hep-ex]. URL: https://inspirehep.net/record/1243859/files/arXiv:1307.5487.pdf.

[25] Yu-Feng Li. "Jiangmen Underground Neutrino Observatory: Status and Prospectives". In: *Proceedings, 17th Lomonosov Conference on Elementary Particle Physics: Moscow, Russia, August 20-26, 2015*. 2017, pp. 27–33. DOI: 10.1142/9789813224568_0004. arXiv: 1606.04743 [physics.ins-det]. URL: https://inspirehep.net/record/1469449/files/arXiv:1606.04743.pdf.

[26] Marco Grassi. "Double Calorimetry in Liquid Scintillator Detectors". The 26th International Workshop on Weak Interactions and Neutrinos (WIN2017). 2017. URL: https://indico.fnal.gov/event/9942/session/4/contribution/50/material/slides/0.pdf.

[27]  Yury Malyshkin. "JUNO: Next Generation Reactor Neutrino Experiment". HEP2016. 2016. URL: https://indico.cern.ch/event/385771/contributions/919133/attachments/1211236/1766672/JUNO_Malyshkin_HEP2016.pdf.

[28]  Guillaume Mention. "Etude des sensibilité et bruits de fond de l'expérience Double Chooz pour la recherche du paramètre de mélange leptonique Theta 13". Theses. Université Claude Bernard - Lyon I, 2005. URL: https://tel.archives-ouvertes.fr/tel-00010528.

[29]  Hitoshi Murayama and Aaron Pierce. "Energy spectra of reactor neutrinos at KamLAND". In: *Physical Review D* 65.1 (2001). DOI: 10.1103/physrevd.65.013012. URL: https://doi.org/10.1103/physrevd.65.013012.

[30]  J. Engel et al. "Double beta decay in the generalized-seniority scheme". eng. In: *Physics Letters B* 225.1 (1989), pp. 5–9. ISSN: 0370-2693.

[31]  P. Vogel and J. F. Beacom. "Angular distribution of neutron inverse beta decay, $\bar{\nu}_e p \rightarrow e^{+} n$". In: *Physical Review D* 60.5 (1999). DOI: 10.1103/physrevd.60.053003. URL: https://doi.org/10.1103/physrevd.60.053003.

[32]  S.M. Bilenky, D. Nicolo, and S.T. Petcov. "Constraints on $|U_{e3}|^2$ from a three-neutrino oscillation analysis of the CHOOZ data". eng. In: *Physics Letters B* 538.1 (2002), pp. 77–86. ISSN: 0370-2693.

[33]  Liang Zhan et al. "Determination of the neutrino mass hierarchy at an intermediate baseline". In: *Physical Review D* 78.11 (2008). DOI: 10.1103/physrevd.78.111103. URL: https://doi.org/10.1103/physrevd.78.111103.

[34]  Malvin H Kalos. *Monte Carlo methods*. eng. 2nd rev. and enl. ed.. Weinheim: Wiley-Blackwell, 2008. ISBN: 9783527407606.

[35]  Pierre L'Ecuyer. "Good Parameters and Implementations for Combined Multiple Recursive Random Number Generators". In: *Operations Research* 47.1 (1999), pp. 159–164. DOI: 10.1287/opre.47.1.159. URL: https://doi.org/10.1287/opre.47.1.159.

[36]  Liang Zhan et al. "Experimental requirements to determine the neutrino mass hierarchy using reactor neutrinos". In: *Physical Review D* 79.7 (2009). DOI: 10.1103/physrevd.79.073007. URL: https://doi.org/10.1103/physrevd.79.073007.